Important Notice

UNIVERSITY OF CALGARY

Multicomponent seismic exploration and ground-penetrating radar surveying in the Canadian Arctic

by

Carlos E. Nieto

A THESIS

SUBMITTED TO THE FACULTY OF GRADUATE STUDIES

IN PARTIAL FULFILMENT OF THE REQUIREMENTS FOR THE

DEGREE OF MASTER OF SCIENCE IN GEOLOGY AND GEOPHYSICS

DEPARTMENT OF GEOLOGY AND GEOPHYSICS

CALGARY, ALBERTA

FEBRUARY, 2005

UNIVERSITY OF CALGARY

FACULTY OF GRADUATE STUDIES

The undersigned certify that they have read, and recommend to the Faculty of Graduate Studies for acceptance, a thesis entitled “Multicomponent seismic exploration and ground-penetrating radar surveying in the Canadian Arctic” submitted by Carlos E. Nieto in partial fulfillment of the requirements for the degree of Master of Science in Geology and Geophysics.

_____

Supervisor, Dr. Robert R. Stewart
Department of Geology and Geophysics

_____

Dr. Brian Moorman
Department of Geology and Geophysics

_____

Dr. Alejandro Ramirez-Serrano
Department of Mechanical and Manufacturing Engineering

_____

Date

Abstract

This thesis explores the near-surface and deeper subsurface in two different locations of the Canadian Arctic: Devon Island, and Hadween Island in the Mackenzie Delta. A perennial frozen layer, known as permafrost covers part of the study area. The top of this layer thaws during the summer months forming the seasonally unfrozen layer. A similar phenomenon is also observed in the planet Mars. Imaging the subsurface using multicomponent seismic exploration and ground-penetrating radar surveys is the main objective of this work.

The Devon Island case study shows that both methods produce a good quality image of the near-surface. However, the ground-penetrating radar method yields a better image in a faster acquisition and data processing time. A new seismic processing flow based on a linear-offset correction of head wave energy is presented as a solution to produce images under these conditions. A V_P/V_S ratio of 1.55 was obtained for the seasonally unfrozen layer. Velocities of 260 m/s and 168 m/s for P and S-waves were obtained as well. The permafrost shows a similar V_P/V_S ratio of 1.53, with P and S-wave velocities of 3100 and 2030 m/s respectively. For the 2.5D ground-penetrating radar surveys linear interpolation was required to produce an image from the subsurface. A radar velocity change was interpreted as the contrast between lithology of thawed layer and permafrost.

In the Mackenzie Delta study area, the first known multicomponent survey in the Canadian Arctic was recorded and processed. PP and PS seismic sections were obtained and interpreted using well log data from the Hansen G-07. A compelling correlation between the PP and PS seismic sections was found using a V_P/V_S ratio of 1.9.

Acknowledgements

Thanks to every member and sponsor of the Consortium for Research in Elastic Wave Exploration Seismology (CREWES) which is and hope continue being a great place to learn. Special thanks to my supervisor, Dr. Robert R. Stewart not only for his guidance, knowledge and experience but also for his support and encouragement during my time at the University of Calgary. I express my appreciation to the NASA Haughton-Mars Project, and specially its principal investigator Dr. Pascal Lee of NASA Ames. Thanks to our Inuit helpers: Sam, Jon and Pauline. Thanks to Sensors & Software Inc. for all the ground-penetrating radar support.

From the University of Calgary I would like to express my gratitude to Dr. Federico F. Krause for the support and help in the bad parts of the road; Regina Shedd for all the technical and personal help offered throughout my program; Dr. Lawton for important discussions on various areas of multicomponent seismic; Drs. Henley and Krebes for discussions in theoretical seismology; Kevin Hall, Eric Gallant, Henry Bland and Charles Ursenbach for their technical expertise in different areas; and to Louise Forgues and Cathy Hubbell for their assistance.

Finally, many thanks to all the students, staff and proffesors at the University of Calgary for their support and friendship.

Dedication

...para Aurelio, Elena, Claudia Karina y Juan Pablo.

Y para mis abuelos Aurelio, Cecilia, Elena e Ignacio...

TABLE OF CONTENTS

LIST OF TABLES

LIST OF FIGURES

CHAPTER ONE: *INTRODUCTION*

This thesis explores the near-surface and deeper subsurface in two different locations of the Canadian Arctic: Devon Island, and Hadween Island in the Mackenzie Delta. The Northwest Territories and Nunavut cover a vast area in the northern latitudes of Canada. Based mainly on seismic exploration and more than 400 wells, several basins have been studied in the Mackenzie Delta with major oil + gas discoveries (Polczer, 2001). Production from these fields waits for delivery options such as the Mackenzie Valley Pipeline. Interest in developing these regions has increased in the last 5 years, creating a need for technologies capable of coping with the harsh climate conditions of the Arctic, and the challenges of subsurface imaging common to this setting.

1.1- *Motivation*

The Canadian Arctic lies upon a perennial frozen layer, often defined as permafrost. The thickness of this layer varies generally with latitude, thinning southward, where warmer temperatures are typical on the surface. Thickness may also be associated with the presence of water in the form of lakes, rivers, or underground streams. The fact that part of the subsurface is frozen represents a challenge for the development of this area, including oil and gas exploration and production activities. During the summer months, as surface temperature increases, part of the permafrost thaws forming the seasonally unfrozen layer.

The surface of the planet Mars is also been thought to be underlain by frozen ground (Lee, 2002; Long, 1999), and this has been a topic of research for different institutions around the world - the NASA Haughton-Mars Project (HMP) being one of them. HMP is located on Devon Island, Nunavut, where geologic and climatic conditions provide some

similarities to those on Mars. One of the objectives of HMP is to use geophysical exploration techniques, particularly seismic and ground-penetrating radar to study aqueous and frozen ground systems (www.marsonearth.org). Understanding the processes behind the formation of frozen and thawed layers is important to both the development of the Canadian Arctic and to future Mars analysis.

1.2- *Objectives*

Imaging the subsurface is the main research of this study. To investigate the capabilities and limitations of high resolution seismic and ground-penetrating radar exploration techniques for near surface imaging in periglacial environments. These objectives are achieved through the analysis of data acquired in the two study areas: Devon Island and Hadween Island.

1.3- *Devon Island study area*

Located in the central part of the Canadian Arctic Islands in Nunavut, Devon Island with a surface area of 66,800 km^2 is the largest unhabited island on Earth (Figure 1.1). It has been visited by a number of research groups interested in the study of ice caps, glaciers, wildlife, archaeology, and simulations of living logistics on Mars, among others. It was the site of much hydrocarbon exploration activity in the 1960s and 70s and has a number of dry and abandoned offshore wells in its vicinity (Wilkin, 1998).

The majority of the exploration for oil and gas of the island was centred on the Grinnell Peninsula (Figure 1.1). In 1962, west of Devon on Melville Island, the first well Dome Winter Harbour No. 1 in the Canadian Arctic Islands was completed (Figure 1.2). The

well was dry, but it increased the interest in the Arctic Islands. Melville Island was the centre of operations for the exploration wells drilled through out the 70s.

Figure 1.1 Map of Devon Island, Nunavut (Glacier Atlas of Canada). Grinnell and North Yorkshire peninsulas are to the northwest part of Devon Island.

A number of private geological field teams explored the Grinnell Peninsula, finding only poor hydrocarbon potential on northern Devon Island (Mayr *et al.*, 1998). Mayr (1998) states that hydrocarbon accumulations from the middle member of the Allen Bay Formation may be trapped in the Devon Island Formation reefs, in the area north of Grinnell and North Yorkshire peninsulas (Figure 1.1).

The Lancaster Sound basin, located southeast of Devon Island, was an important area for exploration in the 70s. More than 6500 km of offshore marine seismic were recorded in this zone (Figure 1.1). The objective was the zone proximal to the basement uplift, the Dundas structure (www.canstrat.com).

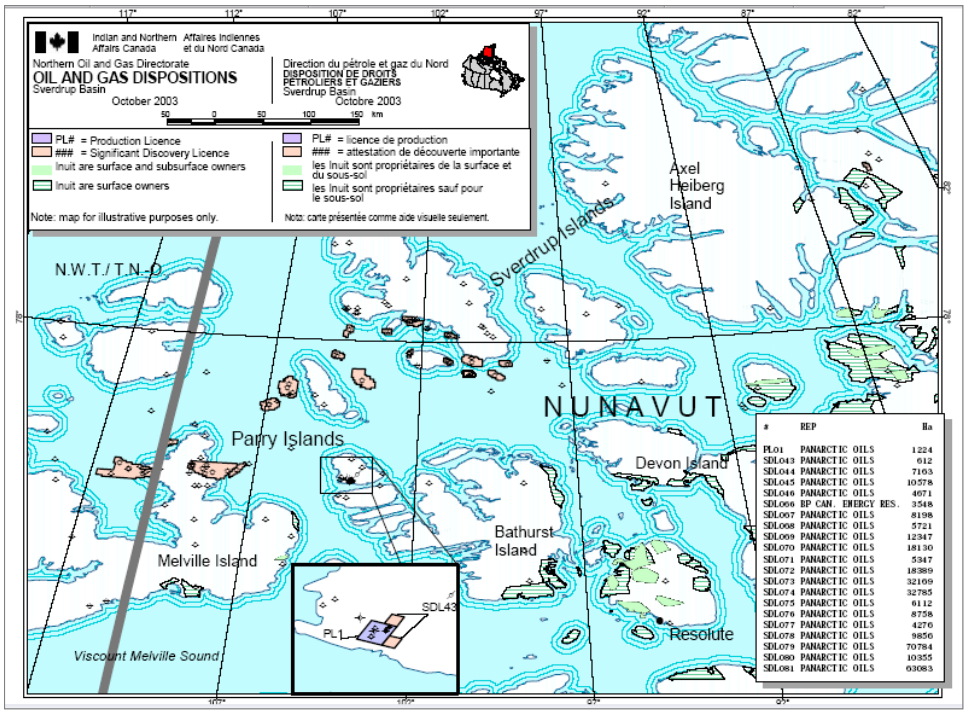

Figure 1.2 Map of region around Devon Island, Nunavut Territory (Indian and Northern Affairs Canada). Grinnell and North Yorkshire peninsulas are in the northwest part of Devon Island.

NASA Haughton – Mars Project (HMP)

The HMP is a field research project whose main objective is the scientific study of the Haughton impact structure and its surroundings, viewed as a terrestrial analog for Mars. In 1996, Dr. Pascal Lee initiated the project with a postdoctoral research proposal approved by the National Research Council (NRC) of the US National Academy of Sciences and NASA Ames Research Center (ARC). It has been active since the summer

of 1997, when the first research group surveyed the Haughton area confirming the potential for Mars analog studies (www.marsonearth.org). A total of eight field seasons have been successfully completed with the participation of various universities and institutions from around the world. The base camp of the HMP is located just outside the northwest area of the Haughton impact crater (Figure 1.1).

The project is divided into two branches: the science and the exploration program. The goals of the *science program* can be summarized in three categories:

(1) Obtain insights into the *possible* evolution of water and of past climates on Mars.

(2) Study the effects of impacts on Earth and on other planets.

(3) Analyze the possibilities and limits of life in extreme environments.

On the other hand, the *exploration program* focuses on the development of new technologies/strategies and the use of human factors experience and field-based operation for the design of the future exploration of the Moon, Mars and other planets by robots and humans. The University of Calgary has collaborated with the science program in two different areas:

(1) Subsurface Geologic Structure: ground-penetrating radar and seismic surveys of a variety of substrates at the Haughton impact structure and surrounding terrain are targeted at determining the crater's subsurface structure; and

(2) Ground Ice and Subsurface Aqueous Environments, and Periglacial Geology: ground-penetrating radar surveys of ground ice and subsurface water at the Haughton impact structure and surrounding terrain are conducted and analyzed as an analog for exploring possible subsurface H_2O-rich environments on the Moon and Mars.

1.4- *Mackenzie Delta study area*

The discovery of the Taglu, Parsons Lake and Niglintgak gas fields in the years of 1971, 1972 and 1973, respectively, generated interest in the commercial exploration for hydrocarbon in the Mackenzie Delta area. Approximately six trillion cubic feet of natural gas has been discovered in the area. 2D and 3D reflection seismic surveys were essential to the discovery of these three giant gas fields. Currently, the construction of a pipeline connecting the Delta to northern Alberta has been a topic of active discussion (Figure 1.3).

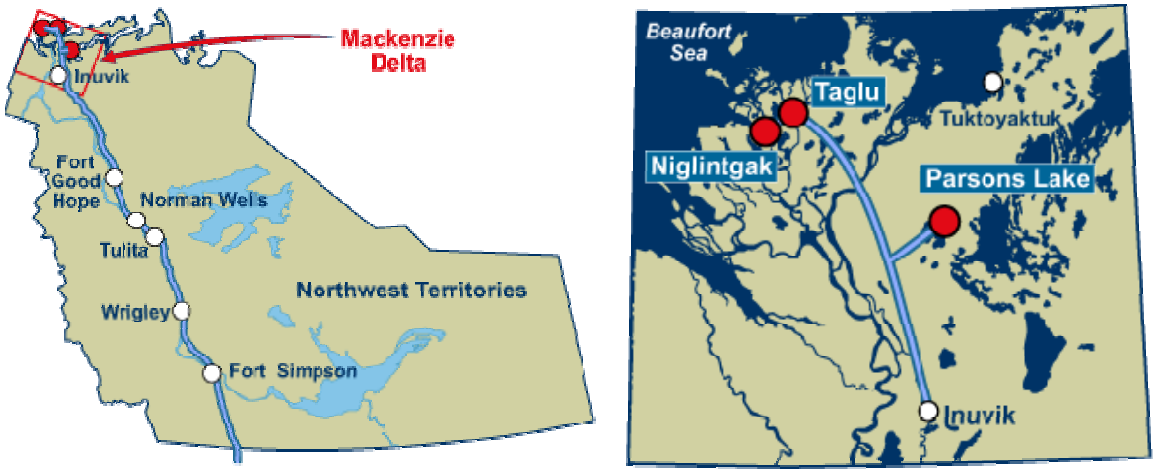

Figure 1.3 Mackenzie Valley Gas Pipeline route (modified from www.mackenziegasproject.com). A total of 1200 km could connect the Mackenzie Delta with Northern Alberta.

As a result of numerous feasibility studies and proposals, the Mackenzie Gas Project (MGP) was formed. The partners in this project comprise four major oil companies: Imperial Oil Resources Ventures Ltd., ConocoPhillips Canada (North) Ltd., ExxonMobil Canada Properties, and Shell Canada Ltd.; plus the Aboriginal Pipeline Group (APG). The MGP has the objective of connecting northern onshore gas fields with North

American markets through a 1220 – kilometer natural gas pipeline system, which is proposed to run through the Mackenzie Valley (www.mackenziegasproject.com). The ultimate goal is to begin transporting natural gas through the pipeline by 2010.

The surface of the Mackenzie Delta area has large water coverage, in the form of lakes and rivers. During the winter a layer of ice covers the entire area. When the summer warms the surface, and the ice starts thawing, the top part of the frozen ground thaws, forming what is known as the active layer. This layer may vary according to different factors such as the mean annual ground temperature, nature of the ground surface cover, and/or the thermal properties of the soil material (Williams *et al.*, 1989). All of these processes make the near surface a complex medium with not only lateral but vertical variation in terms of elastic properties. Recording seismic surveys in this type of environment is challenging due to this varying subsurface.

Some of the seismic issues related with periglacial environments are:

(1) Variation in amplitude energy level;

(2) Trapped and/or surface waves;

(3) Poor transmission of acoustic energy to the subsurface;

(4) Reverberations and/or flexural waves;

(5) Large variation of static times.

The CREWES Project at the University of Calgary was invited to participate in the acquisition of a 2D multicomponent seismic test line in a transition zone from floating ice to ground – fast ice. A compelling PP and PS 2-D seismic interpretation was achieved in the end.

CHAPTER TWO: *SEISMIC EXPLORATION AT DEVON ISLAND, NUNAVUT*

2.1- *Introduction, assumptions and previous work*

Water-saturated sediments show an increase of the compressional-wave velocity when temperature drops from 26º C to -36º C (Timur, 1968). The change of elastic modulae due to the freezing of interstitial water may be applied to use the seismic method for the study of physical properties of soil in periglacial environments. On average, an increase of 34% in the velocity of compressional waves due to freezing is obtained in different sands studied by Timur (1968). Based on this fact, a number of seismic experiments were recorded at two different locations in the Canadian Arctic as part of the NASA Haughton-Mars Project. On average, the thickness of the active layer (water-saturated sediments) is 0.6 m, with variations in the order of centimeters due to changes in the mean annual temperature of the region.

Nieto *et al.* (2003) obtained compressional and shear wave velocities of *260 and 168 m/s*, with a V_P/V_S ratio of *1.55* in the very near surface. The underlying frozen sediments (permafrost) showed a much higher compressional wave velocity of *3100 m/s and 2030 m/s* for shear waves, with a V_P/V_S *ratio of 1.53.* This strong impedance contrast between frozen and thawed layers represents a challenge to the seismic project due to diverse factors such as;

(1) The critical angle of incidence is close to vertical, restricting the energy transmitted to the sub-permafrost layers;

(2) Most of the seismic energy is trapped in the thawed layer, which results in reverberations and multiples that contaminate the records; and

(3) Small part of the energy gets transmitted below this interface, reducing the possibility of imaging sub-permafrost unfrozen bodies (taliks), if present.

To visualize this situation and understand the propagation of elastic waves in this type of subsurface, seismic ray arrival times were calculated and energy partition were generated. An additional objective of this thesis was to study the possibility of imaging an unfrozen layer (*i.e.* talik) inside the permafrost layer. A general subsurface model, which includes a talik (Table 2.1 and Figure 2.1), was designed based on previous measurements and reference values (Telford *et al.*, 1967; Nieto *et al.*, 2003).

Strata	Thickness (m)	V_P (m/s)	V_S (m/s)	ρ (g/cc)
Water-saturated silt	0.6	260	168	2.21
Seasonal frozen	0.3	3100	2030	2.0
Talik (dry silt)	0.4	260	168	1.43
Permafrost	n.a.	3100	2030	2.0

Table 2.1 Elastic parameters for the near surface periglacial model. Density values taken from Telford *et al.* (1967)

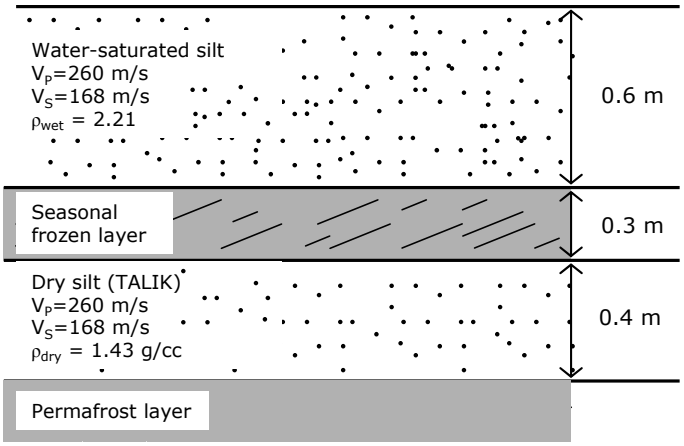

Figure 2.1 Periglacial near-surface elastic model of a particular High Arctic area during the summer including a talik.

Consider a model formed by only the first two layers of the periglacial model (Figure 2.1) and an incident P (compressional) wave to calculate the exact solution of energy partition based on Zoeppritz equations (www.crewes.org). Only the homogeneous solutions are considered for the analysis, i.e. below the critical angle. From the diagram (Figure 2.2) the following are observed:

(1) A critical angle of incidence of 4.81º.

(2) A large and almost constant R_{PP} reflection coefficient versus angle of incidence, approximately 0.8;

(3) An increasing R_{PS} reflection coefficient versus angle of incidence, ranging between 0 to -0.2;

(4) A low coefficient of transmission T_{PP}, near 0.18, and no variation with versus angle of incidence; and

(5) Increasing transmission coefficient T_{PS} with angle of incidence, ranging between 0 to -0.2.

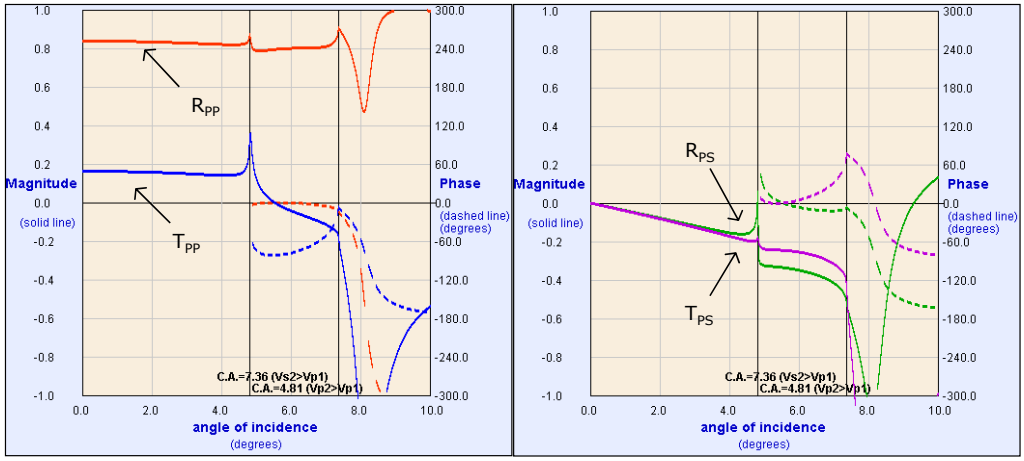

Figure 2.2 Energy partition at the thawed-frozen layer interface of the periglacial model. Observe the small critical angle of incidence caused by the P-wave velocity contrast. R_{PP}, R_{PS}, T_{PP} and T_{PS} are the reflectivity coefficient and transmission coefficient, for PP and PS events, respectively. Dashed and solid lines are the phase and energy partition curves, respectively.

A high reflection coefficient R_{PP} is a promising factor for the application of seismic reflection techniques to survey these areas (periglacial near surface). The critical angle of incidence is small and restricts the transmission of homogeneous waves to the sub-permafrost layers. T_{PP} is considerably smaller than the reflection coefficient R_{PP}. The low transmission coefficient energy plus the attenuation and amplitude decay due to a spreading factor of this model limits the possibilities of imaging an intra-permafrost talik. The need for sensors with a broad amplitude range capacity to record possible deep reflections is a requirement.

The exact solution for energy partition at a standard weathering/bedrock layer interface, which is standard in most land seismic surveys, offers insight into the comparison of these two cases (Figure 2.3, Table 2.2).

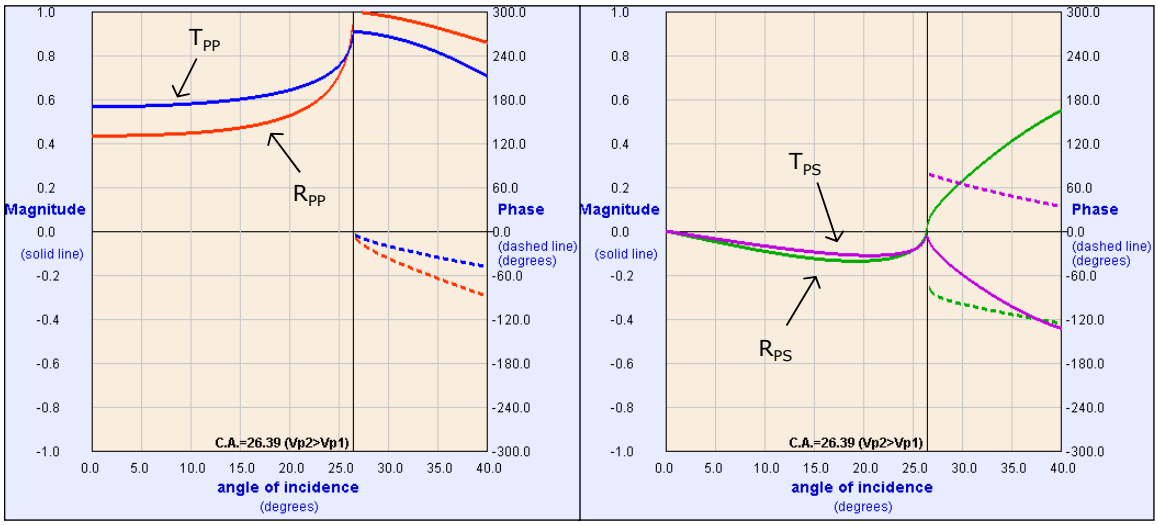

Figure 2.3 Energy partition at a typical weathering-sub weathering type of near surface. R_{PP}, R_{PS}, T_{PP} and T_{PS} are the reflectivity coefficient and transmission coefficient, for PP and PS events, respectively. Dashed and solid lines are the phase and energy partition curves, respectively.

Strata	Thickness	V_P (m/s)	V_S (m/s)	ρ (g/cc)
Weathering	n.a.	800	200	1.6
Sub weathering	n.a.	1800	500	1.8

Table 2.2 Elastic parameters for a typical weathering-sub weathering model. Values taken from Szelwis and Behle *in* Damdom and Domenico (1987)

A larger critical angle of incidence which allows a broader range of homogeneous waves to be transmitted to the subsurface occurs in this model (Figure 2.3). For this case, the transmission coefficient is larger than the reflection coefficient, indicating that more energy is being transmitted than reflected, as opposed to the first model. The converted-wave modes R_{PS} and T_{PS} have a similar trend in both models. Generally, for land seismic surveys, a common convention is to bury the seismic source below the weathering layer. Surface and trapped waves are greatly reduced with this technique.

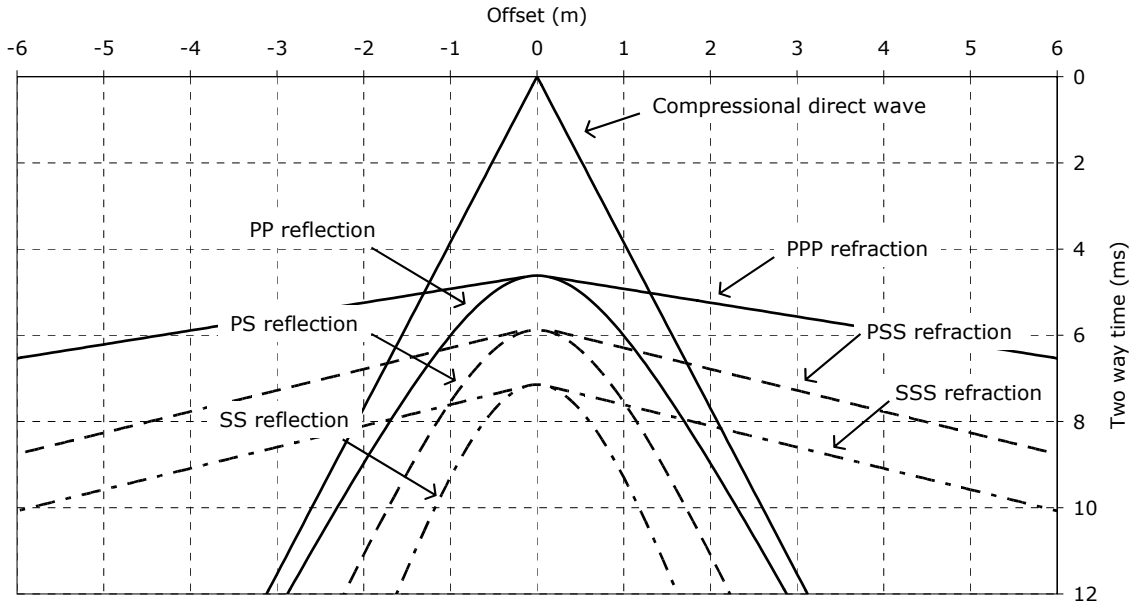

Figure 2.4 Arrival times for various waves propagating in the unfrozen-frozen layered medium. No talik is considered for this example.

Arrival times for different waves were calculated using the previous two-layer periglacial model, and assuming straight seismic rays (Figure 2.4, Equations 2.1 and 2.2). If the head wave event is extrapolated to the zero offset axes, a time value commonly called the intercept time is obtained. For this particular case, the zero-offset reflection two-way time can be approximated by the zero-offset refraction time, even though a head wave at zero offset does not exist. Mathematically, this can be explained using the expressions for reflection and refraction events in a two-layer model flat interface, constant velocity (Equations 2.1 and 2.2, respectively) when the offset is zero and the critical angle of incidence is small.

$$t_{reflected}(x) = \sqrt{t_o^2 + \left(\frac{x}{V}\right)^2} \qquad (2.1)$$

$$t_{refracted}(x) = \frac{x}{V_2} + \frac{2 \cdot z \cdot \cos(\alpha_c)}{V_1} \qquad (2.2)$$

This is the criteria supporting the processing flow used in this research project. The refracted energy is used to image the thawed-frozen layer interface, instead of the reflected energy. The traces are grouped by shot position to apply a Linear Moveout correction (LMO) which flattens the refraction (Figures 2.4 and 2.5). Based on the stacking principle to increase the signal-to-noise ratio, all the traces are summed into a single one located at the source position. The final pseudo-zero offset seismic stacked section is obtained after applying this process for each source point.

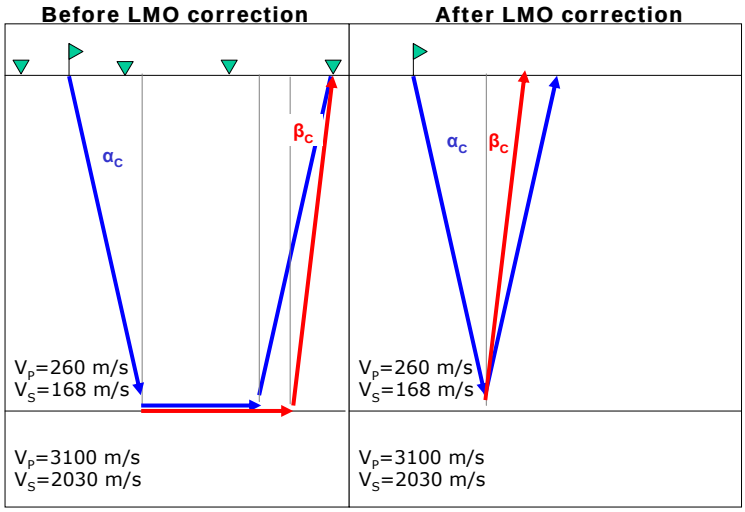

Figure 2.5 Effect of the LMO correction in refracted events. Since the critical angle of incidence is small, the zero-offset time can be approximated with the intercept time of the head wave.

Shallow seismic imaging studies

Seismic refraction data can yield valuable information from the near-surface geology, and sometimes it can also be a useful aid in interpreting shallow reflection data (Reynolds *et al.*, 1990). Analysis of shear-wave reflections has had success in shallow weathering/bedrock interface at 60 m deep (Pullan *et al.*, 1990). These authors found success with shear-wave reflection analyses in areas where the ground roll energy was quickly attenuated and did not interfere with reflection events. The method is optimal when the top layer is unconsolidated.

Norminton (1990) shows by computer modeling that both SH and SV reflections from the bedrock interface should be observable at small angles of incidence, depending on the elastic parameters ratio and the type of incident wave P or SV. The SH wave has an advantage when designing field arrays; it only has one critical angle of incidence. Dufour *et al.* (1996) managed to detect shear head wave arrivals in shot records by analyzing their polarization. Dufour *et al.* showed how the P and S head waves have both rectilinear

polarizations in the vertical and radial component respectively and the Rayleigh waves have elliptical polarization. The use of FK filters was key to enhance the shear head waves in the radial component.

Analyzing several shot records from different locations Jolly *et al.* (1971) demonstrated that the surface wave effect is greatly diminished when the source is located below the weathered layer. Bachrach *et al.* (1998) concludes in his work that there is still need to better understand the seismic response of the near surface. These authors showed how the velocity profile is pressure dependent in the first few meters below the surface. Bachrach *et al.* were able to recognize very shallow reflections, less than 1 m deep, in unconsolidated sediments by applying only a low cut filter.

Xia *et al.* (1999) mentions that shear wave reflections will be possible depending on the dispersion of the unconsolidated layer, *e.g.* if the packet is dispersive resulting from strong velocity gradients near the surface, the groundroll will mask much of the viewing window.

2.2- *Study area*

In a flat area located inside the NASA Haughton-Mars Project base camp, two high-resolution seismic surveys were recorded (Figure 2.6). The target for these surveys was the thawed-frozen layer interface and possible deeper events, such as taliks. High-frequency 40 Hz 3C geophones were used for both surveys. A pellet gun and a 3-lb hammer were the seismic sources for the 2-D and 3-D surveys, respectively.

Figure 2.6 High resolution 3C-2D and 3C-3D seismic surveys, left and right panels respectively. The geophones in the 2D survey are oriented in the N-S direction, while in the 3D the receiver lines are oriented in the E-W direction.

A ground-penetrating radar constant-offset reconnaissance line indicated the presence of a thawed layer (Figure 3.3 in Chapter 3). Additionally, a pit was dug in the study area to take samples and to measure the true depth to permafrost (Figure 2.7). Nieto *et al.* (2003) reports a thickness of 0.6 m for the active layer and describe the active layer in terms of the silt sediment size (Figure 2.7).

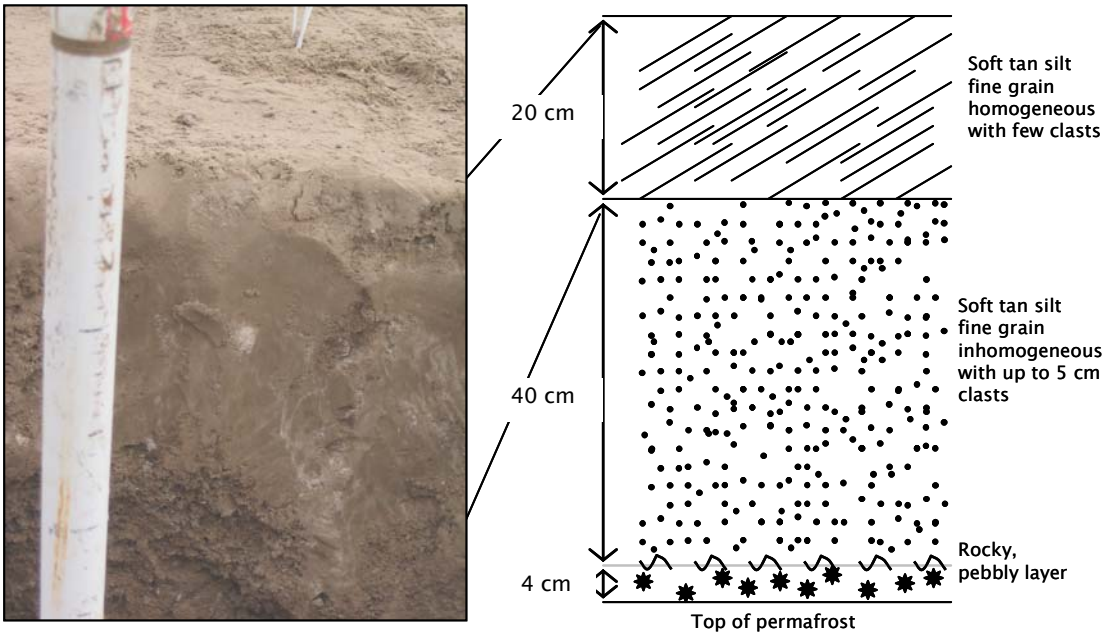

Figure 2.7 Thawed ground profile from the experimental pit. The lithology consists of three units: fine silt, silt with clasts, and rocky layer. At 0.2 m deep a noticeable change in lithology is observed.

The natural frequency of this geophone is 40 Hz, and its spurious frequency occurs at frequencies higher than 400 Hz. The seismic response curve output of this element (Figure 2.8) shows a stable output at frequencies higher than 400 Hz. The range of frequencies used in the project does not exceed 400 Hz, due to the thawed layer attenuation of high frequency components. A Strata View seismic recorder model R60 from Geometrics Inc. allowed recording a maximum of 60 channels. The equipment was originally designed for refraction seismic surveys using single component geophones. It was successfully adapted to multicomponent geophones.

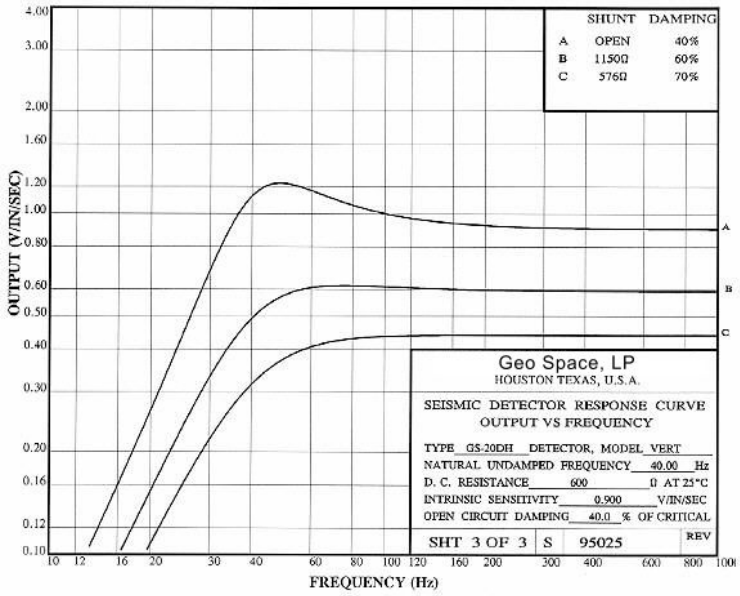

Figure 2.8 Seismic response of the element versus frequency. Observe the stability of the curve for frequencies up to 1 KHz.

2.3- *3C-2D high resolution seismic imaging*

Survey design and acquisition

A high – resolution seismic line, 4 m long, was acquired at the base camp survey site (Figure 2.6). Three-component, high frequency geophones were used along with a pellet gun as the seismic source. The line was set in the N-S direction. The target of the seismic line was to image the top of the frozen layer, as well as any other possible interfaces such as taliks. A geophone element was attached to the barrel of the gun to set the zero time for recording. The gun was used with standard pellets (which were recovered to have low environmental impact). The parameters for this recorded line were (Figure 2.9):

- Receiver station interval: 0.2 m;
- Total of 20 receiver stations;
- 3 channels per station: *vertical* (V), *inline* (H2), and *crossline* (H1);

- Source station interval: 0.2 m;
- Source stations in between two receiver stations;
- Total of 21 source stations;
- Time sample rate: 0.125 ms; and
- Recording time: 256 ms.

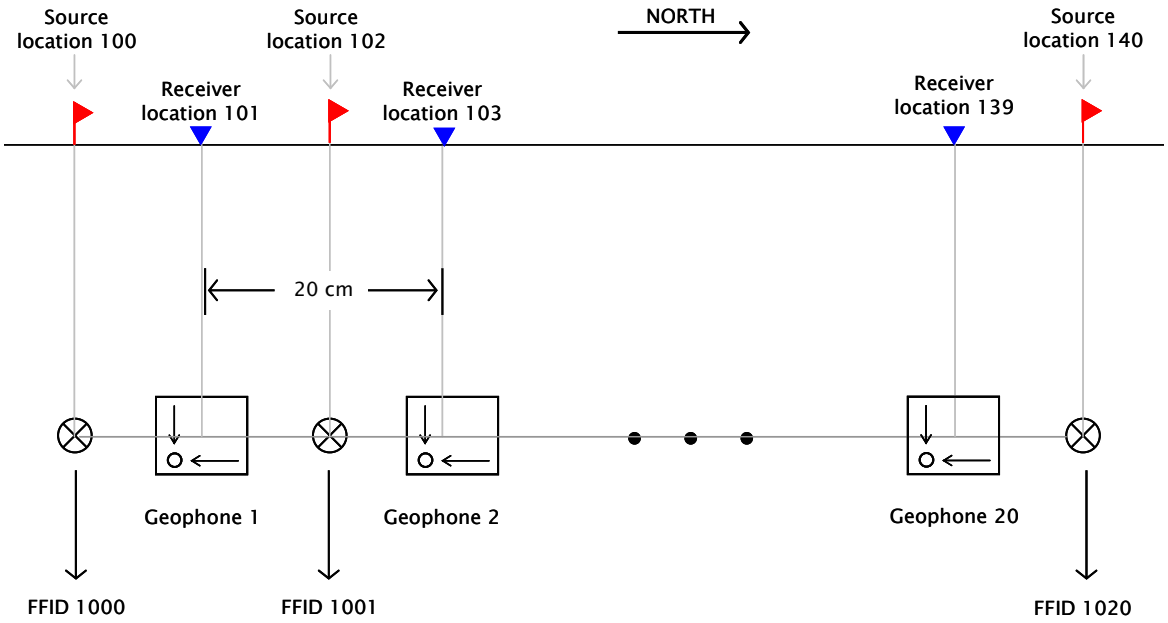

Figure 2.9 Diagram of 3C-2D seismic line. The top part of the diagram shows the location numbers for both receivers and sources. The bottom shows the file number for shots and geophone numbers. The *inline* <<H2>> component is marked by the arrow in the north – south direction while the *crossline* <<H1>> is orthogonal to it.

The survey was recorded with all channels live. Every geophone has three components: *vertical (V), inline (H1) and crossline (H2)*. For every receiver station the H1, V and H2 were connected in the same order as mentioned (Appendix A, Table A.1). Each geophone was oriented in the field such that *the H2 channel* was pointing *south* (Figures 2.6 and 2.9).

The original data was recorded with the corresponding file number and channel number in the header information. Using the channel number, the seismic data were separated into three subsets corresponding to inline, crossline and vertical components. The geophone number was assigned as well using the geophone connection convention presented in Table A.1 (Appendix A). An observer report obtained during the acquisition of the survey (Appendix A, Table A.2) was used to assign source locations to each of the shot gathers, as well as receiver locations. The next step to define the geometry was to assign spatial coordinates to all the traces, which was done by setting the origin of coordinates at the first shot point location.

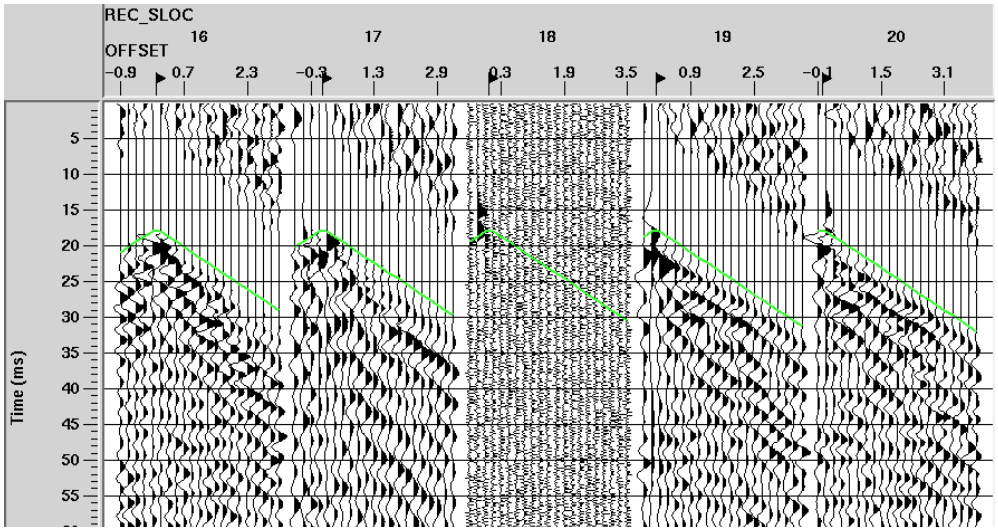

Figure 2.10 Crossline component <<H1>> seismic data sorted by receiver location and offset. All the traces with receiver location 18 were killed due to electronic noise in the seismic recorder.

Up to this point, the data have spatial information, and various domains to be displayed. To check the geometry, the traces were displayed sorted by receiver location and offset (Figure 2.10). The last step in the geometry definition was to define bins and their relations. A bin size of 0.1 m x 0.1 m was defined. The parameters for offset calculation

were: minimum offset of -4 m, maximum offset of 4 m and an interval of 0.1 m. The maximum fold obtained for the full range of offsets was 20.

The position of the horizontal sensors with respect to the labels of the cable connectors and their polarity was obtained by a tap test of the geophones (Figure 2.11). Several time sample rates were analyzed in order to avoid aliasing effects of the first arrival polarity. It has been observed that time aliasing might produce a wrong interpretation of the first break polarity (Bland *et al.*, 2001).

The test consisted in recording three traces (H1, V and H2) for five different tap directions (Figure 2.11), using four different sample rates: 125 us, 250 us, 1000 us and 2000 us. The convention for this project is that a normal polarity corresponds to positive amplitude due to a tap in the direction of the arrows on top of the geophone (Figure 2.11). According to this convention, a normal polarity will correspond to positive amplitude in the *H1* trace due to a *tap in the direction of the H1 arrow* (the same applies to the V and H2 channels).

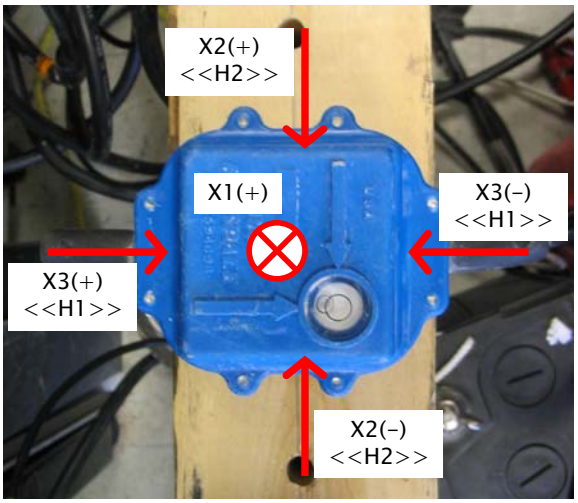

Figure 2.11 Three-component geophones used for all the seismic surveys. The red arrows indicate the tap directions recorded to match the connectors with the sensors, and their polarity.

The cables are labeled as: *H2, V and H1.* For the vertical sensor only a tap on the top of the geophone was recorded.

The results presented in Figure 2.12 indicate the following:

- V channel corresponds to X1 axis and has NORMAL polarity;
- H2 channel corresponds to X2 axis and has REVERSED polarity; and
- H1 channel corresponds to X3 axis and has REVERSED polarity.

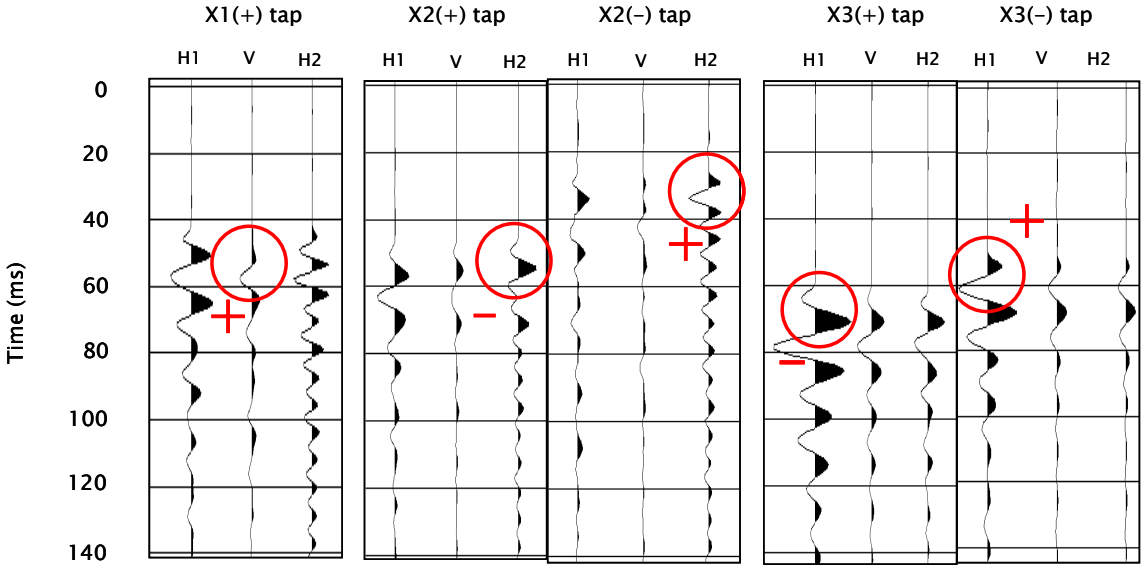

Figure 2.12 Tap test results from high frequency geophones GS-20DH. From left to right: X1(+), X2(+), X2(-), X3(+) and X3(-) tap directions. Each tap test shows three traces: *H1, V and H2*. The amplitude sign is marked by the red circle. The time sample rate used was 1 ms.

Head-wave energy processing flow

Except for providing refraction statics, the energy from the head waves is generally considered as noise in most seismic reflection surveys. After calculating static solutions for the survey, they are often muted from the data. On the other hand, this project treats head waves as signal. The processing objective is to filter out any events, such as direct

waves, or trapped modes and enhance the head wave signature, for a final stack of traces to obtain the pseudo-zero offset section.

The main objective of this project was to image the top of the frozen layer, events inside the permafrost were considered as well, although no physical evidence of these was found. The origin of these structures may be related to water presence, although for this case we are interested in the ones formed by incomplete freezing of the active layer (depth of seasonal frost). Taliks might be seismically imaged thanks to the contrast in elastic properties with the surrounding frozen ground (Table 2.1).

An *experimental processing* flow was applied to define a pseudo-zero offset stacked seismic section (Figure 2.13). Various filtering methods were applied to separate the signal (*head wave*) from the noise (*direct wave*).

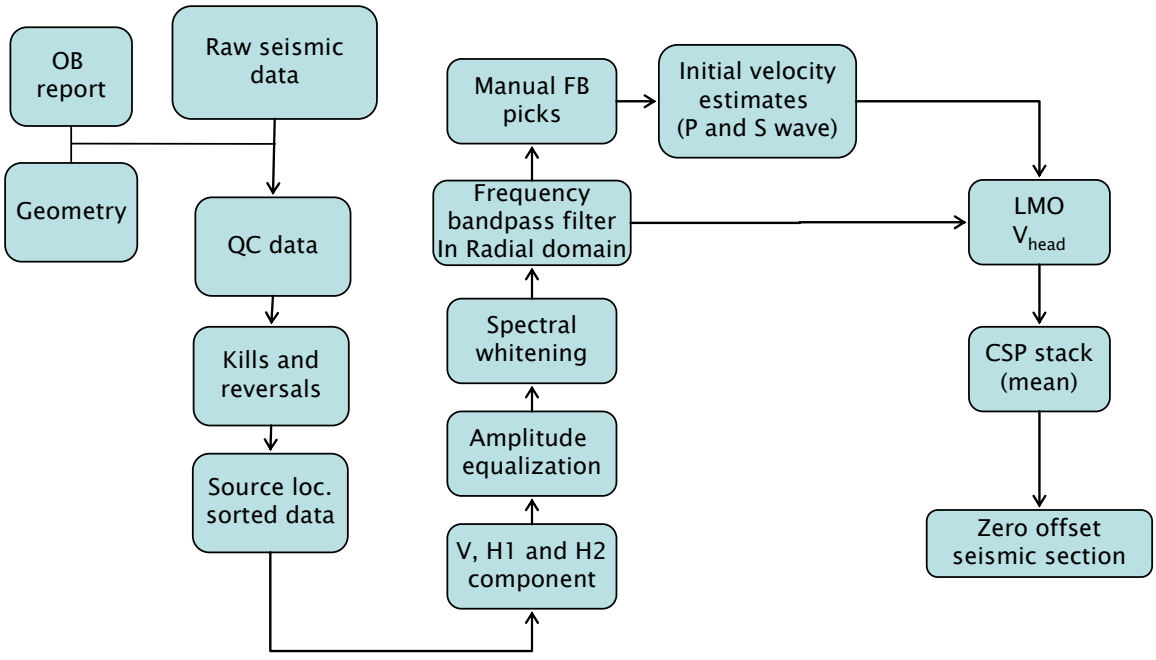

Figure 2.13 Experimental head wave energy processing flow.

The traces from the first shot were sorted and displayed by source location and offset to obtain velocity values (Figure 2.14). A time shift of 15 ms approximately is observed in all the components due to a delay introduced by the pellet gun used as the seismic source. The vertical 'V' component shows three well defined events: (1) the compressional air wave traveling at a velocity of 330 m/s; (2) a compressional direct wave with a velocity lower than the air wave velocity, of approximately 300 m/s; and (3) a compressional head wave <<*PPP*>> from the top of the frozen layer with an approximate velocity of 2500 m/s. The inline 'I' component shows a couple of linear events: (1) the compressional air wave at a velocity of 330 m/s, and (2) a compressional direct wave at a velocity of 300 m/s. The crossline 'X' component shows a very weak compressional direct arrival.

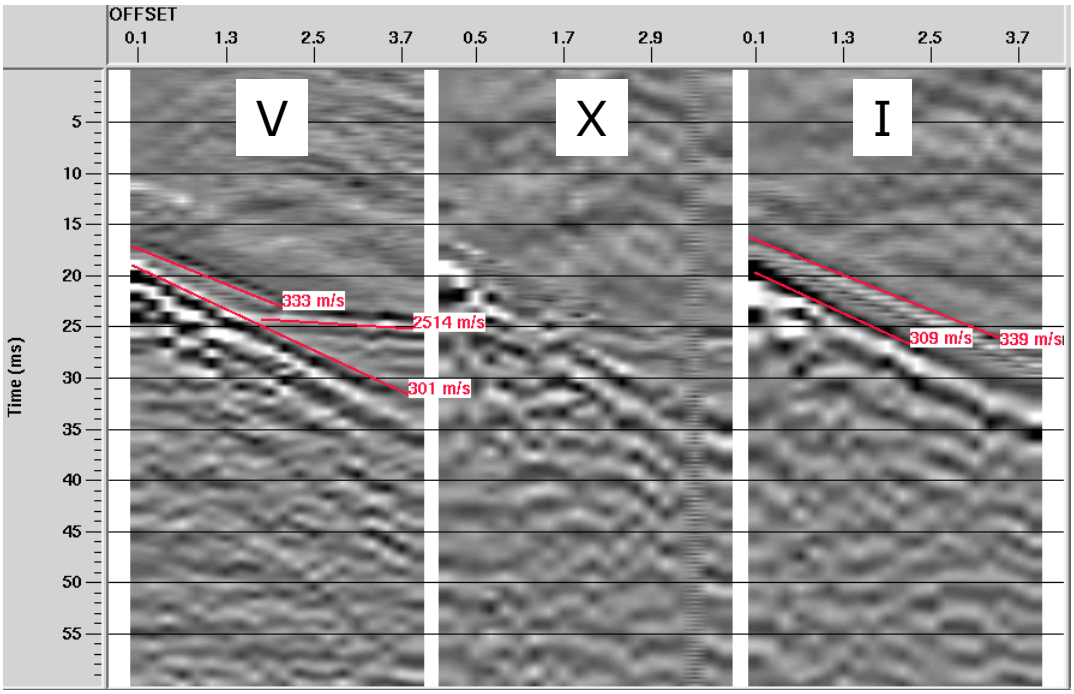

Figure 2.14 Approximate velocities shown in a shot gather from the high resolution seismic line. From left to right: vertical, crossline and inline component.

In terms of frequency content, the head wave has a range from 220 Hz to 800 Hz, while the direct wave has a lower range from 180 Hz to 640 Hz (Figure 2.15). The cutoff dB value used to define these ranges was – 8 dB. This difference in frequency content allows the separation of the noise (*direct wave*) from the signal (*head wave*) in the shot gathers using a simple low cut frequency filter. A reflection event from the thawed – frozen layer interface is expected to occur (since a head wave is observed). For zero – offset there is a small time difference between the direct arrival and the reflected wave, making the two different events hard to resolve. This is one of the reasons why using the head wave for imaging was convenient. No obvious reflections from deeper interfaces are observed.

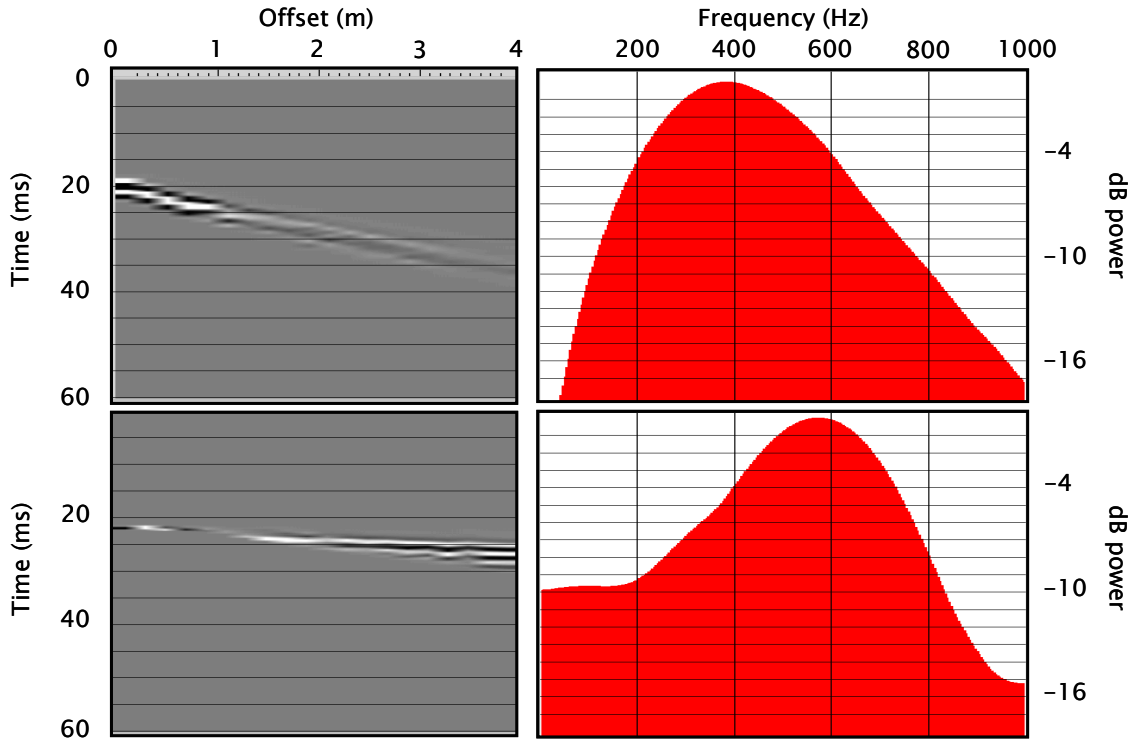

Figure 2.15 Amplitude spectra (right panel) calculated over two different time windows of the shot gather number 100 (left). The top panel corresponds to the direct wave signal and the bottom to the head wave signal. Observe the difference in frequency content.

Vertical and inline components were sorted by source location and offset to obtain an initial estimate of velocities. An application from ProMAX, popular seismic processing software, based on the stabilized power ratio picking was used to obtain first break picks which were later adjusted manually. Velocities were calculated from the time picks using a linear estimation algorithm. The vertical component of the data yields a velocity value of 263 m/s and the inline component yield a value of 256 m/s. In a previous study a compressional direct wave velocity of 260 m/s was estimated from the vertical component data (Nieto *et al.*, 2003). On the other hand, an average velocity of 2244 m/s was estimated for the *PPP* head wave arrivals for the vertical component data (Figure 2.6). Nieto *et al.* (2003) obtained a velocity of 3100 m/s for compressional head waves in a survey located next to a creek.

Kurfurst (1976) obtained ultrasonic wave measurements on different types of soils at permafrost temperatures, from -7º C to +1º C. He found the propagation of velocities to be slower in materials with higher percentage of clays than in those with lower percentage of fines. The velocities obtained range from 1500 m/s to 2900 m/s for inorganic clays. An additional behavior observed was that any increase in natural moisture content in clays resulted in proportionately higher velocities below 0º C (Kurfurst, 1976). King (1984) also found the compressional-wave velocity to be strongly dependant on the fraction of clay-sized particles at temperatures below -2º C, with a weak dependence of porosity. The velocities obtained for samples with a fraction of clay-sized particles higher than 0.40 ranged in average from 1600 m/s to 2800 m/s for temperatures from +5º C to -15º C respectively.

Zimmerman *et al.* (1986) reported compressional wave velocities of unconsolidated permafrost ranging from 2200 m/s to 4210 m/s, depending mainly on the particle size of the soil, which is related to pore size and determines the water/ice ratio. In a series of laboratory experiments Zimmerman *et al.* (1986) observed P and S-wave velocities at a constant temperature of -5º C to be higher for sand than for clay sediment. Clay velocities ranged from 2270 m/s to 3120 m/s for P-waves and from 900 m/s to 1550 m/s for S-waves. An increase of velocity due to a temperature variation from -5º C to -15º C was observed as well (Timur, 1968; Zimmerman *et al.*, 1986). Empirical equations for samples over the porosity (θ) range from 0.30 to 0.50, and water saturation s from 0.00 to 0.6 are obtained by Zimmerman *et al.* (1986) (equation 2.3 and 2.4).

$$V_P = 4.97 - 2.154 \cdot \theta - 2.422 \cdot s \qquad (2.3)$$

$$V_S = 3.043 - 1.698 \cdot \theta - 1.654 \cdot s \qquad (2.4)$$

The P-wave velocities of 3100 m/s and 2244 m/s reported in this work were acquired in different years and at different locations. The first seismic experiment was recorded besides a small creek close to the base camp (Nieto *et al.*, 2003). The second experiment was recorded on a flat area on the top of a hill in the base camp (Figure 2.6). The water content underlying the small creek study area is likely to be higher than in the hill study area, due to intense drying at the hill. The accumulation of water in the creek area may produce greater ice content in the permafrost than on the hill, and thus higher P and S-wave velocities.

Since no head wave arrivals are observed in the crossline component only the vertical and inline component data will be considered. The first step was to balance the amplitude of the data sorted by source location and offset. An AGC operator with a time length of 20

ms was used. The scale factor in each AGC window was calculated using the median of the amplitude samples rather than the mean. The advantage of the median scaling factor over the mean is that it allows enhancing the head wave despite the amplitude difference of five orders of magnitude with the direct wave amplitude (Figure 2.16).

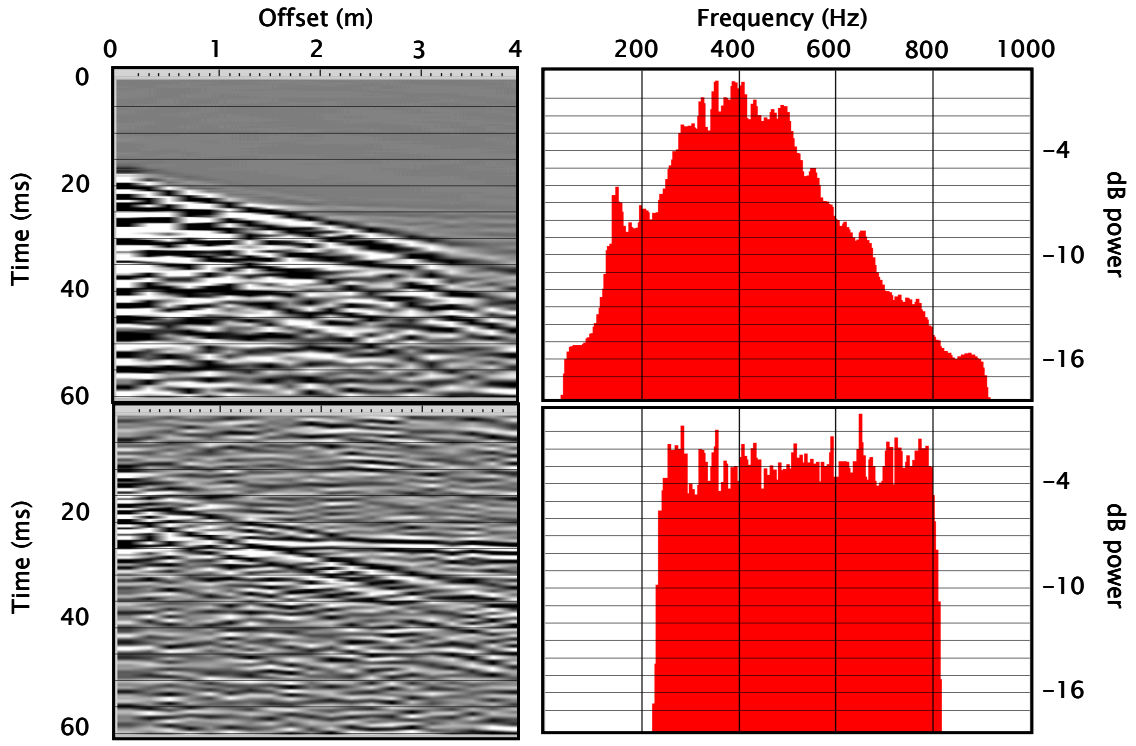

Figure 2.16 Amplitude spectra (right panels) calculated over the shot gather N. 100 (left panel). The top panels are the raw shot gather which has a dominant frequency around 400 Hz. The bottom panels show the same data after an AGC and a spectral whitening correction. Observe how the frequency content has been balanced.

To enhance the high-frequency components of the data a time-invariant spectral whitening function was used. This algorithm works in the frequency domain by applying different gains to individual frequency bands. A total of 10 frequency bands from 210 Hz to 810 Hz were used (Figure 2.16). The method used to restore the amplitude of the traces

was a log average of the individual AGC scalars, which is indicated to be insensitive to large amplitude arrivals, such as near offset direct arrivals.

Following the amplitude balancing and frequency whitening of the data the next processing step applied was to filter out the direct arrival and the air wave responses, and enhance the head wave arrival response (Figure 2.17). Two different frequency bandpass filters were tested: (1) in the *x-t domain;* and (2) in the *radial domain*.

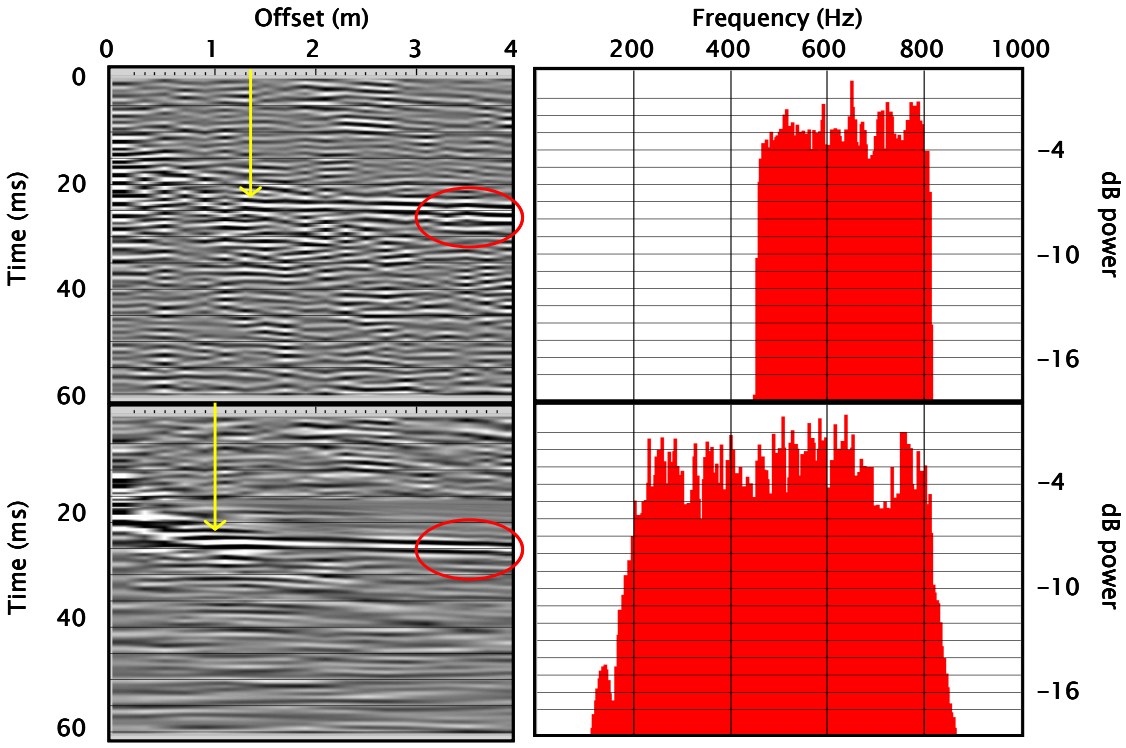

Figure 2.17 Amplitude spectra (right panels) calculated over the shot gathers number 100 (left panels). The top panel is the result from applying a bandpass 460 Hz to 810 Hz filter. The bottom panel shows the same data after applying twice a bandpass filter in the radial domain. Filtering linear noise (direct wave and air wave) is more effectively done in the radial domain.

The first bandpass filter was applied in the *x-t domain*. The pass frequencies were 460 Hz and 810 Hz, respectively. The ramps are formed by Hanning (cosine) tapers in the frequency domain. Both ramps were 10 Hz wide. As a consequence of filtering the data

in the frequency domain (Gibbs's phenomenon) the signal from the head wave is spread out in time (Figure 2.17). Remnants of the direct wave and air wave are observed in the data after filtering it. Another consequence of this technique is that the low frequency component of the signal has to be removed (Figure 2.17).

The second bandpass filtering method was in the *radial domain* which has many advantages for this particular case were the noise to be removed has a linear pattern in the offset – time domain (Henley, 2003). This filter was applied twice since the air wave and the direct wave were to be removed. Using a radial fan filter the data were transformed into the radial domain with the following parameters:

- 200 radial traces (10 times the number of traces in the x – t domain). The interpolation method used was linear;
- Minimum radial trace velocity: -20000 m/s;
- Maximum radial trace velocity: 20000 m/s; and
- Time coordinate for radial trace origin: 0.02 s for the first pass and 0.016 s for the second.

Once the data were transformed to the radial domain, a bandpass filter with frequencies in the range of 50 Hz to 810 Hz for the first pass and 170 Hz to 810 Hz was applied. The ramps for both frequency filters were 10 Hz wide. The data after filtering shows that a more continuous signal is recovered from the head wave (Figure 2.17). No spreading of the signal in the time domain is observed like in the previous case. Also the direct wave and air wave were removed. A broader frequency bandwidth for the head wave signal is recovered after filtering, especially in the range of low-frequency components. The head

wave can be traced up to 1 m offset using the radial domain filtering, while only up to 1.5 m in the frequency domain (Figure 2.17).

The next step in this experimental processing flow was the linear move out correction of the shot gathers (Figure 2.13). Prior to this correction, the data were limited to an offset range from 0.9 m to 4 m, since the near-offset traces have a high amplitude band that distorts the results. The linear move out correction *'t_{LMO}'* depends on the offset *'x'* of the trace and the velocity *'V_{LMO}'* specified (Equation 2.5).

$$t_{LMO} = \frac{x}{V_{LMO}} \qquad (2.5)$$

The correction times from this equation show little sensitivity for large variations of velocities, which in part is a consequence of the small spread and the velocity itself (Figure 2.18).

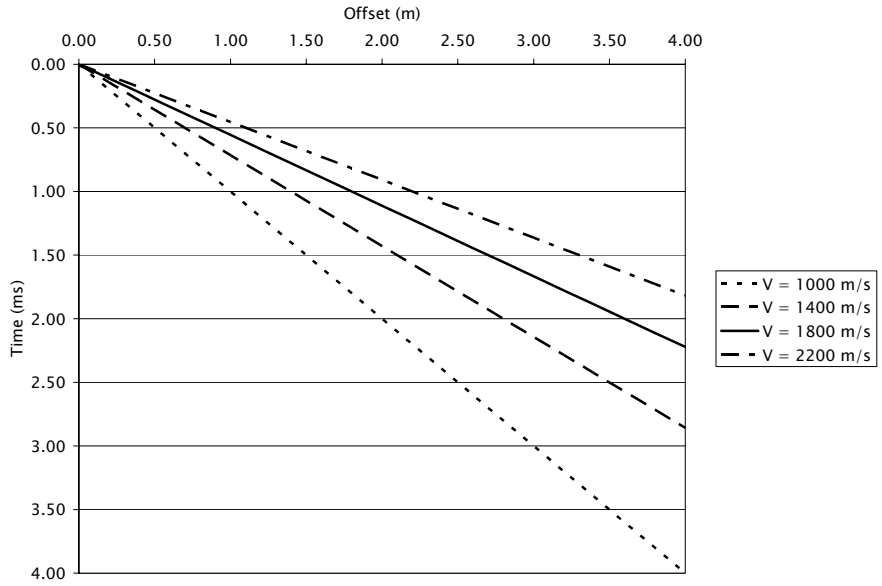

Figure 2.18 Linear move out correction, or offset-dependent static shifting used in the experimental processing flow. Note that the correction is only 4 ms at its maximum value.

A P-wave velocity of 2244 m/s was obtained by averaging the refraction times over all the shot gathers (Figure 2.19). The correction times obtained with velocities higher than the average value of 2244 m/s doesn't show much variation. This is in part due to the small spread used, and the velocity of the frozen layer. A correction LMO velocity of 2000 m/s was used for this line.

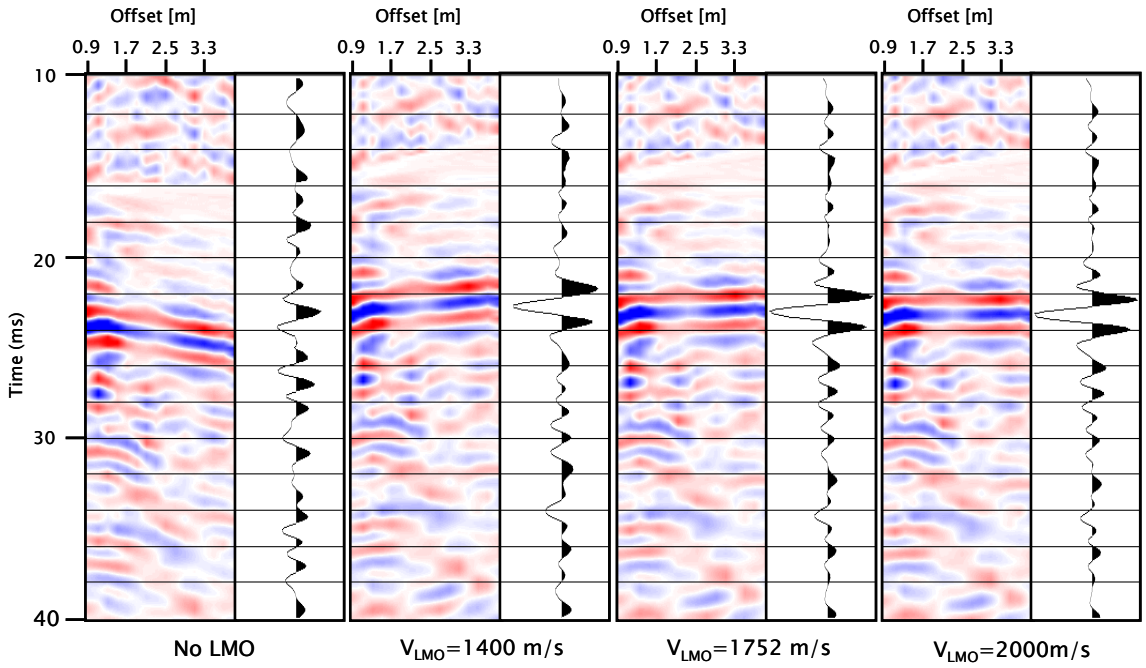

Figure 2.19 Shot gather 100 with offsets from 0.9 m to 4 m and a linear move out correction of: none, 1400 m/s, 1752 m/s and 2000 m/s.

The final step for obtaining an image of the subsurface is stacking and balancing. Little variation of the head wave velocity along the line is observed, however a single linear move out velocity of 2000 m/s was used for all the shots. From every shot gather, a stacked trace was obtained, for a total of twenty traces (equivalent to twenty shot gathers) for all the line. Different stacked sections were obtained using the following LMO velocity corrections: no LMO velocity correction, 1000 m/s, 1752 m/s and 2000 m/s

(Figure 2.20). For longer lines or for 3D surveys this technique could be used to do velocity analyses with different LMO velocity corrections and based on amplitude and continuity of the traces. Additionally this information could be combined to build a stacking velocity model of the surveyed area. The inline component of the data was used to obtain an estimate velocity of the thawed layer, but since the PSS head wave was not recorded, no image was obtained. For longer arrays, a PS seismic stacked section can be obtained (Nieto *et al.*, 2003).

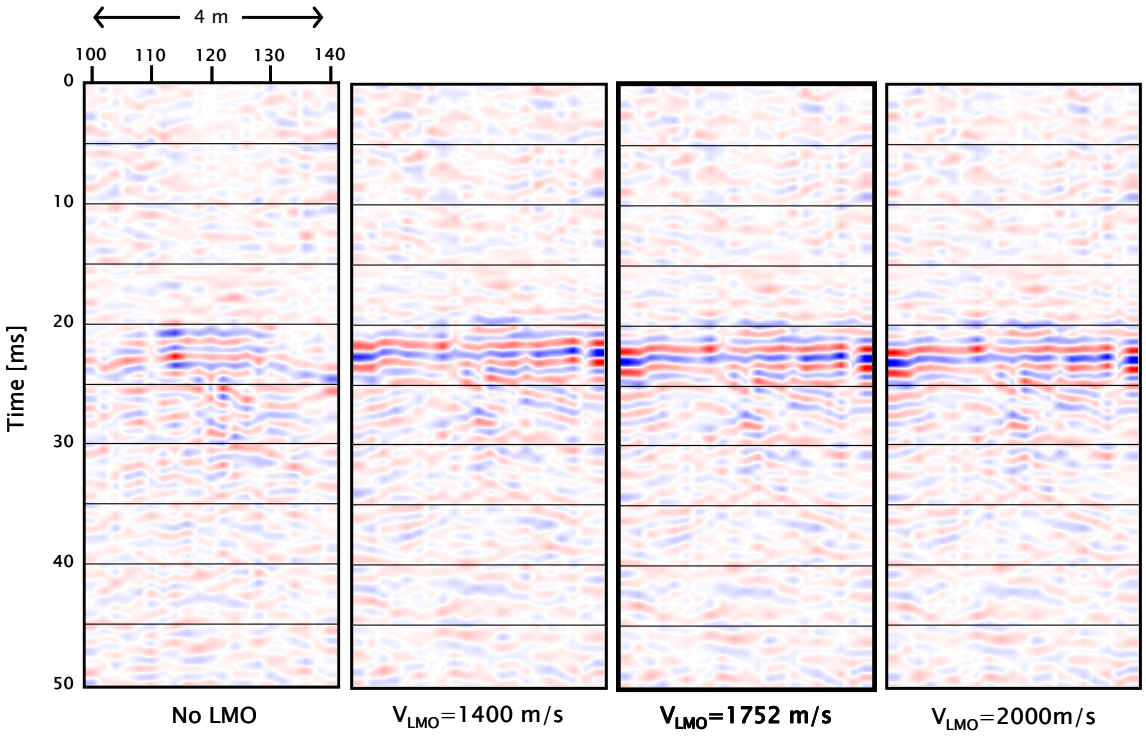

Figure 2.20 Seismic stacked sections obtained from the experimental refracted processing flow. The line is 4 m long and only the top 50 ms is shown. Different LMO velocities show how the highest amplitude is obtained with the correct stacking velocity, however the difference is subtle.

2.4- *3C-3D high resolution seismic imaging*

Survey design and field logistics

A 3C-3D high resolution seismic project was acquired in Devon Island, Nunavut as part of the geophysical program. The survey site was conducted on a flat surface of 25 m^2 inside the perimeter of the HMP base camp (Figure 2.6). The objective of this survey was to image the active layer, and other intra-permafrost events that might be found. Since the depth of investigation is so close to the surface, about one metre depth, issues with reflected energy ratio, attenuation, surface waves, P to S conversion, resolution, and others, were important to understand the process of obtaining an interpretable image. No significant dips are expected to be recorded hence no spatial aliasing represents an issue to the survey. The sample rates used for the survey (Table 2.3) were designed considering subsurface velocities of the study area. Reports from the same area show the presence of a high velocity contrast between the active and the frozen layer (Nieto *et al.*, 2002 and 2003).

Seismic survey parameters	*High resolution 3D*		*Standard 3D*	
	Space	Time	Space	Time
Sample rate	*0.5 m*	*0.125 ms*	*25 m*	*2 ms*
Nyquist frequency	*1 cycle/m*	*4000 Hz*	*0.02 cycle/m*	*250 Hz*

Table 2.3 Sample rates used for the project. Two additional columns with sample rates from a standard 3D seismic survey are shown for comparison.

The temporal Nyquist frequency is an important parameter that points the limit for time aliasing problems. Use of these parameters allows seismic data recording *up to 4000 Hz and 1 cycle/m* frequency without aliasing problems, although 400 Hz is the maximum

frequency expected to be recovered due to attenuation and equipment limitations. When the volume of data is considerably large, it is possible to resample the data to an optimal time sample rate, but in this case was not necessary.

Since we had a restricted number of receiver points (twenty per shot) a large number of shot points were recorded compared to receiver locations. The procedure to record this survey was similar to that of a standard rectangular 3D seismic exploration survey, but on a smaller scale. We used a rectangular recording spread formed by two receiver lines and ten stations per line (Figure 2.21). Since we were constrained by the number of receivers to a maximum of twenty, a more dense shot coverage was used. The parameters of the survey were defined as highlighted below:

- Source points spacing of 25 cm;
- Source lines spacing of 50 cm;
- 9 source points per source line centred;
- 13 source lines per recording unit;
- Receiver stations spacing of 50 cm;
- Receiver lines spacing of 50 cm;
- 10 receiver stations per receiver lines; and
- 2 receiver lines per recording unit.

A recording area patch defined as a *swath* from now on, consists of a fixed position of receiver stations for several source stations. The total number of source points per swath was 117 (Figure 2.21). To cover the study area we recorded five swaths moving the receiver lines 1 m at a time without overlap (Figure 2.23). In this type of survey the use of a plastic grid marked with source and receiver positions would be very useful addition

to avoid the possibility for human errors, and accelerate the recording process. Once the swath has been finished, the grid will be moved to a new position and the source points will be marked automatically as well.

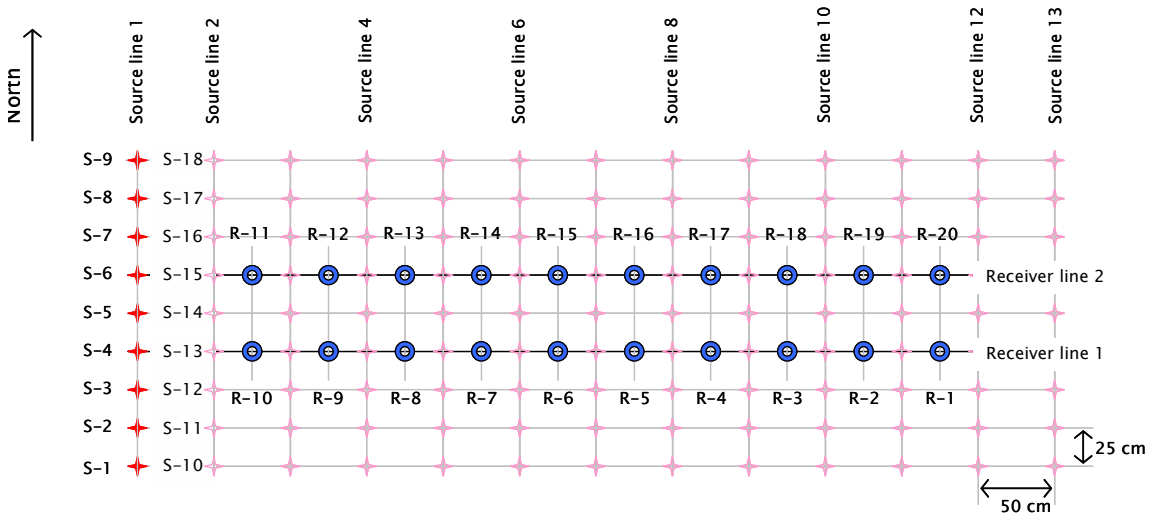

Figure 2.21 Recording unit for 3C-3D seismic survey. Red crosses indicate shot points and blue circles indicate receiver stations.

The survey was recorded over three days. Some time was lost during the survey because of heavy rain that caused strong noise level on the geophones. The source used in this survey was a 2 Kg hammer. A metal washer was centred at the shot point to use as the impacting base for the hammer. A trigger was attached to the hammer for zero – time recording. Only one geophone per station was used for this seismic survey. The geophones were oriented in such a way that the *arrow of the H2* direction was pointing towards *south*. To use the three component geophones we had to connect the seismic cable starting with the H2 channel, following the vertical and then the H1 channel (Figure 2.22). Once all the shot points for a swath were acquired, we moved the receiver spread

(geophones + seismic cables + seismic recorder) one metre north, without overlapping receiver lines (Figure 2.23).

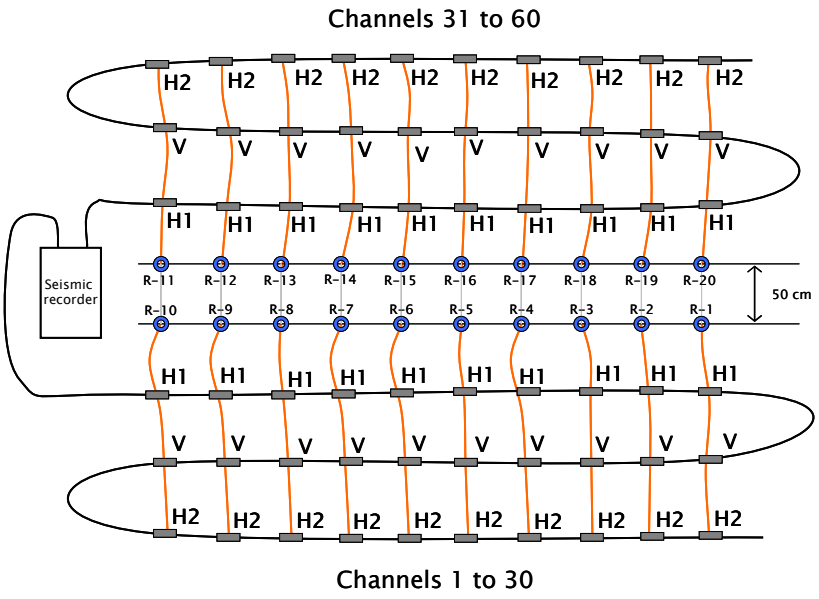

Figure 2.22 Diagram showing the connection of 3C geophones to the seismic recorder.

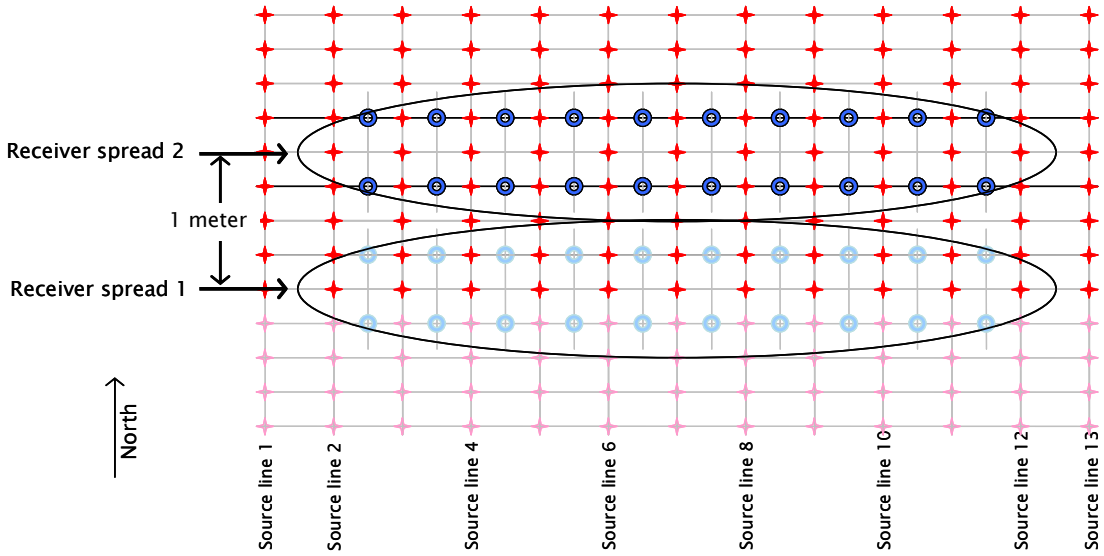

Figure 2.23 Diagram showing the advance of a swath.

Pre-processing (geometry and trace header edit)

The raw data were saved in a format used by seismic refraction recorder systems defined by a "dat" extension. This was transformed to standard "sgy" format, verifying that the file number and the channel number on the trace headers were conserved, as well as the amplitude content. Once the data were correctly converted, we uploaded it into the processing software (ProMAX). The first step to set up the geometry was to separate the data into three different sets corresponding to sensor position: *vertical* <<V>>, *inline* <<H1>> and *crossline* <<H2>>. The three components are defined as in the previous 2D surveys. The order in which the traces were originally sorted was file number and channel number. The channel number corresponds to a specific geophone number and sensor position (Figure 2.22 and Appendix A-Table A.3). The geophone number of each of the three datasets was defined from the channel sequence numbers as a reference, using a simple formula (Table 2.4). The range of the geophone numbers goes from 1 to 20 (Figure 2.22). The data now has a consistent geophone number on each of the components (Figure 2.24).

Channel number ranges	Geophone number formula
1 to 10	= chan
11 to 20	= 21 – chan
21 to 40	= chan – 20
41 to 50	= 61 – chan
51 to 60	= chan - 40

Table 2.4 Formulae to define the geophone number of the traces from the channel number.

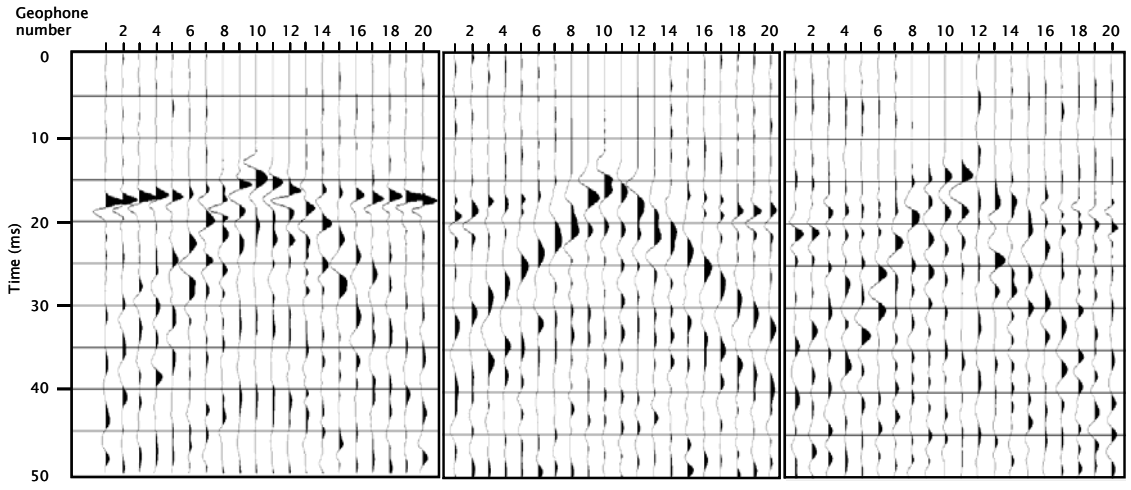

Figure 2.24 Seismic data from shot file number 4012. From left to right, we observe the vertical component, inline (H1) and crossline (H2). An AGC filter of 30 ms with a bandpass frequency filter was used for the display. Notice the presence of a prominent PPP head wave in the vertical component, and a consistent direct arrival in the inline component.

Once the data had the geophone number information on the headers we continued with defining receiver and source locations using a survey grid as a reference. The survey station numbers were defined in a rectangular grid with a unit separation of 0.25 m. The origin of coordinates for the grid was located in the south western corner outside the study area. The station number consists of 2 numbers: “aabb”. The “aa” corresponds to the line station number in the east – west direction, and the “bb” corresponds to the ones in the north – south direction (Figure 2.25). For example 1219 corresponds to the station located 2.75 m (11 stations times 0.25 m) east and 4.5 m (18 stations times 0.25 m) north of the station 0101 (south western corner of the survey area).

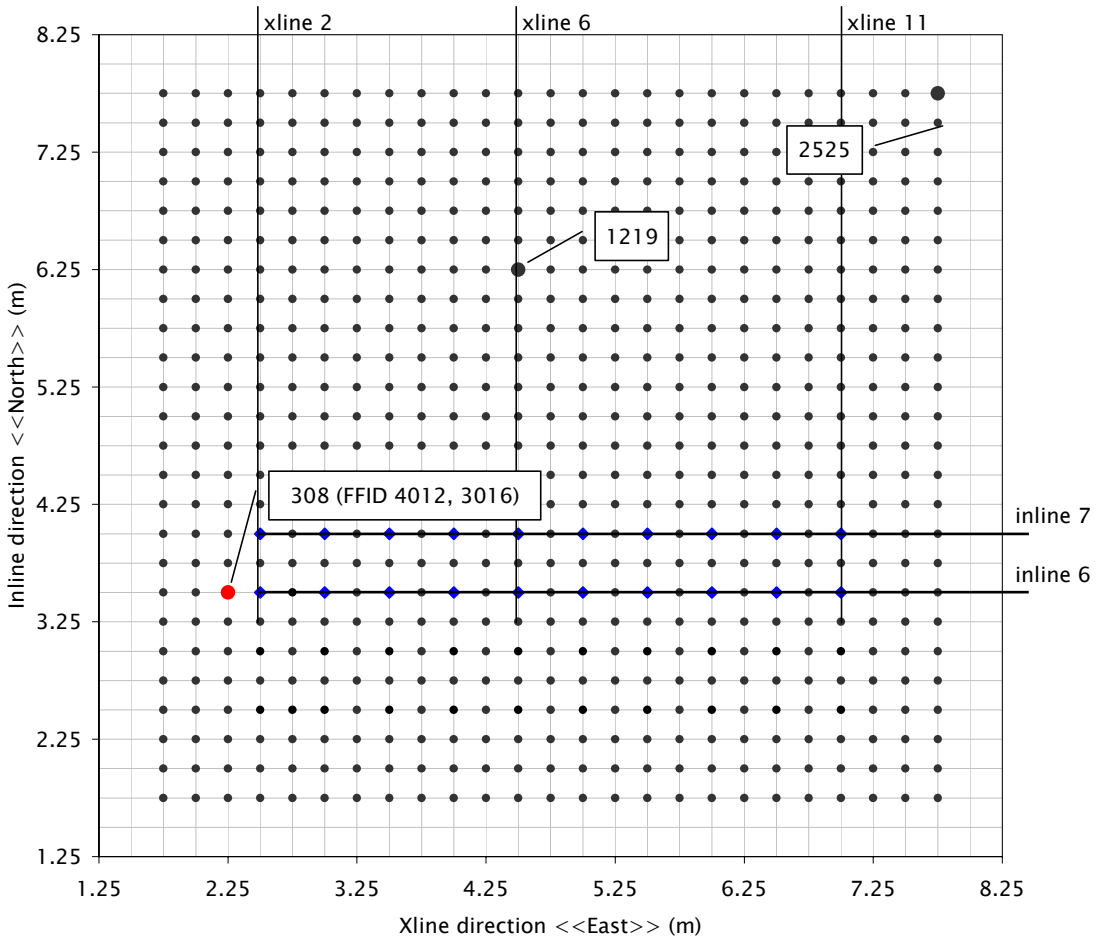

Figure 2.25 Survey grid used for the 3C – 3D high resolution seismic project. The scale used in both axes is centimeters. Some stations are marked for clarification.

The field notes were used to define an observer report that relates the file number and recording channels to the source and receiver stations (Appendix A). The source stations were matched to the file numbers (Table A.4, Appendix A) and the receiver stations were matched to the geophone numbers (Table A.5, Appendix A). After the traces were fed with receiver and source stations, a survey file with spatial coordinates (Table A.6, Appendix A) was loaded as well and completed with this the geometry. To make sure that the geometry is correct, a time gate was picked for one gather and propagated through the rest of the gathers and sorted by source and receiver locations.

The last step in the definition of the geometry was binning the data. The theoretical bin size was 0.125 m x 0.25 m, but we used a square bin size of 0.25 m x 0.25 m. Offsets were calculated using as a reference 0.25 m, 5.5 m and 0.125 m for minimum, maximum and interval respectively. The maximum fold obtained for the full range of offsets was 60 (Figure 2.26). The acquisition footprint was a consequence of the limited number of geophones for the survey, although it is not so marked for the target depth (Figure 2.26).

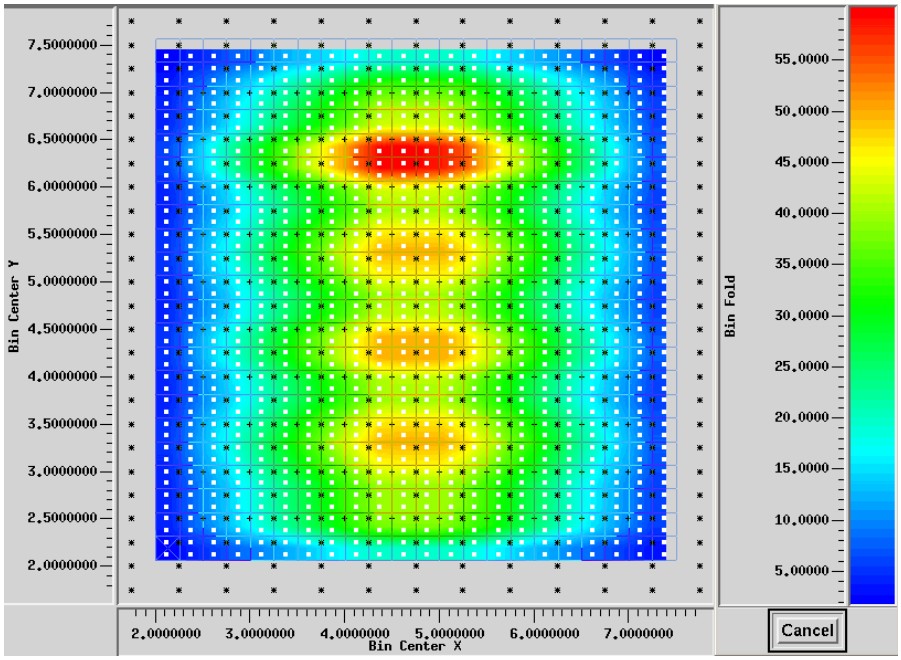

Figure 2.26 Fold distribution obtained for the 3C – 3D survey. The bin size was 0.25 m x 0.25 m.

3C rotation analysis

Tap test of the geophones indicate that the response for each component vary. This conclusion could be biased by the fact that the strength of the tap in different directions was not constant. In order to find if the response varies, or is constant, between the horizontal components, a number of traces with different azimuths were analyzed: 45º,

135º, 225º and 315º (Table 2.5). All angles are measured clockwise from the source location looking at the receiver location. For reference, the north direction has 0º azimuth, and 90º azimuth for the east direction.

SR azimuth	Offset	H1 polarity	H2 polarity	Source loc.	Receiver loc.
45º	0.35	Normal	*Reversed*	1111	49
135º	0.35	Normal	Normal	1515	54
225º	1.77	*Reversed*	Normal	909	1
315º	1.77	*Reversed*	*Reversed*	1305	26

Table 2.5 Parameters of location and orientation of the traces analyzed for the rotation correction.

Significantly, this analysis indicates that the energy recorded by the H1-H2 components at different azimuth values is equal and therefore no variation is observed between them. In 3D geometries positive offsets are calculated when both the geometry and the azimuth of the source-receiver point is assigned. This process helps when dealing with *shear waves*. The importance of controlling the position of the source and receiver is due to the nature of shear waves, as they have a polarity sign change with change in the offset sign. In other words, a polarity reversal occurs whenever source and receiver position are interchanged (Figure 2.27). The direct and refracted events recorded by the horizontal components H1-H2 of the geophones show this polarity reversal (Nieto *et al.*, 2002). The behavior observed in the horizontal components H1-H2 at various azimuth values agrees with the expected theoretical results (Table 2.5 and Figure 2.27). An additional issue when dealing with shear waves in 3D geometries is the orientation of the sensors in the field and the orientation for processing. At the time of acquisition a specific orientation is fixed for all sensors. For this 3D survey the convention used was H2 pointing towards

south. Generally for processing the horizontal components have to be rotated from the H1-H2 field directions to the *radial-transverse*. The elastic energy is recorded by both horizontal sensors fixed in a constant direction.

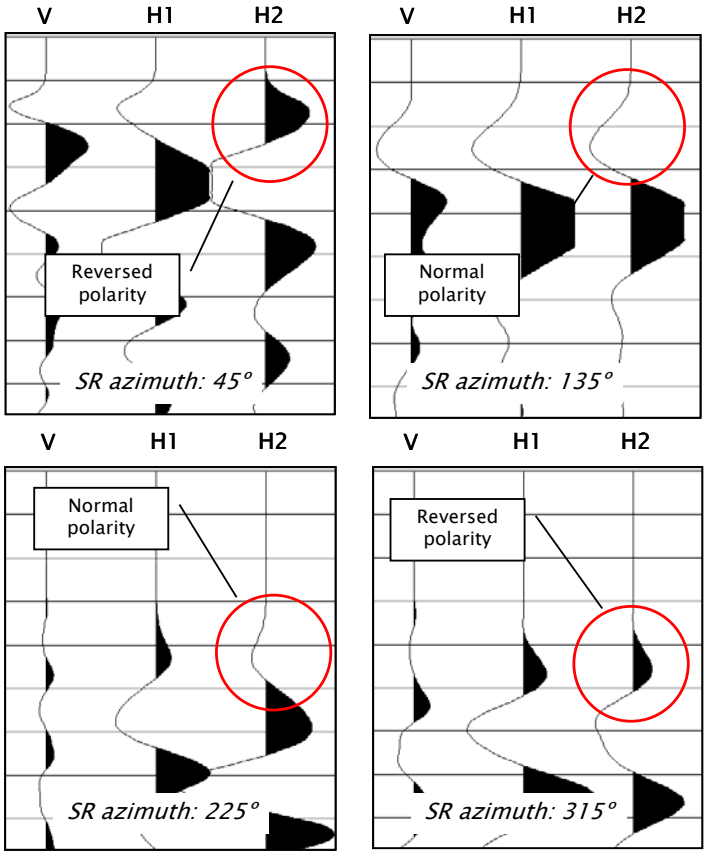

Figure 2.27 Display of V-H1-H2 sets of traces from various source-receiver pairs. Top to bottom, left to right each diagram has a different azimuth and offset value: 45º-0.35 m, 135º-0.35 m, 225º-1.77 m and 315º-1.77 m. Observe how the H1 component traces change polarity between 0º-180º (top) and 181º-360º (bottom). In the same way, H2 component traces change polarity when the azimuth value is in the range 0º-89º or 271º-360º.

The objective of rotating the H1-H2 horizontal traces is to find the direction of *maximum energy* that is defined as *radial* and the direction of *minimum energy* that is defined as *transverse*. By definition the radial and transverse directions are orthogonal. Various methods have been developed to find the angle of rotation (*e.g.* Guevara, 2001).

Generally these methods require the use of either first break picks, or time windows, to obtain the angle were a maximum level of energy is reached (DiSiena *et al.*, 1984). Normally this method uses first breaks, or event(s) in both horizontal components. Other methods consist of using hodograms, which are a plot of the H1 versus H2 amplitudes to define an angle of maximum energy for a particular event. This method requires the presence of clear events as well. A more automated method *geometrical rotation* uses the geometrical angles of source receiver pairs (azimuth) to rotate the H1-H2 into radial and transverse positions, as if the geophones were oriented towards the source location. All of these methods are implemented in the Matlab environment and compared to the geometrical rotation to estimate the error among them. The inputs for this comparison are the traces chosen for the polarity analysis (Table 2.5).

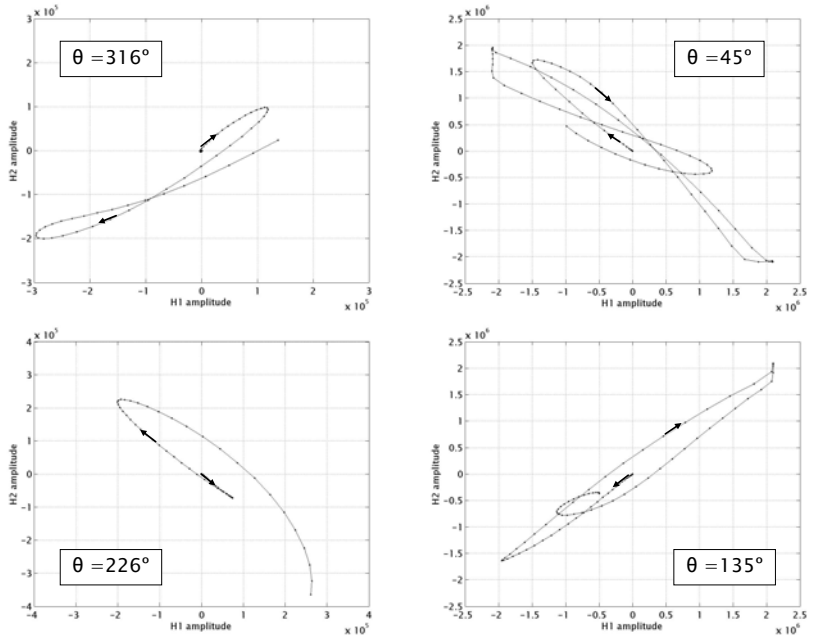

Figure 2.28 Hodograms for traces at different source receiver azimuths: 45º, 135º, 225º and 315º. Each display consists of H2 amplitudes (vertical axis) versus H1 amplitudes (horizontal axis).

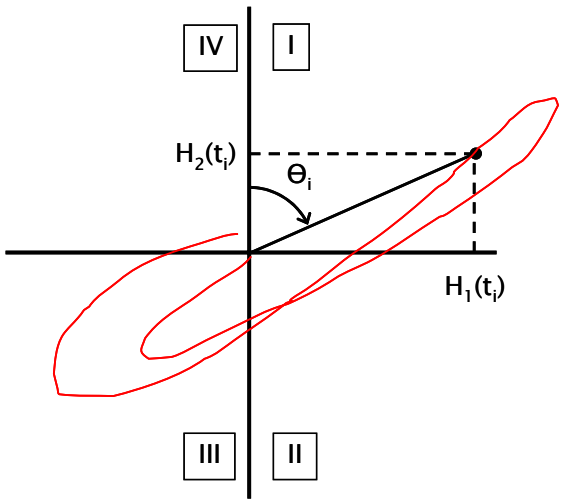

Figure 2.29 Hodogram diagram example. The horizontal and vertical axes correspond to the H1 and H2 components respectively. To calculate the vector θ_i for a complete cycle, the space was subdivided into four quadrants according to their azimuth: (I) 0 to 90, (II) 90 to 180, (III) 180 to 270 and (IV) 270 to 360. The origin for azimuth values points towards positive H2 amplitudes and the angles are measured clockwise.

The first method tested, *hodogram analysis*, allows a visual inspection of the polarization characteristics of the analyzed event. The time window chosen for the amplitude extraction is from 10 ms to 24 ms for all the traces that contain a clear direct event. Traces at different azimuths allow the observation of the variation of polarity of sensors according to their position (Figure 2.28). A good approximation of the rotation angles can be estimated from observing hodogram displays. The uncertainty of these measures is high due to its dependence on visual estimation of the rotation angles. A method that allows obtaining an estimate based on the amplitudes of H1-H2 components (Figure 2.29) was developed by DiSiena *et al.* (1984). This method consists in obtaining instantaneous angles of rotation $\theta(t_i)$ from Eq. 2.6, and defining a histogram of the resultant angle. The vector $\theta(t_i)$ can be weighted using $r(t_i)$ or $r^2(t_i)$ (Eq. 2.7) in the

presence of noise in both components, but this is not the case for this dataset. The origin and direction of measuring the angles is arbitrary, but should be consistent.

$$tan\ (\theta_i) = H_1(t_i) / H_2\ (t_i) \qquad (2.6)$$

where, $\theta_i = \theta(t_i)$

$$[r_i]^2 = [H_2(t_i)]^2 + [H_1\ (t_i)]^2 \qquad (2.7)$$

where, $r_i = r(t_i)$

Once the vector θ_i has been obtained a histogram has to be defined. The number and width of bins to be used may vary according to the distribution of angles obtained. For this case the bins were chosen to be 5º wide, for a total of 72 bins for a complete cycle (Figure 2.30). The azimuth angles obtained by using this method show small differences compared to the geometrical angle from the survey (Table 2.6).

Source loc.	Receiver loc.	SR azimuth (geometrical)	Geometrical rotat. angle	Histogram method	
				Rot. angle	Error (%)
1111	49	45º	135º	135º	0
1515	54	135º	225º	225º	0
909	1	225º	315º	314º	0.3
1305	26	315º	45º	44º	0.3

Table 2.6. The rotation angles using the histogram method coincide with the angles obtained from the geometrical measures.

Realizing that the error from using the geometrical angle of rotation is less than 1%, the automatic rotation of H1-H2 components into radial-transverse is chosen. This choice is made because otherwise it would represent an analysis of an approximate of 100,00 traces for this 3D survey. The geometrical rotation method is based on a simple equation

(Eq. 2.8). DiSiena *et al.* (1984) developed a technique to orient geophones in VSP surveys and that is used in this project to rotate the horizontal components towards the source location (Figure 2.31).

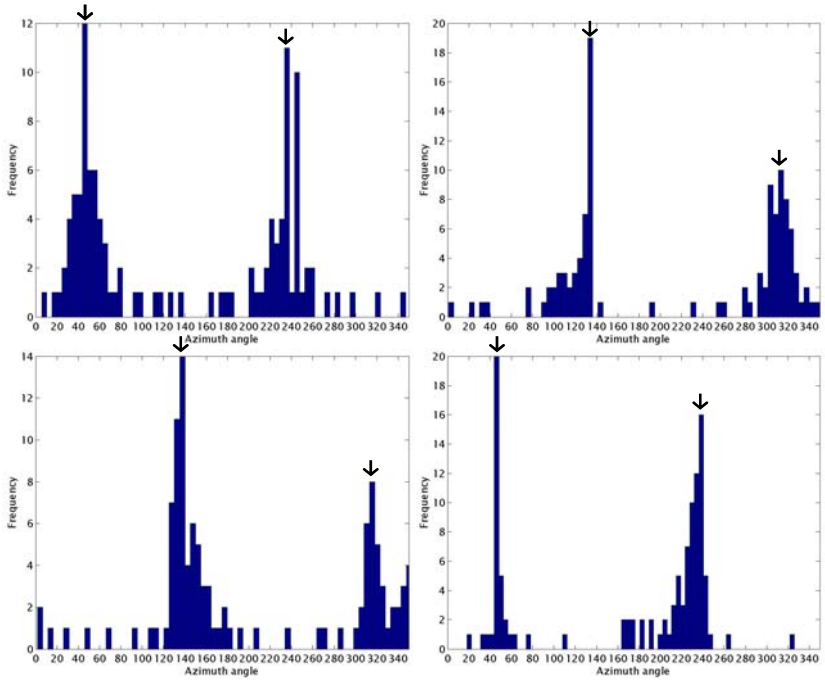

Figure 2.30 Histogram for rotation angle calculation. The horizontal axis shows the angle values ranging from 0º to 360º. The vertical axis corresponds to the frequency of samples that fall into a specific bin. The black arrows indicate the position of a maximum energy, which corresponds to the rotation angle.

The energy from H1 and H2 components is used to calculate both the radial and transverse new components using equation 2.8.

$$x' = M \cdot x \qquad (2.8)$$

where

x': columns vector with rotated components;

x: column vector with field components; and

M: transformation matrix.

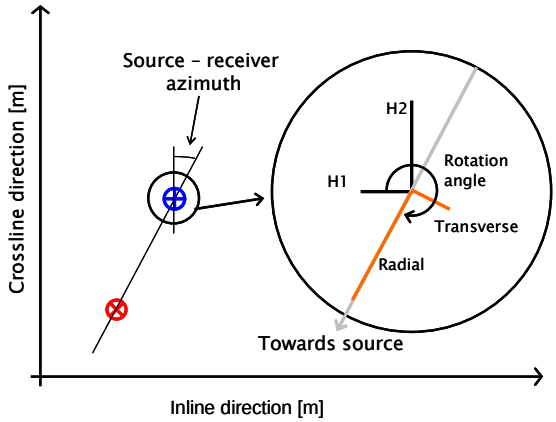

Figure 2.31 Technique for geometrical rotation of horizontal components. The red circle indicates a source location while the blue circle is a 3C receiver location. After a clockwise rotation of the H1-H2 components into radial-transverse is using the respective azimuth angle, every geophone was pointing towards the source.

Consider the traces from source location 1111 and receiver location 49, which has a geometrical azimuth of 45º. The rotation angle for this case is 135º, obtained from its azimuth angle. A series of traces rotated at various angles show continuously how this pair of traces changes its amplitude until it reaches a maximum exactly for the rotation angle equal to 135º (Figure 2.32).

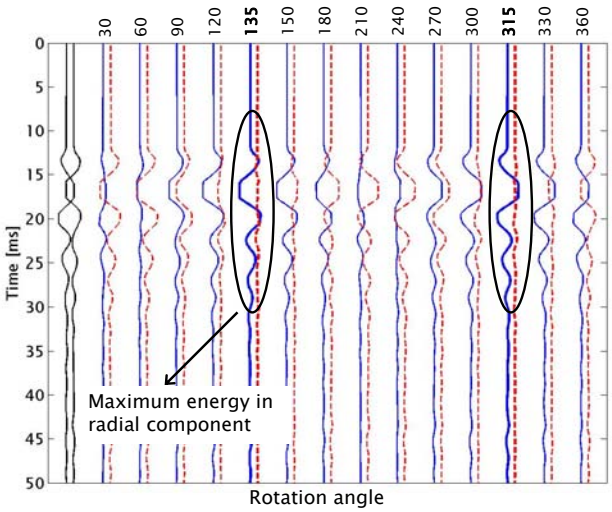

Figure 2.32 Rotated traces from the original H1 – H2 component at source loc 1111 and receiver loc 49 (in black). The source-receiver azimuth for this pair of traces was 45º. The blue

solid traces represent the radial component and the red dashed line the transverse component. Observe how the energy increments and decrements as the rotation angle vary, until a maximum is reached in the radial component for 135º.

A comparison between them is done to assure that the rotation algorithm of the processing software used (ProMAX) was congruent with the theory that was used in the previous analysis (Figures 2.33, 2.34, 2.35 and 2.36).

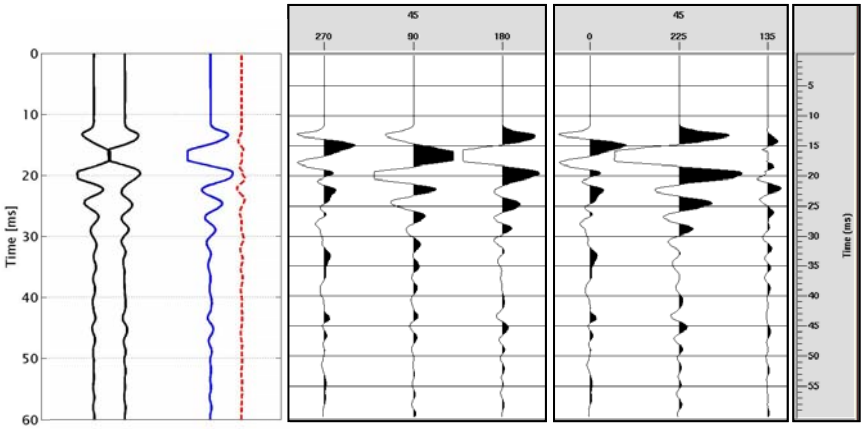

Figure 2.33 H1-H2 rotated trace from source-receiver azimuth 45º.

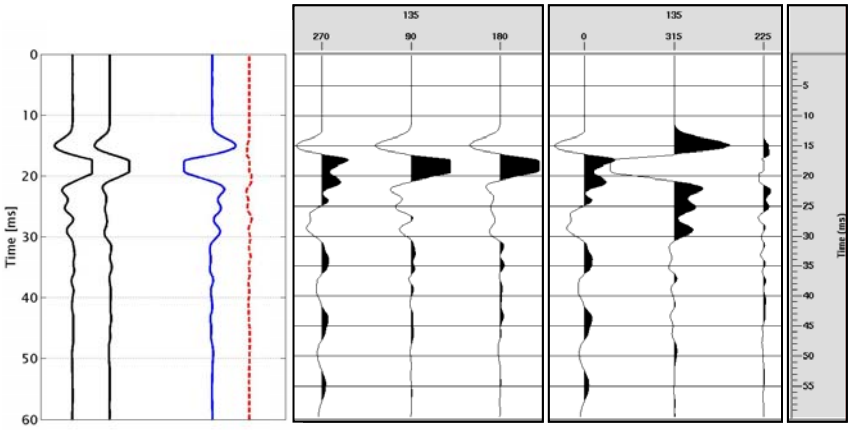

Figure 2.34 H1-H2 rotated trace from source-receiver azimuth 135º.

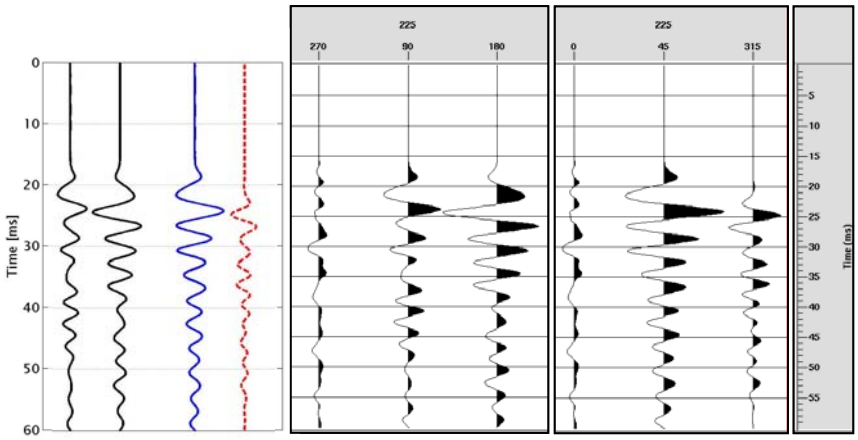

Figure 2.35 H1-H2 rotated trace from source-receiver azimuth 225º.

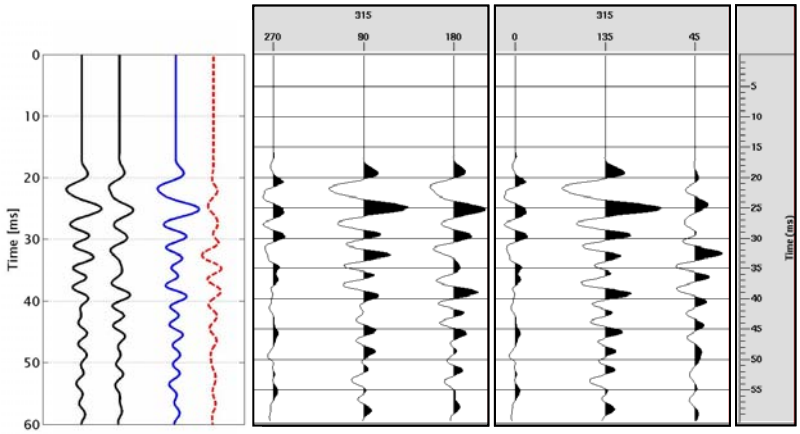

Figure 2.36 H1-H2 rotated trace from source-receiver azimuth 315º.

To fully comprehend the limitations of the rotation algorithm in ProMAX, traces from source-receiver azimuths of 90º were included. This was done since a display of the data after rotation revealed that the traces at these angles were not being rotated properly (Figure 2.37). It was found that the resultant traces after the rotation was applied have incorrect amplitudes because of a improper use of angles (Figure 2.38). Since it only occurs for traces which have source-rotation azimuths of 90º, a simple reversal filter served to correct this mistake (Figure 2.37).

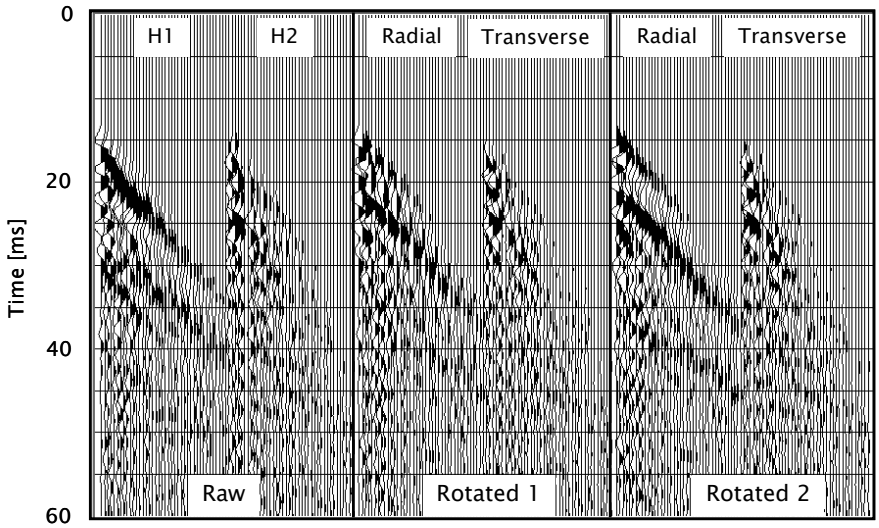

Figure 2.37 Horizontal component traces from source and receiver location 108 and 1 (chosen since most of the azimuths here are around 90º). From left to right: H1 and H2 components with no rotation; radial and transverse traces with no 90º correction; and radial and transverse traces with correction. Rotation effect manifests as the polarity reversals observed in the centre panel.

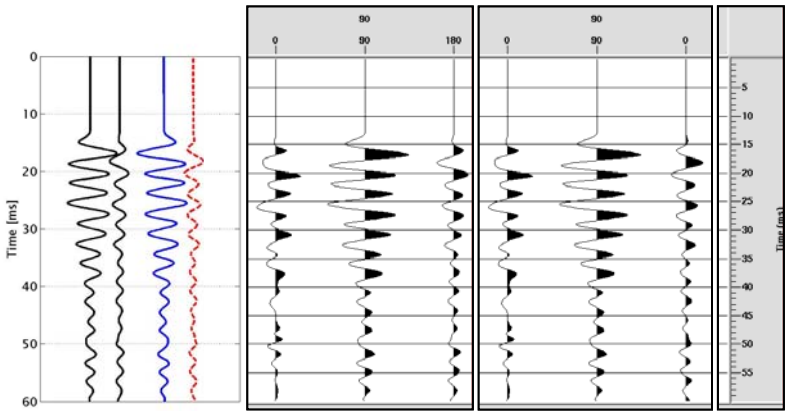

Figure 2.38 H1-H2 rotated trace from source-receiver azimuth 90º. The left panel shows H1 and H2 traces in black (before Matlab rotation) and colour (after Matlab rotation). The right panel shows V, H1 and H2 traces before ProMAX rotation (left) and after rotation (right). Notice the inconsistency between the blue trace in the left panel (radial Matlab trace) and the black trace in the centre of the far right panel (radial ProMAX trace).

Processing head wave energy of 3C-3D seismic

A similar experimental processing flow was applied to the high resolution 3C-3D in order to obtain a comparable seismic image of the subsurface. A problem included in the

definition of subsurface images when 3D acquisition geometry is used is anisotropy. If the study area has azimuthally anisotropic layers then a variation of arrival times with angle is recorded (Leslie *et al.*, 1999; Vermeer, 2001). A plot of *vertical* traces from a CMP sorted by offset for two different azimuth ranges shows the material to be isotropic (Figure 2.39). This conclusion is based on the absence of variation of arrival times with azimuth.

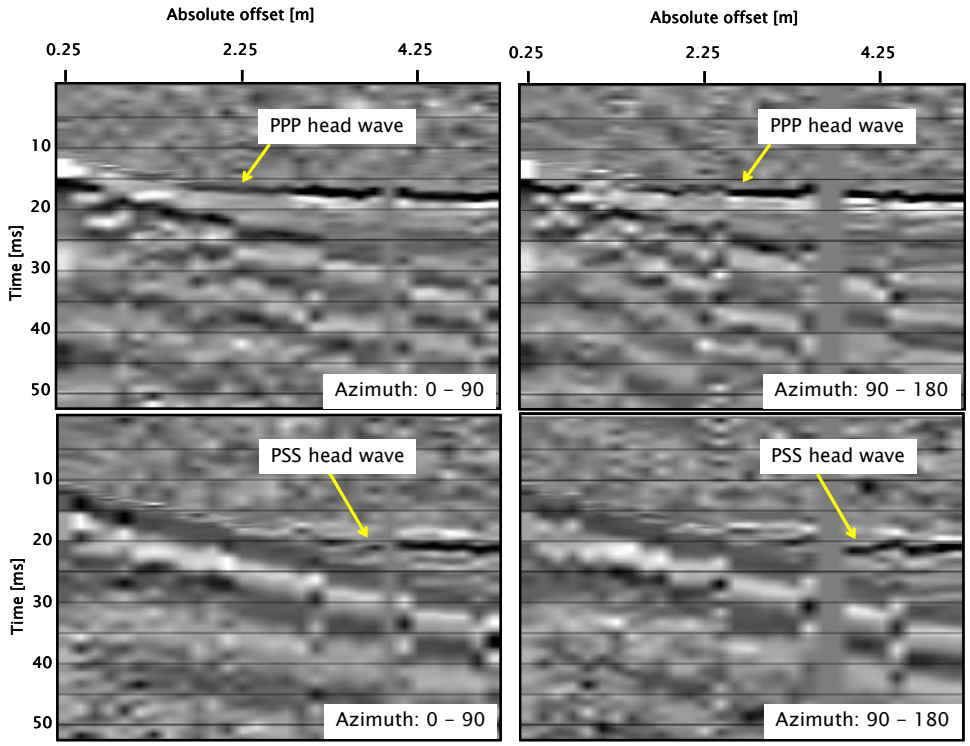

Figure 2.39 Vertical (top) and inline (bottom) component traces from CMP #210. The left panel shows traces with an azimuth range between 0 and 90 degrees, while the right panel is between 90 and 180. No significant difference in arrival time of the PPP head wave is observed in the two different azimuth ranges. Some time variation of the PSS head wave is observed in the inline component.

The inline component traces from the same CMP show some variation, but this variation is unlikely to be caused by anisotropy (Figure 2.39). Many factors that have not been

considered include the station elevation differences, the ground coupling, the horizontal orientation and strength of the impact are very likely to cause time variations on the order of fractions of milliseconds.

The first part of the processing flow is the amplitude and frequency balancing. Starting with the amplitude balance, a trace equalization correction was applied to data sorted by receiver location. This was undertaken since the strength of the source varies for every location (hammer impact). The trace by trace equalization was applied to balance the energy by source variability. The effect is not well appreciated in a display, but makes a difference for further processes applied (Figure 2.40). Both the vertical and radial components were equalized using the same operator.

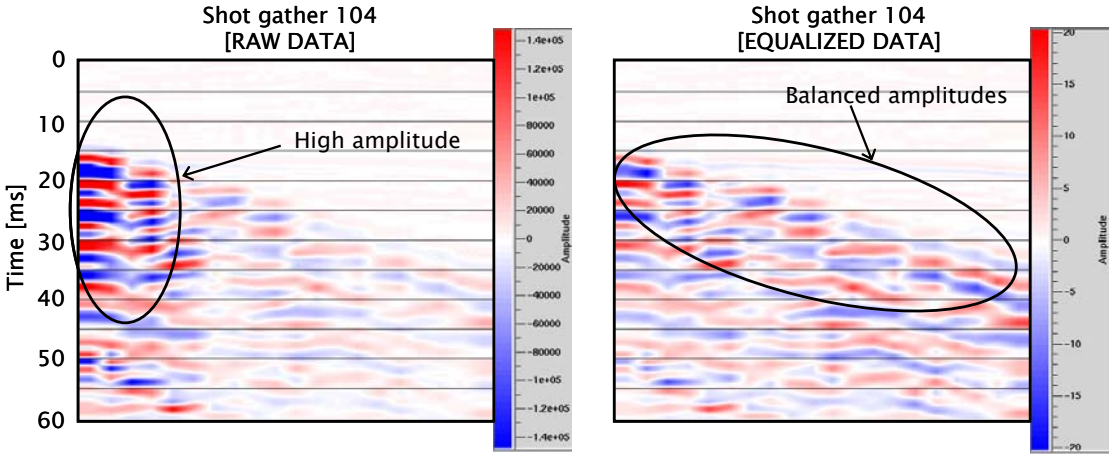

Figure 2.40 Trace equalization applied in the vertical component of shot gather 104. The left diagram shows the raw data with the color bar scale that ranges from 140000 to -140000. Observe how the amplitudes at near offset are very strong compared to the far offset traces. The right diagram shows the same shot gather after trace equalization with the new color bar scale ranging from 20 to -20. Observe how the amplitudes are balanced across all traces.

Now that the amplitudes have been equalized, the frequency spectrum of the data needs to be whitened. The frequency content of the 3D seismic data is different than the 2D

seismic because of the different sources used in each survey, a hammer for the 3D and a pellet gun for the 2D surveys. A time-varying spectral whitening application in ProMAX which works by applying different gains to individual frequency bands was used to balance the seismic data.

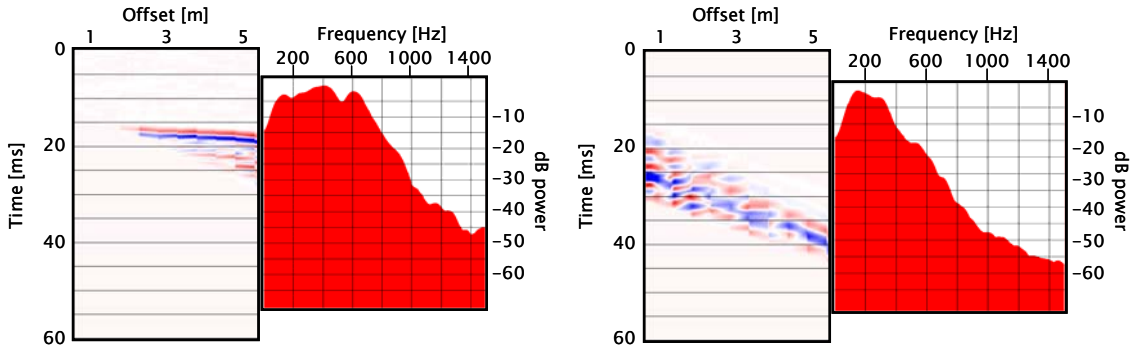

Figure 2.41 Amplitude spectrum of data from vertical component of shot gather 104. The left diagram is the spectrum calculated over a time window containing the head wave, which frequency content ranges from 100 Hz to 650 Hz. The right diagram is the spectrum calculated over the direct arrival, which frequency content ranges from 100 Hz to 300 Hz.

An amplitude spectrum (vertical component) in a time window containing the head wave indicates a broad dominant frequency range from 150 to 650 Hz (Figure 2.41). The parameters for the 3D whitening operator were similar to the 2D, namely, 100 ms operator length, 25% padding, 10 frequency panels and 100-110-810-820 Hz frequency limits. The result from applying this frequency domain operator yields a zero phase wavelet at the head wave arrival and with amplitude similar to the other events (Figure 2.42).

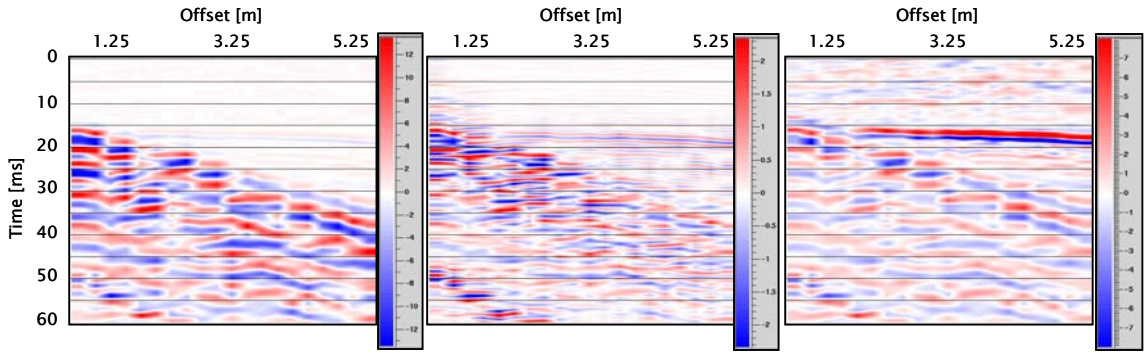

Figure 2.42 Comparison of frequency balance (whitening) versus AGC median for vertical component shot 104. Original (left), frequency balanced (middle) and AGC'ed (right) panels show the different results obtained.

An AGC operator was applied to the raw data as well (Figure 2.42). The scalars for the correction of amplitudes are obtained by calculating a median of all samples in a 20 ms time window. The result from applying this operator to the raw data enhances the head wave arrival, showing a minimum phase wavelet. The difference between the two results rests in the frequency content of the head wave event. The first result has frequencies above -5 dB from 550 Hz to 800 Hz, while the second has a dominant frequency of 150 Hz to 600 Hz. For the purpose of this study frequencies higher than 600 Hz are not considered to be reliable.

The following step is the separation of signal and noise. In this case the direct arrival and lower velocity modes are considered to be *noise*, while the head wave arrival is the *signal* to be separated. Since the radial domain frequency filter was found to be more effective in separating the noise from the signal than a low frequency cut filter, it is used again for the 3D seismic dataset. The discussion can be reviewed in the previous section. A radial fan filter was used to transform the data into the radial domain. The parameters for the transformation were the following:

- 600 radial traces (10 times the maximum number of traces per source location);
- Linear interpolation;
- Minimum radial trace velocity: -20000 m/s;
- Maximum radial traces velocity: 20000 m/s;
- Time coordinate for radial trace origin: 0.01 s; and
- Bandpass filter frequency limits: 80 Hz to 90 Hz and 800 Hz to 810 Hz.

The geometry of this survey makes the offset distribution of source location gathers to be irregular, i.e., consecutive traces with different offset intervals and in some cases with the same offset (Figure 2.43). Trace ensembles output from the radial filter show artifacts (Figure 2.43). This corresponds to traces with similar or equal offset that come into the radial filter. Prior to input traces to the filter a binning of offset values is required to avoid these artifacts. The binning consisted in sorting traces by source location and grouped them in offset bins defined by the following parameters, minimum 0 m, maximum 6 m and interval 0.1 m. Traces within a source location ensemble that had the same offset bin were averaged. After this step the traces were resorted using the new offset distribution and input to the radial filter. The results show a filtered trace ensemble with no smoothing effects of noise (Figure 2.43).

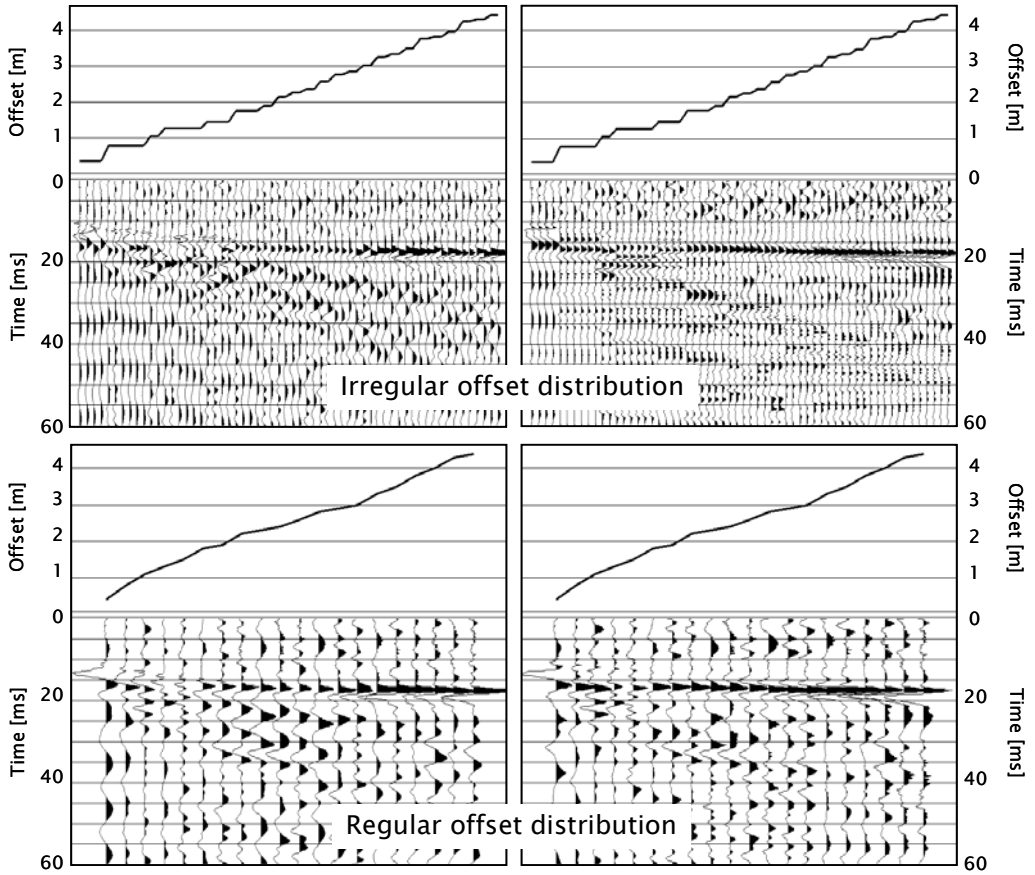

Figure 2.43 Traces from source location 513 sorted by offset. The curve shown on top of each ensemble represents the offset distribution. The left and right ensembles show data before and after radial filter. Observe the artifacts caused by repeated traces in the irregular offset distribution. After offset binning (bottom ensembles) the radial filter is applied without artifacts.

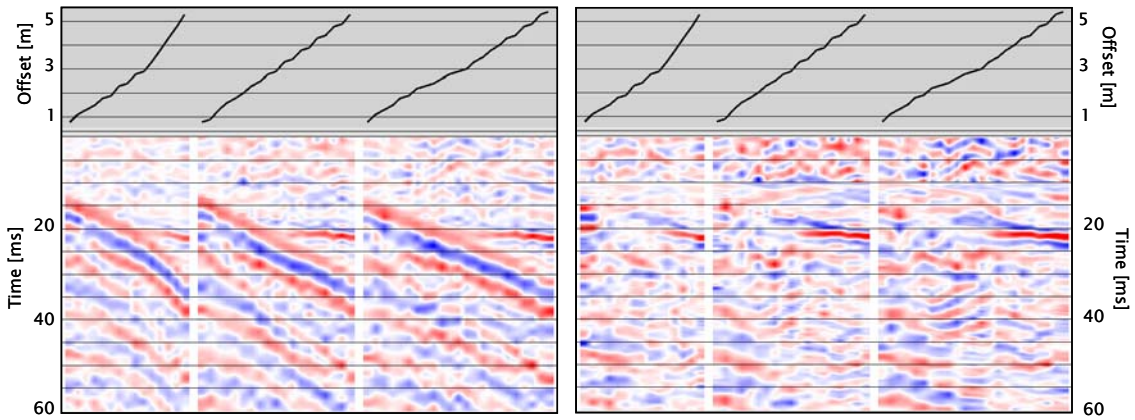

Figure 2.44 Three consecutive source ensembles: 2519, 2520 and 2521. The left diagram is the data before radial filter and the right diagram is after filtering. The ensembles shown have been binned by offset before applying the radial domain frequency filter. The curve shown on top of each ensemble represents the offset distribution. Observe the suppression of direct wave.

The direct wave is strongly apparent on the radial component, compared to the vertical component (Figure 2.44). The use of radial domain frequency filtering for near-surface events is important for the suppression of noise (Figure 2.44). After data has been balanced and filtered, velocity correction and stack follows.

The velocity correction (linear moveout of the head wave arrival) is conducted in the source domain, and the stacked energy is assigned to the trace position falling right under its respective source location. This is repeated for all the source locations and a 3D image with bin size of 25 cm x 50 cm is obtained. The number of bins equals the number of source locations in the survey, which in this case was 325 (25 in the inline direction x 13 in the crossline direction).

The vertical and radial component were sorted by gathers of source location and offset. Since variation of the unfrozen layer structure is observed from the 3D ground-penetrating radar map (Appendix A), 25 gathers from different source locations around the area were used for velocity analysis (Figure 2.45). The traces at each source location were sorted by offset and several linear move-out (LMO) velocity values were applied.

LMO velocity values were obtained selecting the gather with the best corrected event from the gathers with different correction values. The velocity variation observed across the study area responds to dips in the top of the frozen layer. The arrangement of sensors in the field limits the ability of discriminating variation accurately enough since the maximum offset was 5 m. Another disadvantage of this technique is that ensembles (source location gathers) from the centre of the survey lack of long offset traces thus lack of head wave energy.

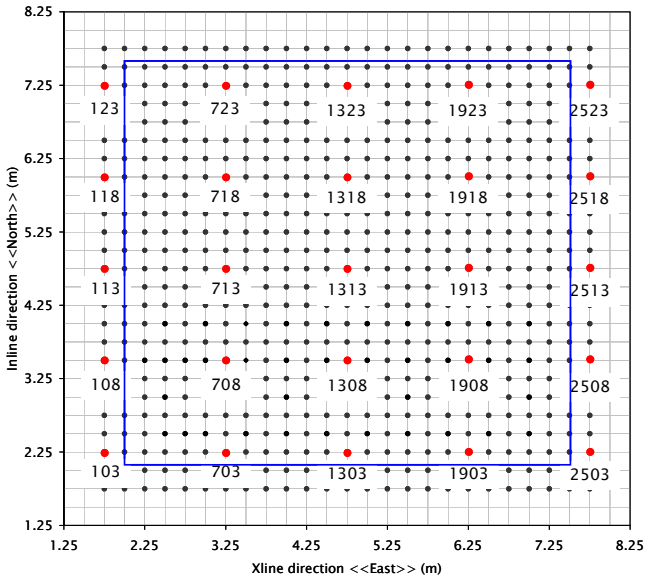

Figure 2.45 Map of 3D seismic survey. Red dots indicate the locations selected for velocity analysis. The blue square delimits the imaged area using the CDP domain method.

The ensembles used for velocity analysis (Figure 2.46 and 2.47) were corrected using the following LMO velocity corrections, 1500, 2000, 2500 and 3000 m/s for the vertical component, and, 1000, 1500, 2000 and 2500 m/s for the radial component data. These velocities were guided using results from the previous 2D seismic imaging. A more refined search was done after the first analysis but no major differences were observed. A single LMO correction velocity of 2500 m/s for P wave and 1500 m/s for S wave, yielding a V_P/V_S ratio across the area of 1.67.

The velocities obtained (Table 2.8) are not interpretable since they cannot be attributed to a common point in the subsurface, but to a rectangular area of the subsurface. The parameter that is related to the structure of the permafrost top is the pseudo zero-offset time since it is a direct function of the depth to the refracting surface below the source location (Equation 2.9).

Source location #	LMO V velocity (m/s)	LMO R velocity (m/s)
103	2500	1500
108	2500	1500
113	2500	1500
118	2500	1500
123	2500	1500
703	2500	1500
708	2500	1500
713	2500	1500
718	2500	1500
723	2500	1500

Source location #	LMO V velocity (m/s)	LMO R velocity (m/s)
1303	2500	1500
1308	2500	1500
1313	2500	1500
1318	2500	1500
1323	2500	1500
1903	2500	1500
1908	2500	1500
1913	2500	1500
1918	2500	1500
1923	2500	1500

Source location #	LMO V velocity (m/s)	LMO R velocity (m/s)
2503	2500	1500
2508	2500	1500
2513	2500	1500
2518	2500	1500
2523	2500	1500

Table 2.7 LMO velocity values obtained for the source domain imaging processing.

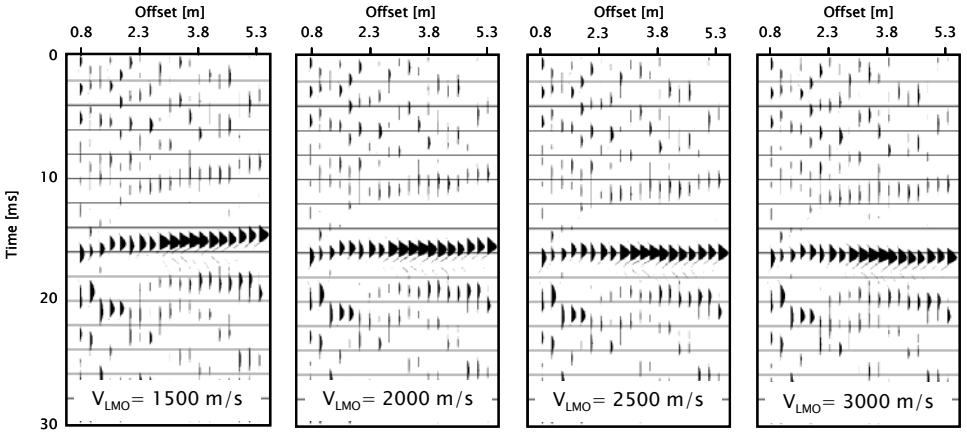

Figure 2.46 Vertical shot gather 118 corrected using different LMO velocities (from left to right): 1500, 2000, 2500 and 3000 m/s. The appropriate correction occurs with a value of 2500 m/s.

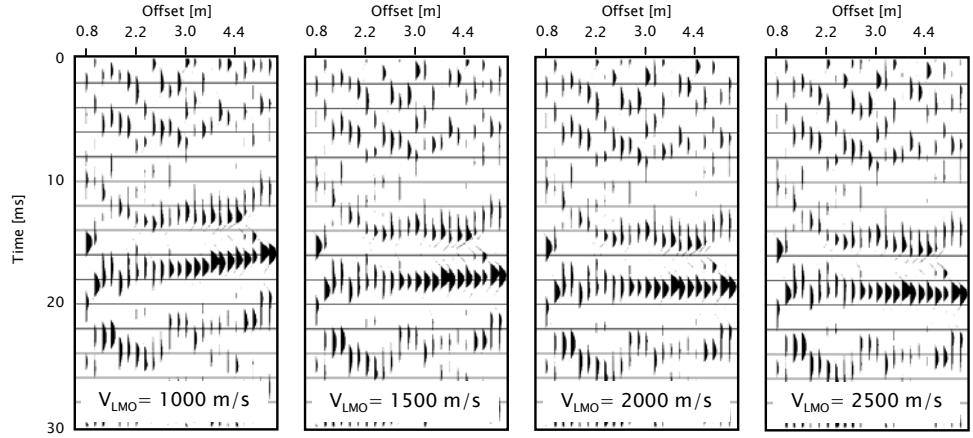

Figure 2.47 Radial shot gather 2513 corrected using different LMO velocities (from left to right): 1000, 1500, 2000 and 2500 m/s. The appropriate correction occurs with a value of 1600 m/s.

A general south to north dip of the frozen layer is interpreted in the stacked sections. The reason being the increasing zero-offset time of the head wave arrival found in the N-S seismic sections.

$$t_i = 2\,Z\cos(\alpha_c) / V_{P1} \qquad (2.9)$$

where Z is the depth to the refracting surface, α_c is the critical incidence angle, V_{P1} is the compressional wave velocity in the first medium (thawed layer), and t_i is the zero-offset time or commonly known as intercept time. After all the traces for one ensemble have been LMO corrected, they are stacked to form a zero – offset trace assigned to the specific source location for that ensemble. The dip of the structure, which can be interpreted, the thickening of the thawed layer, is observed well in the crossline stacked seismic section number 1 (Figures 2.48 and 2.49).

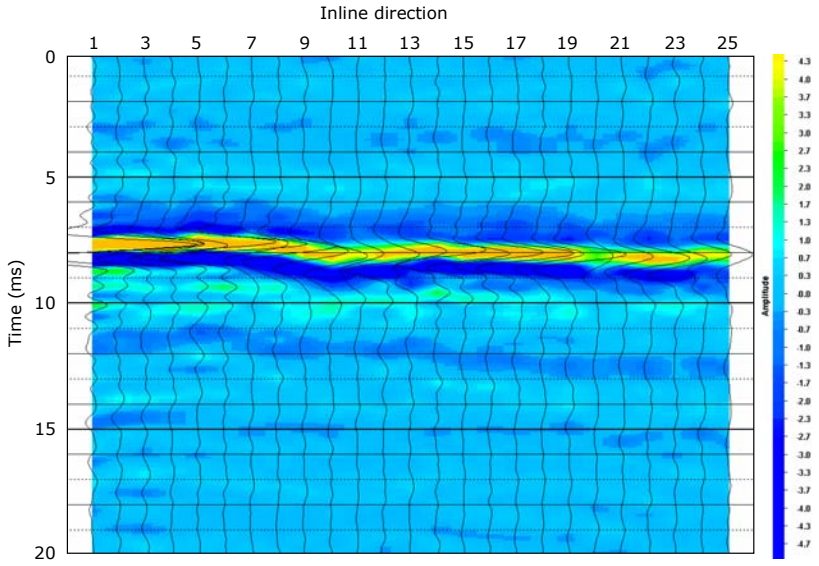

Figure 2.48 Crossline seismic section number 1, from vertical component data.

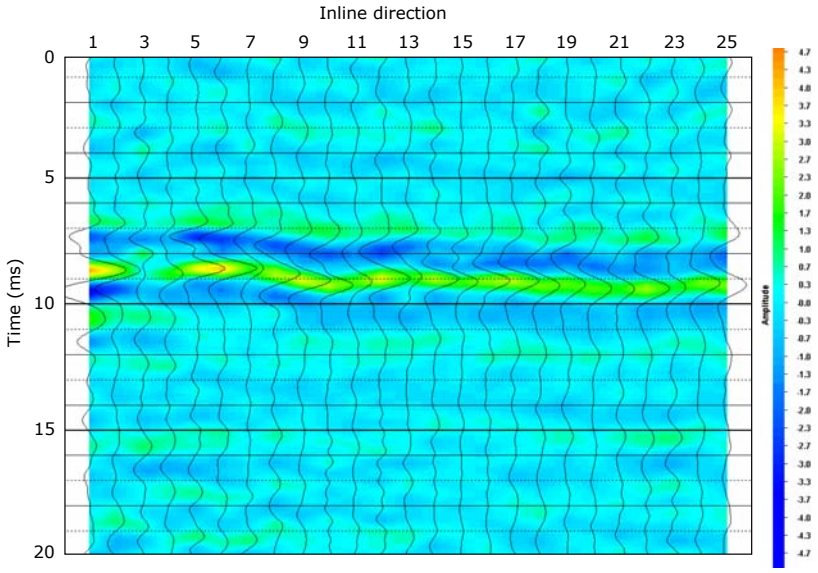

Figure 2.49 Crossline seismic section number 1, from radial component data.

It is possible to generate a 3D seismic image of the shallow subsurface using the refracted wave. After all the ensembles have been stacked a volume is obtained. Due to acquisition geometry, the number of traces in the N-S direction (inline direction) is different than the ones in the E-S direction (crossline direction), 13 and 25 respectively (Figure 2.25). The total number of traces for the radial and the vertical component is 325 for each volume. Linear interpolation in the inline direction was applied to have a symmetrical bin size in both directions. The results indicate a *signal* with stronger amplitude in the vertical component compared to the radial (Figures 2.48 and 2.49).

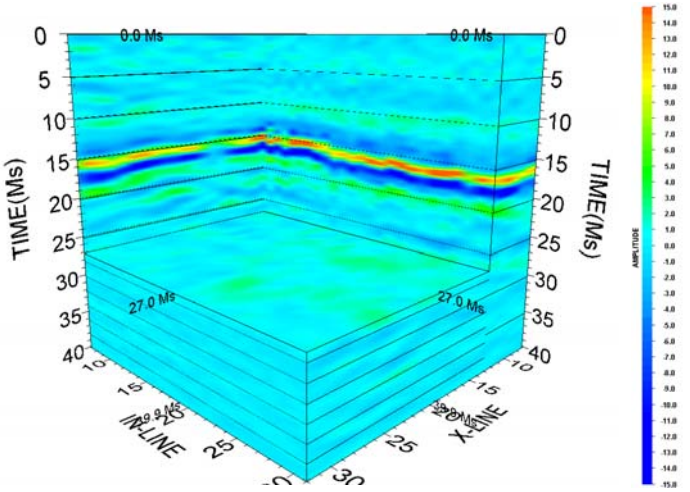

Figure 2.50 View of seismic volume from vertical component data.

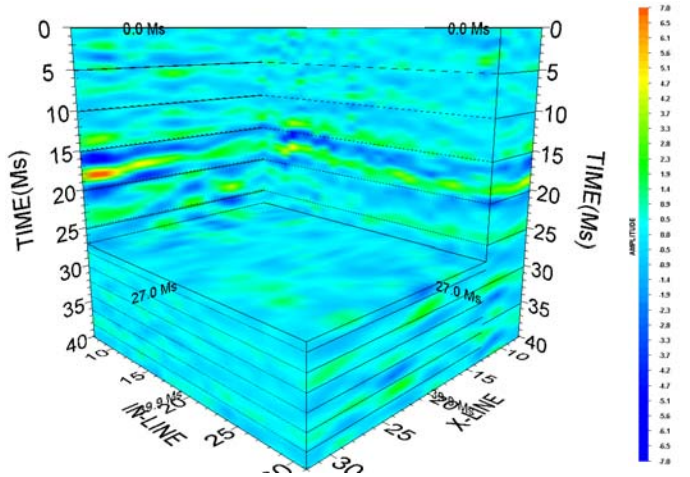

Figure 2.51 View of seismic volume from radial component data.

CHAPTER THREE: *GROUND-PENETRATING RADAR EXPLORATION AT DEVON ISLAND, NUNAVUT*

A number of ground-penetrating radar, GPR, experiments were acquired at the HMP base camp. These experiments were used to image the frozen-unfrozen sediment interface (Figure 3.1), as well as to obtain soil properties. Velocity analyses using variable-offset, constant-offset geometries, 2D and 2.5D surveys were part of the experiments. GPR method was chosen because radar waves are sensitive to the contrast in dielectric properties of the soil. Moorman *et al.* (2000) review the basic concepts in GPR data interpretation. They show that the reflection coefficient (for a planar surface) can be related to the dielectric properties of the material by equation 3.1:

$$R = \frac{\sqrt{k_1} - \sqrt{k_2}}{\sqrt{k_1} + \sqrt{k_2}} \qquad (3.1)$$

The constants k_i (i=1 for upper layer and i=2 for lower layer) represents the dielectric constant of the material and are measured in electrostatic units (esu). For unfrozen sediments the average k is 25 esu, while for frozen sediments is 6 esu. The reflection coefficient for this case scenario is 0.34. This value is very high compared to the frozen sediment (k=6 esu) over rock (k=8 esu) case which has a reflection coefficient of -0.07. This is the reason why GPR exploration is ideal for subsurface imaging under periglacial conditions.

The depth of the active layer varies according to the combination of several factors, such as, ambient air temperature, degree and orientation of slope, vegetation, drainage, snow cover, soil and/or rock type, and water content (French, 1996).

The freezing is a more complex process than thawing because it occurs from both sides of the active layer while thawing occurs only from the top. Additionally, a drop in

temperature occurs in the freezing process as a consequence of the retarding freezing effect caused by the release of latent heat.

The seasonally active permafrost is defined as the uppermost part of the permafrost that thaws and refreezes seasonally. The extent of this layer depends either of the salinity and/or clay content. Frost heave and ground ice segregation are two phenomena which represent engineering hazards due to the displacements and pressures generated (French, 1996).

An interesting feature related to permafrost areas is “patterned ground”. Polygonal patterns are one of the most important. Circles, stripes, nets and steps also may be formed depending on the slope angle. The processes responsible for these patterns occur within the active layer, and have not been proven, although numerous hypotheses exist. The term cryoturbation, referred to all soil movements due to frost action, is often used to explain the development of patterns. Usually three types of cracking control the formation of polygonal patterns: desiccation, thermal contraction and seasonal frost. Details with regards to the nature of each of these processes are discussed in French (1996).

Two different instruments were used to record these experiments, both from Sensors and Software Systems: (1) a constant – offset antennas NOGGIN 250 MHz GPR cart, and (2) a variable – offset PulseEKKO unit with 100 and 200 MHz antennas. The separation of the antennas in the NOGGIN equipment is 0.28 m. An important characteristic of this equipment is that it allows a real-time display of the data as it is been acquired. A review of the acquisition and parameters of the experiments was reported earlier by Nieto *et al.* (2003).

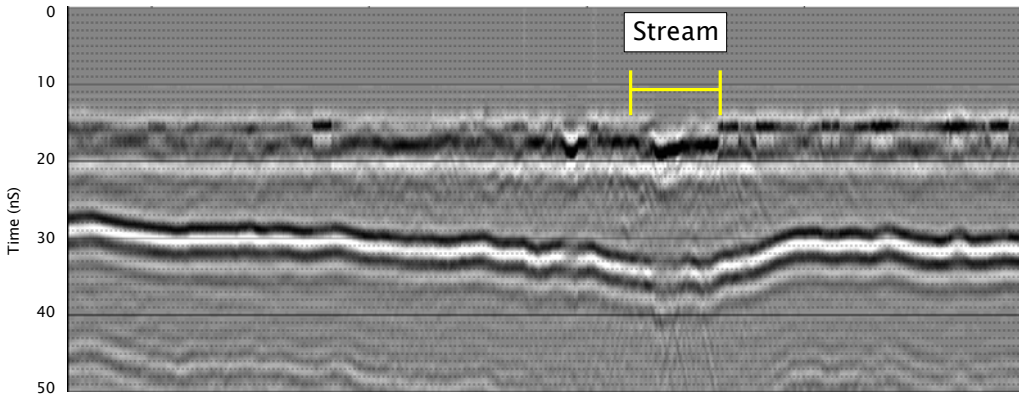

Figure 3.1 Ground – penetrating radar 2D recorded across a stream in the Conrad Valley. The length of this section is 130 m. The thickness of the active layer is greater under the river mainly due to water's greater heat capacity, among other factors.

The location for the 2D and 2.5D ground-penetrating radar experiments was a flat area located between the greenhouse and the work tent inside the base camp (Figure 3.2). The recorded experiments were:

(1) Reconnaissance 2D survey (250 MHz antennas);

(2) Constant-offset velocity analysis with 250 MHz antennas (Rebar experiment); and

(3) 2.5D survey (constant-offset unit with 250 MHz antennas).

The analysis of this data allowed a detailed description of GPR imaging of soil under periglacial conditions.

3.1- *2D GPR survey and test pit*

A 26 m GPR line acquired at the study area with the NOGGIN 250 MHz unit indicates the presence of a complex strong reflection from 17 to 25 ns (Figure 3.3). This event was interpreted to be the frozen-unfrozen sediments interface, and it was confirmed with the results obtained from a test pit dug next to the line (Figure 3.4). This interface shows

discontinuities and diffractions which could be caused by either the presence of boulders, or by formation of ice lenses at the top of the permafrost (French, 1996).

Figure 3.2 Views of the study areas of the project: (1) base camp zone to the left, and (2) land strip zone to the right.

The distribution of sediments in the active layer varies from a very fine silt layer on the top to a rocky pebbly layer right on top of the permafrost (Figure 3.4). It is reasonable to think this process to be controlled by the freezing-thawing cycles in this area. French (1996) defines the active layer as the layer of ground in areas underlain by permafrost which are subject to annual freezing and thawing.

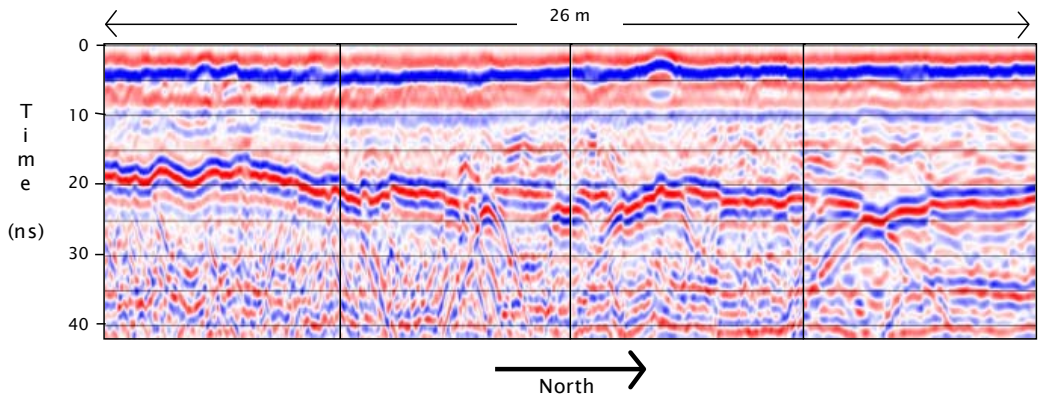

Figure 3.3 A 26 m GPR reconnaissance line from the base camp site. A series of diffractions are interpreted as either boulders or ice lenses in the top of the permafrost.

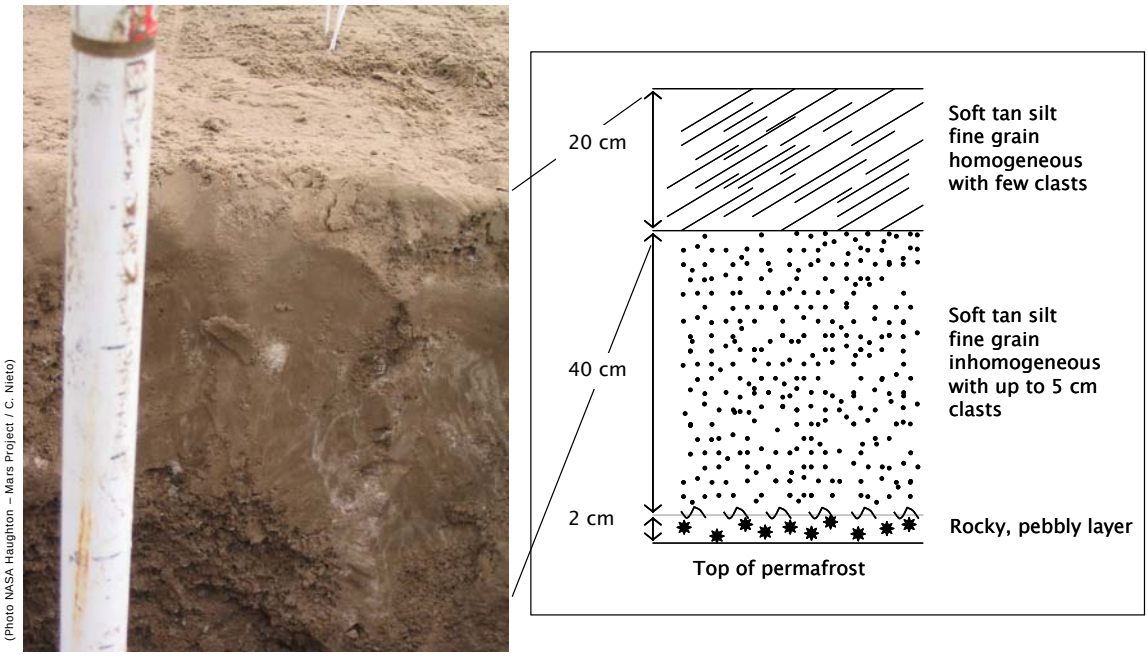

Figure 3.4 View of the test pit dug in the base camp zone. The active layer may be separated into three layers according to sediments size.

3.2- *GPR velocity analysis*

A number of surveys were recorded to obtain velocity curves for the active layer, seasonally active permafrost, and permafrost (Figure 3.4). Velocity curves are important for time-to-depth conversion, and interpretation of GPR data. The experiment was recorded with the NOGGIN 250 MHz. This unit has a constant separation of 0.28 m between the receiver and transmitter antennas.

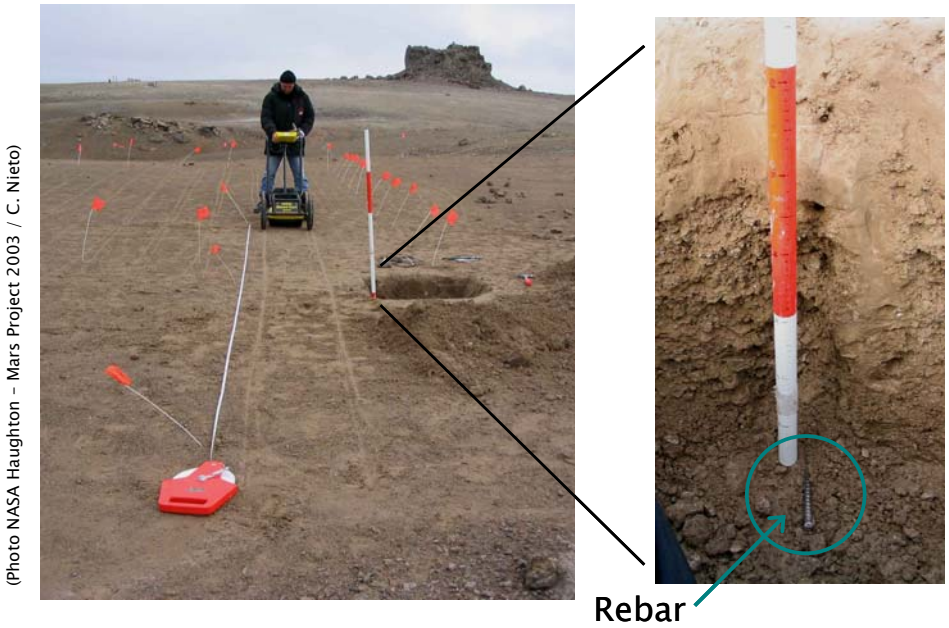

Figure 3.5 Views of the constant offset GPR velocity survey. Rebar was pound at various depths (right) and a GPR line was acquired (left).

The experiment consisted of recording constant offset six meters GPR lines across a Figure with a one meter rebar at various depths (Figure 3.5). This element was used since it has a strong radar response, which is used to complete the calibration. Nieto *et al.* (2003) give a more detailed explanation of the experiment.

A pit was dug to the bottom of the active layer. In one of its sides rebar was driven to the soil at various depths (Figure 3.5). For each depth value a GPR line was recorded. A rebar diffraction event was interpreted for each line (Figure 3.6), obtaining a set of time-depth values (Table 3.1). A cross plot of time and depth values yield an average velocity model of the active layer (Figure 3.7). Interval velocities are obtained from each time-depth pair, and RMS velocities (Figure 3.8) are calculated as well using equation 3.2:

$$V_{RMS} = \sqrt{\frac{\sum V_{INT}^2 \cdot \Delta t}{\sum \Delta t}} \qquad (3.2)$$

Rebar depth (m)	Rebar twt (ns)	Interval velocity (m/ns)	RMS velocity (m/ns)	Diffraction velocity (m/ns)	Difference (%)
0.00	2.98	0.0577	0.0577	0.0430	25.48
0.10	5.95	0.0672	0.0626	0.0565	9.78
0.20	7.54	0.1260	0.0802	0.0575	28.33
0.30	10.32	0.0720	0.0781	0.0630	19.32
0.40	13.50	0.0630	0.0748	0.0640	14.35
0.50	16.67	0.0630	0.0727	0.0705	3.03
0.62	20.24	0.0672	0.0718	0.0740	3.15

Table 3.1 Time-depth values for constant offset GPR line. Rebar times are referenced to the air-ground wave arrival.

The slight change observed in the slope of the time-depth crossplot indicates a change in the radar velocity, which is also observed in the interval and RMS velocity models, as expected (Figures 3.9 and 3.10). This change occurs at the same depth value where the sediments distribution changes in the test pit (Figure 3.4). Based on reported radar velocities (Table 3.2) the conclusion of this velocity change responds to the contrast between saturated silt and saturated sand.

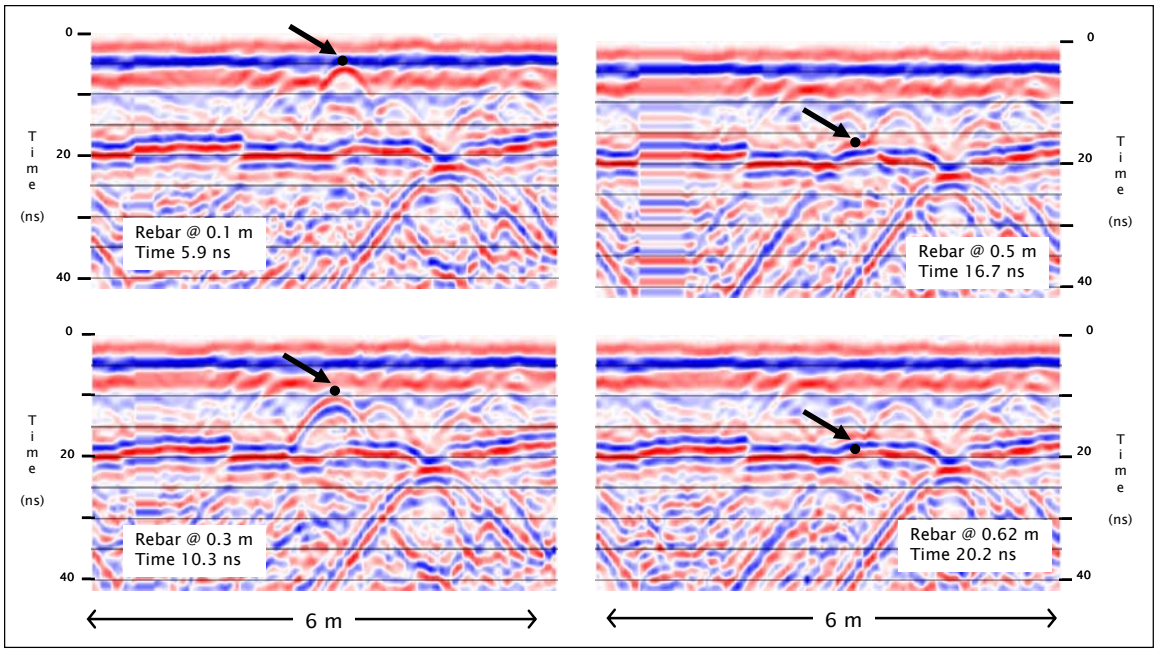

Figure 3.6 GPR lines from constant offset velocity survey. Results from rebar at 0.1, 0.3, 0.5 and 0.62 m are displayed from top to bottom, left to right. Black arrows indicate rebar diffraction apex.

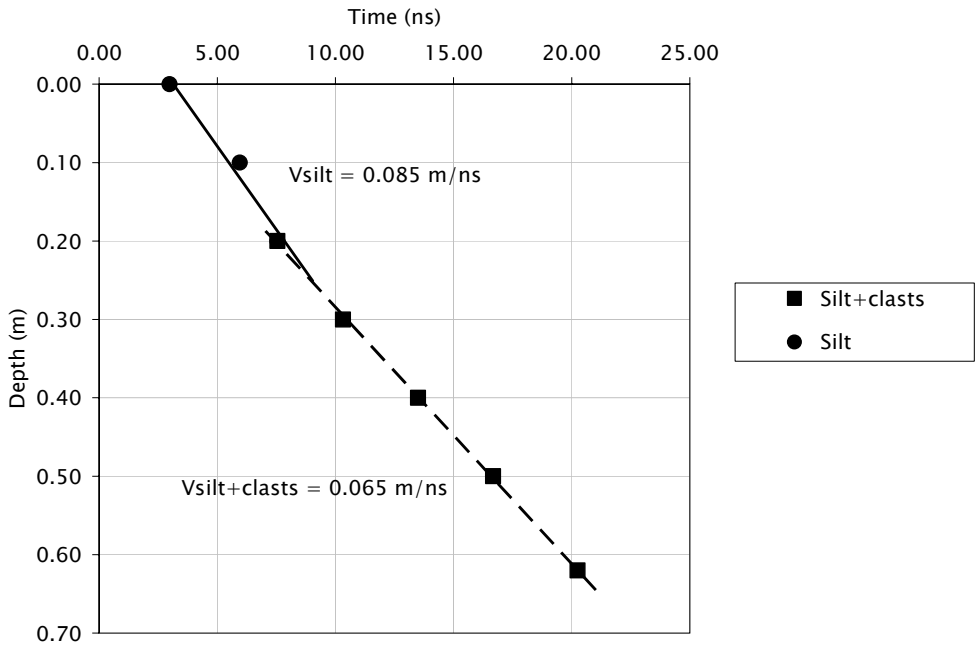

Figure 3.7 Time-depth crossplot. An average radar velocity model by linear regression. Notice the change of the slope around 0.2 m depth.

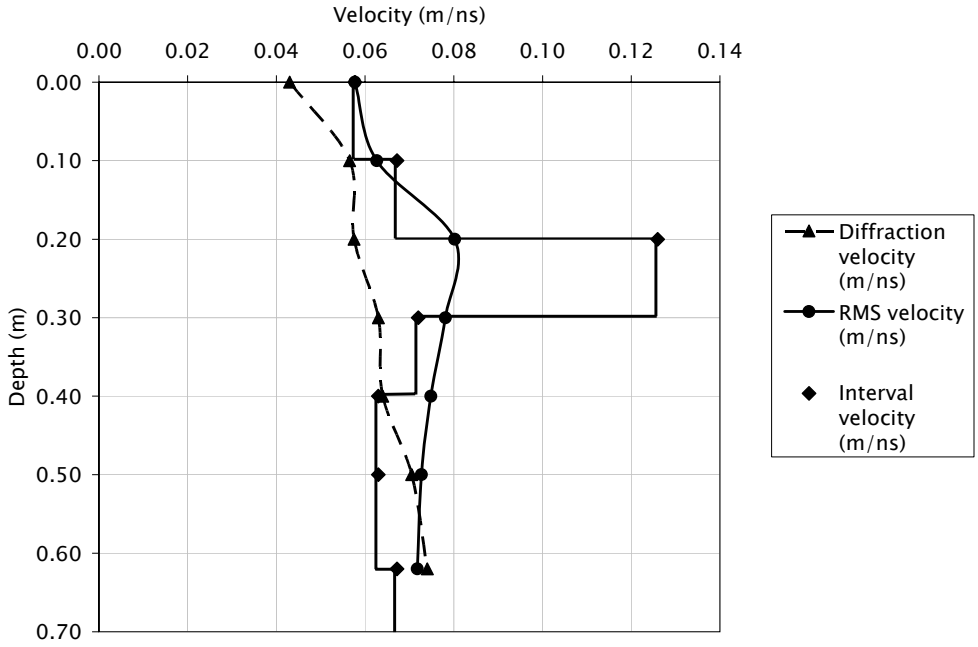

Figure 3.8 Various radar velocity models. Interval and RMS velocity curves calculated from the time-depth pairs indicate a change at 0.20 m depth.

Material	Radar velocity (m/ns)
Air	0.300
Fresh water	0.033
Limestone	0.120
Saturated sand	**0.060**
Saturated silt	**0.090**
Dry silt	0.070

Table 3.2 Radar velocity values for different materials (Davis *et al.* 1989; Moorman *et al.* 2000).

An additional velocity model was obtained by fitting *hyperbolas* to the rebar diffractions at different depth values (Figure 3.8). It is assumed that the moveout of a scatter point recorded with a constant receiver-transmitter survey is hyperbolic, which is a fair approximation for this case. Only a narrow offset of the scattered energy is used to the

fitting process as the diffraction is not observed well in the long offset values (Figure 3.6).

The velocity model obtained by fitting hyperbolas to the rebar diffractions grossly correlates with the RMS velocity curve (Figure 3.8) but with some differences. The errors range from 3% to 28% (Table 3.2), decreasing with depth. A number of reasons can be used to explain this difference, starting from the fact that the moveout of a scatter point diffraction recorded using a constant receiver-transmitter separation is governed by the double square root equation (Figure 3.9; Equation 3.3; Bancroft, 2001):

$$T(x) = \sqrt{\left(\frac{t_o}{2}\right)^2 + \left(\frac{x-h}{V}\right)^2} + \sqrt{\left(\frac{t_o}{2}\right)^2 + \left(\frac{x+h}{V}\right)^2} \qquad (3.3)$$

where t_o is the vertical two-way time from a scatter point, x is the horizontal distance from the scatter point to the CMP, h is the half offset, and V is the RMS velocity.

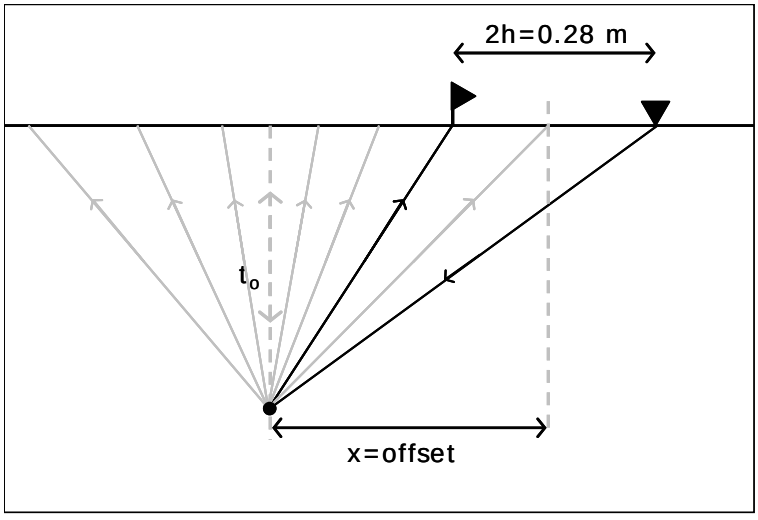

Figure 3.9 Diagram calculation of travel time from a scatter point in a constant velocity media with a constant receiver-transmitter array. Notice that only one receiver records the diffracted event. The gray lines are the scattered energy.

Consider the rebar located at two different depths below the surface: 0.2 and 0.62 m, in a media with a constant radar RMS velocity of 0.08 m/ns (Figure 3.7). A synthetic line recorded using two different settings show the contrast in arrival times and moveout of the scattered energy (Figure 3.9). A constant receiver-transmitter offset and CMP variable offsets surveys were used to calculate travel times from the model defined previously (Figure 3.10). From the synthetic example the diffractions in the variable offset geometry pass through the scatter point for both cases, as expected from the standard normal moveout equation (Equation 3.4).

$$T(x) = \sqrt{(t_o)^2 + \left(\frac{X}{V}\right)^2} \qquad (3.4)$$

and $X = 2 \cdot x$

where t_o is the vertical two-way time from a scatter point, X is the receiver transmitter offset and V is the RMS velocity.

On the contrary, the diffractions pass below the scatter point for both cases using the constant receiver-transmitter offset geometry. The estimated velocity from a constant receiver-transmitter offset geometry is different than the velocity obtained from a variable offset geometry. Additionally, different apex times occur at zero offset, but are not an issue for the aperture and depths used in this experiment. For a correct estimation of velocities using the hyperbolae fitting process, the double square root equation needs to be considered.

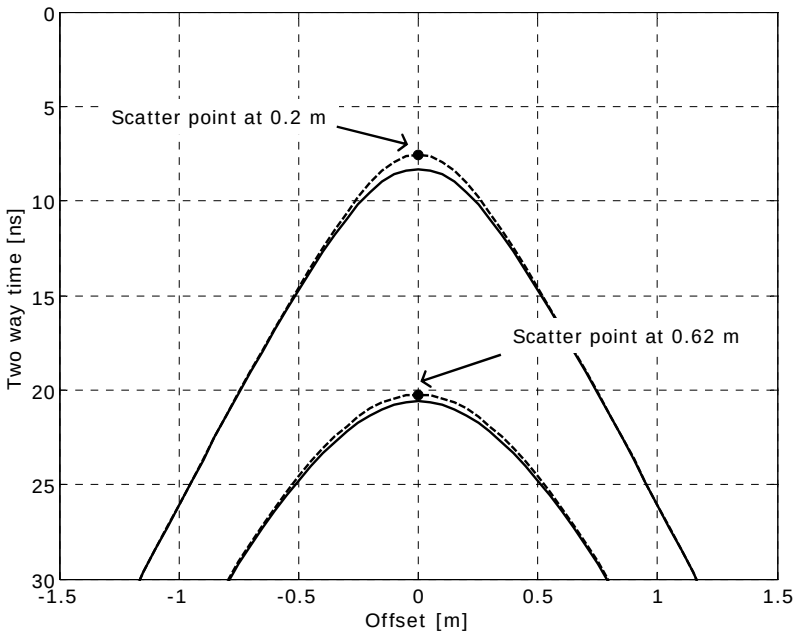

Figure 3.10 Synthetic travel times of a scatter point at two different depth values using a CMP variable offset geometry (dashed lines) and constant receiver-transmitter separation (solid lines).

3.3- *2.5D GPR survey*

An area of 10 m^2 was surveyed using the constant offset NOGGIN 250 MHz GPR unit. Nieto *et al.* (2003) describes the field design and recording of this dataset, as well as processing. The volume consists of 21 north-south lines x 21 east-west lines (Figure 3.11). The spatial sample rate set for the inline direction is 0.05 m, and the separation of the lines was 0.5 m. The time sample rate was set to 0.4 ns.

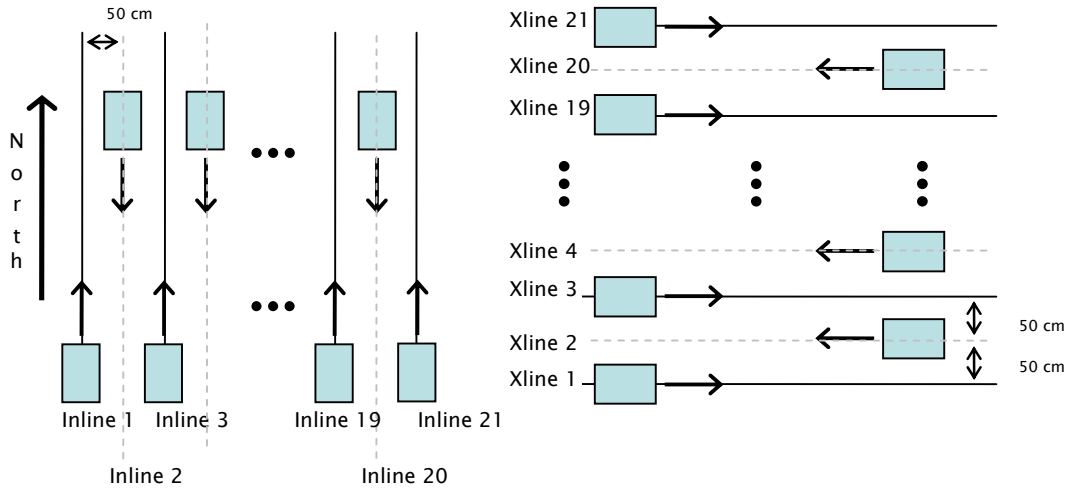

Figure 3.11 Diagram of the acquisition parameters for the 2.5D. GPR inline and xlines correspond to north-south and east-west, respectively. The blue rectangles represent the GPR unit and the arrows are the direction of recording.

An advantage of using constant offset lines is that the processing steps are minimal, consisting of only: trace DC removal, automatic gain control and high cut frequency filter. On the other hand, it constrains the ability of using all the analysis tools from the prestack world, such as: analysis of signal variation with offset (AVO), measurement of propagation velocities of direct, refracted or reflected modes, among other techniques.

Defining a volume from a series of 2D surveys in orthogonal directions is a novel and quick use of constant offset GPR units, but it causes misties among intersecting lines. Additionally, it lacks the ability of correct migration of out-of-plane reflections (Yilmaz, 2001), causing discontinuity of data from line to line. An additional issue with this technique is directly associated with the measuring device attached to the NOGGIN unit. Depending on the conditions of the surface, the unit might jump causing distances to be variable from one line to the other. Even small measuring errors can cause problems with the interpolation results due to the scale of detail for this project.

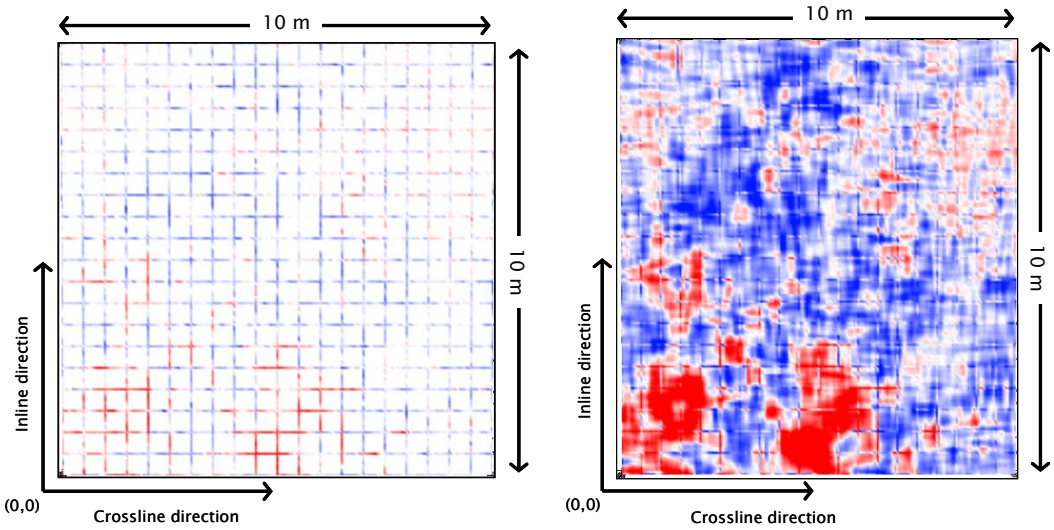

Figure 3.12 Time slice from the 2.5D GPR survey, before and after interpolation+averaging, left and right panels respectively. The spacing between lines is 0.5 m. The gaps are filled by interpolation in each direction. Increasing inline coordinates points toward the north.

Further processes, such as interpolation are required to fill in the gaps produced by the difference between the trace spacing in the inline and crossline directions. A time slice from the volume shows data gaps caused by this problem (Figure 3.12). Two passes of linear interpolation, first in the crossline and second in the inline direction were chosen to fill these zones (Figure 3.13 and 3.14). The final image was obtained by taking the average of both interpolation results. An acquisition footprint marked by the recorded lines is observed in the data after the interpolation+average steps (Figure 3.12).

Out-of-plane reflections problem associated with volumes defined from 2D surveys can be directly observed in the poor correlation at crossing points of orthogonal recorded lines. This causes discontinuity of data from the *recorded lines* to the *interpolated lines* (Figure 3.13). A *recorded line* refers to the line where real data was recorded with the NOGGIN 250 MHz unit. An *interpolated line* refers to the result from interpolating

consecutive traces from the orthogonal recorded lines (Figure 3.13). This is the reason why an acquisition footprint is observed in the final interpolated image (Figure 3.12).

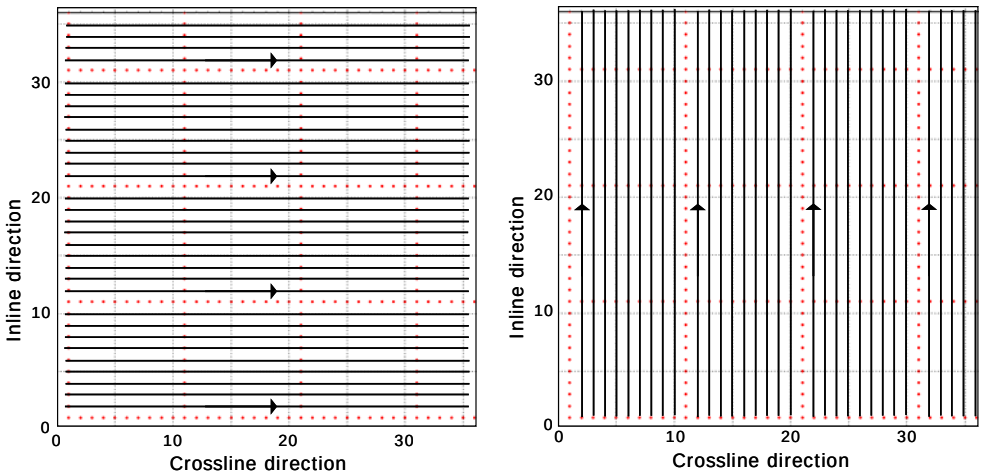

Figure 3.13 Left and right panels shows the grids used for the crossline and inline interpolations, respectively. Red dots indicate a location where a trace was recorded. Black continuous lines indicate the lines which were interpolated. Recorded lines are marked with dotted red lines.

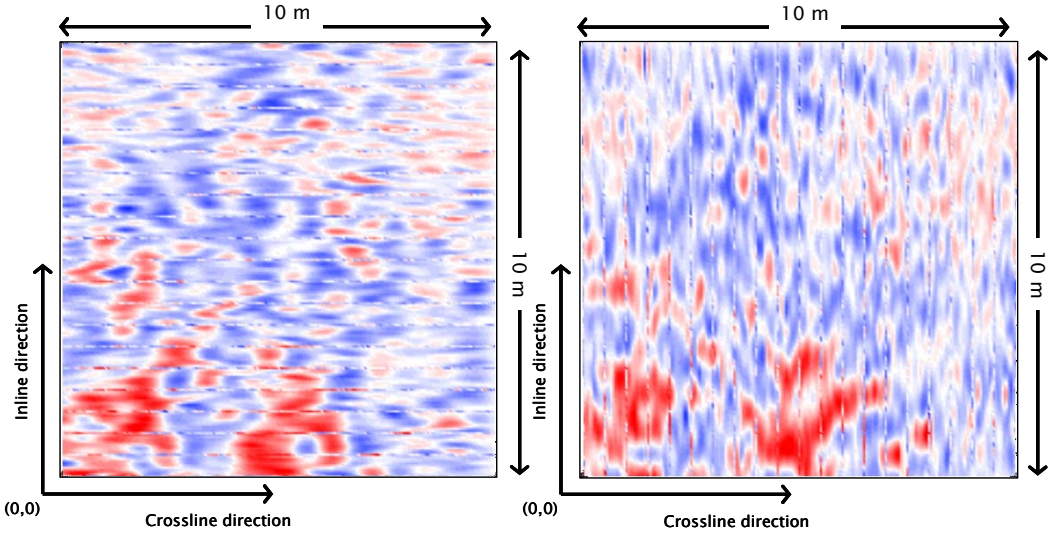

Figure 3.14 Left and right panels correspond to crossline and inline interpolated time slices, respectively. An amplitude stretching effect in the direction of interpolation occurs in both cases as a consequence of the process.

In general, a variety of analysis can be made out of 2.5D data sets. A common application of 2.5D seismic data is to interpret the reflection surfaces and use them to unravel the geological formation history of it.

CHAPTER FOUR: *MACKENZIE DELTA MULTICOMPONENT SEISMIC INTERPRETATION*

Interest in this part of the Arctic has been increasing after a twenty year hiatus since the discovery of the three giant gas fields: Taglu, Parsons Lake and Niglintgak in 1971, 1972 and 1973 respectively. The possibility of the construction of the Mackenzie Valley Pipeline is the factor that has attracted many companies to explore this part of the Canadian Arctic, again (Polczer, 2001; Ross, 2003; Nieto *et al.*, 2003).

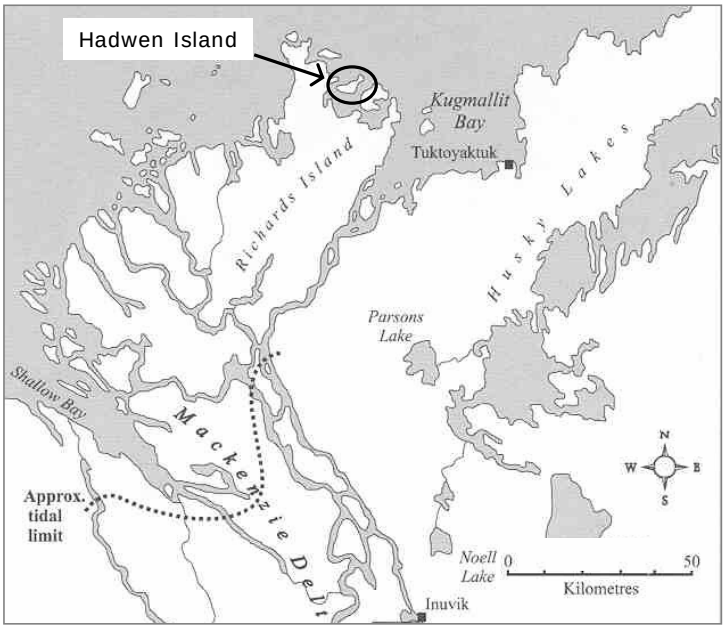

Figure 4.1 Map of the Mackenzie Delta, N.W.T. The location for the seismic test lines was the Hadwen Island north of Richard Island (modified from www.collections.ic.gc.ca)

Devon Energy Ltd. (formerly Anderson Exploration Ltd.) acquired a series of seismic lines in a transition zone, from shore to land, in the Mackenzie Delta, N.W.T. (Figure 4.1). CREWES participated in this project by recording a 3-C seismic line on the same area. This project's main objective was to analyze the performance of different types of

sources and receivers. Motivation for this study was the need for better quality data in transition zones, since many seismic surveys cover areas that comprise deep water bottom, shallow water bottom and land.

4.1- *Subsurface geology review*

A large number of geological surveys, seismic datasets and well logs from the Mackenzie Delta have been reviewed and summarized by Dixon *et al.* (2001). I reviewed isopach maps, structural maps, seismic sections and well logs to define a theoretical geological model of the Hansen Harbour area. Several other authors have worked in the area, but Mi *et al.* (1999) give an interpretation of the Mallik 2L-38 well, which is very useful due to the presence of both P and S wave sonic logs. These are used to define a V_P/V_S function which gives a first approach to the correlation of PS and PP seismic sections.

Mackenzie Delta geology

The Beaufort-Mackenzie basin formed on a post-rift continental margin. The rifting episode began in the Jurassic and continued to the end of the lower Cretaceous. From then until the late Tertiary, compressional tectonics was predominant. Listric faults, folds, and thrust faults are present at various locations in the basin. The combination of significant sedimentation and these structures has resulted in numerous possible traps for hydrocarbons (Dixon *et al.*, 2001).

Consisting mostly of clastic rocks deposited in deltaic, shelf, slope and deep-water environments, the Upper Cretaceous to Holocene sediments in the Beaufort Mackenzie Delta are represented by 12 to 16 km of strata (Dixon *et al.*, 1992). In the area of the

Beaufort-Mackenzie Delta eleven regional sequences have been identified, from the Upper Cretaceous to the Holocene (Figure 4.2). The structural basement is composed of Albian and older strata. These sequences are (from older to younger):

1) Boundary Creek (Upper Cretaceous);

2) Smoking Hills (Upper Cretaceous);

3) Fish River (Early Paleocene to Santonian or Campanian);

4) Aklak (Late Paleocene to Early Eocene);

5) Taglu (Early to Middle Eocene);

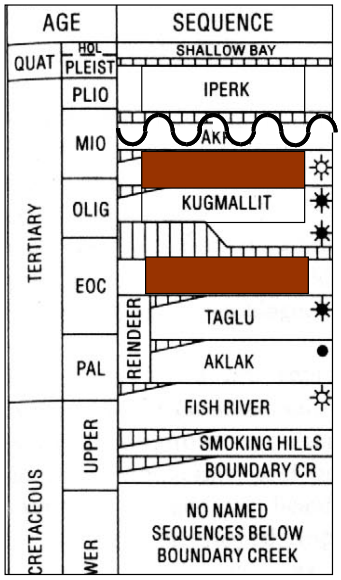

Figure 4.2 Stratigraphic column of the Mackenzie – Beaufort basin (Dixon *et al.*, 1992). Observe that the Kugmallit Sequence has both oil and gas reservoirs.

6) Richards (Middle Eocene to Late Eocene);

Only present as a thin delta complex in the Beaufort-Mackenzie Basin. Under the Mackenzie Delta and near-shore areas the sequence is 1000 to 2000 m thick. Under most of Mackenzie Delta, the Richards Sequence consists mostly of low-velocity shales. They

are of variable thickness and the interval is easily identified on sonic logs. The depositional environment consists of pro delta deposits, mostly shale. The upper boundary is conformable with overlying strata in the Mackenzie Delta. The lower boundary is conformable as well, with the exception of a few erosional unconformities. In seismic sections they consist of either a generally reflection-free interval or one in which there are only weak, discontinuous reflections.

7) Kugmallit (Oligocene)

This sequence has been identified only in the Beaufort-Mackenzie basin. *The thickness estimated in the G-07 well is 1800 m*. The Kugmallit Sequence consists of conglomerates and gravels underlying the Mackenzie Delta and represent *delta plain deposits*. The lower boundary is abrupt throughout most of the basin but varies from apparently conformable (basin ward) to an angular unconformity. The upper contact is also abrupt, but only erosional in the central shelf area. Mackenzie Bay Sequence overlies Kugmallit strata throughout most of the basin. It is possible that the basin margins and some distal basin positions, the younger Iperk Sequence may rest erosional on Kugmallit beds.

8) Mackenzie Bay (Miocene, Late to Middle Miocene)

Deposits of this sequence consist mostly of shale in the central Beaufort area. The dominant environment in the Hansen Harbour area is *delta plain to delta front*, although to the north changes to slope and deep water environments. There is a marked lithological contrast between Mackenzie Bay shale and Kugmallit sandstones. The outer shelf and slope portions of the Mackenzie Bay Sequence are characterized by high-amplitude reflections and well-developed clinoforms, and are good examples of high-amplitude

seismic facies developed in shale-dominant shelf sediments. Under the G-07 well, the thickness of this sequence ranges *from tens of meters up to 300 m*.

9) Akpak (Miocene, probably Late Miocene)

This sequence is not present in the Hansen Island area, since the isopach map indicates that it wedges to a zero edge landward.

10) Iperk (Pliocene to Pleistocene)

The Iperk Sequence thickens from zero on the landward side of the basins to over 4000 m in the north Beaufort Sea. At Hansen Harbour in the G-07 well the interval is approximately *800 meters thick*. It consists of weakly consolidated to unconsolidated sandstone and conglomerate at the basin margins, grading laterally into a succession with more shale basinwards. The Iperk Sequence was deposited as one, very large delta complex centred over the eastern Beaufort Sea. The landward part of the sequence contains fluvial conglomerates and sandstones, grading laterally into deltaic and shelf sandstone and shale that in turn grade into overlying slope shale. The sequence has a *fluvio-deltaic dominant environment* in the Hansen area. It is commonly difficult to separate the Iperk from the Shallow Bay strata. The base is marked by a major erosional unconformity that can be traced throughout the Beaufort-Mackenzie and Banks Beaufort basins. The Iperk strata thin rapidly landward to a zero edge.

11) Shallow Bay (Cenomanian to Holocene)

This sequence is characterized by low-amplitude, discontinuous, subparallel reflections, but only in the Mackenzie Trough. Elsewhere it is difficult to separate from the underlying Iperk Sequence. Some other internal units could be defined using shallow,

high-resolutions seismic data. The Shallow Bay Sequence consists of ocean-ward prograding sequences, many of which are dominated by large delta complexes.

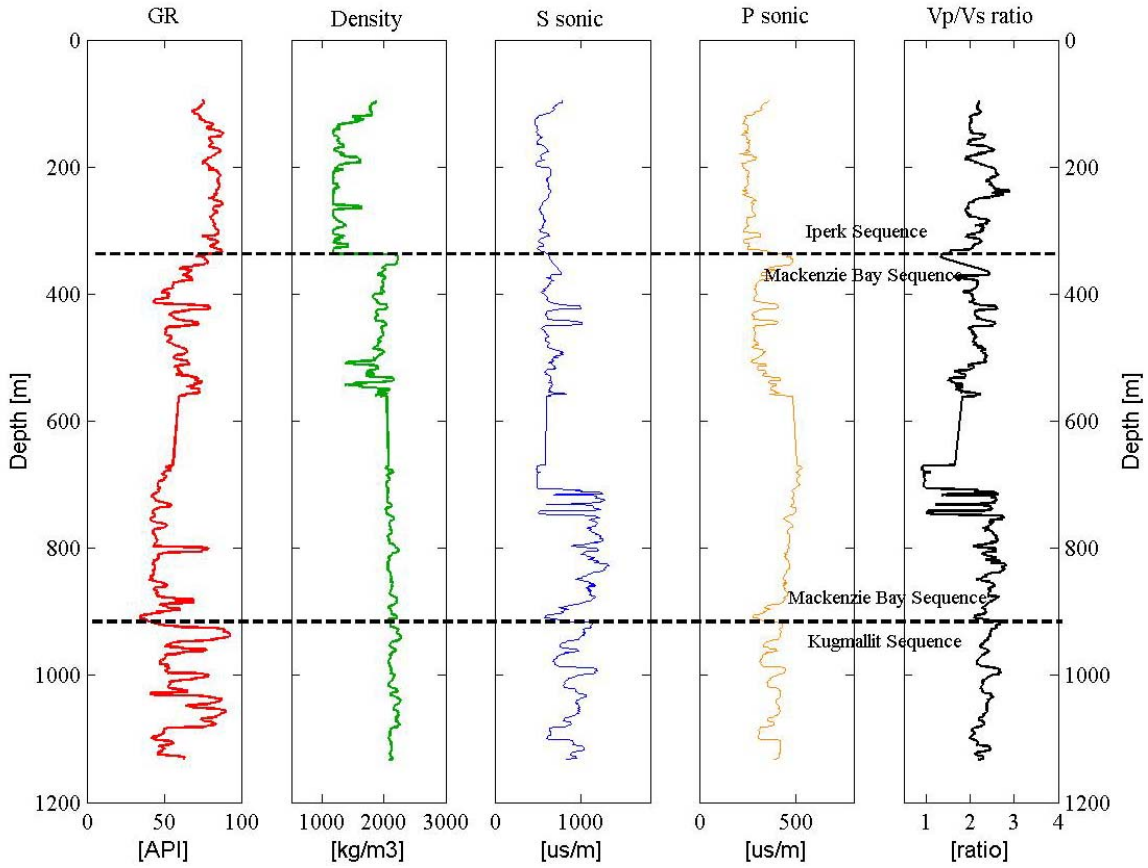

Figure 4.3 Mallik 2L-38 well logs (used by several authors to evidence the presence of gas hydrates in the Mackenzie Delta). The base of ice-bearing permafrost occurs at 640 m deep. The section from 550 m to 718 m was omitted when estimating the Vp/Vs ratio for the lower and upper part of the Mackenzie Bay Sequence (modified from Mi *et al.*, 1999)

A well, relatively close to the area of study is the Mallik 2L-38 (Figure 4.3). Mi *et al.* (1999) provide a detailed discussion of the stratigraphy of this well. They indicate that the upper sequence (Iperk from 0–346 m) is mainly composed of ice-bonded sand with occasional silt and clay layers. The Mackenzie Bay sequence (346-926 m) consists of sand and weakly cemented sandstone with silt/shale interbeds. The Kugmallit sequence

extends below 926 m. The base of the permafrost is at about 640 m and gas hydrates occur between 897 m and 1110 m. VSP and full-waveform sonic logs give P and S-wave velocities of about 3300 m/s and 1500 m/s, respectively, above the base of the permafrost. There is a marked decrease in P and S velocities below the permafrost (to 2100 m/s and 700 m/s). In the gas-hydrate section, the velocities increase to about 2600 m/s for the P waves and 1100 m/s for the S waves. We note that the Vp/Vs value is significantly lower (about 2.4) in the permafrost and gas-hydrate bearing strata than the intervening region that has a Vp/Vs value of about 3.1.

4.2- *Well site description: Hansen Harbour G-07*

A suite of 10 logs was acquired at the well Hansen G-07 (Figures 4.4 and 4.5). This is an Imperial Esso well located in Hadwen Island (Figure 4.1). It is reported as an oil and gas-producing well (Dixon *et al.*, 1992). This well was logged to approximately 3250 m deep. Spontaneous potential, gamma-ray, caliper logs were acquired from 521.8 m to 3275 m depth. Sonic, density, resistivity (shallow, medium, deep) and porosity were acquired from 1196 m to 3275 m depth. Using the GR and SONIC logs, three lithological boundaries separating four different lithological formations were identified (Figure 4.4 and Table 4.1). The notation used to define the mentioned lithology is sequences A, B, C, and D. A identifies the shallowest between them and the contacts are the following: L1 (between A and B), L2 (between B and C) and L3 (between C and D) (Figures 4.4 and 4.5).

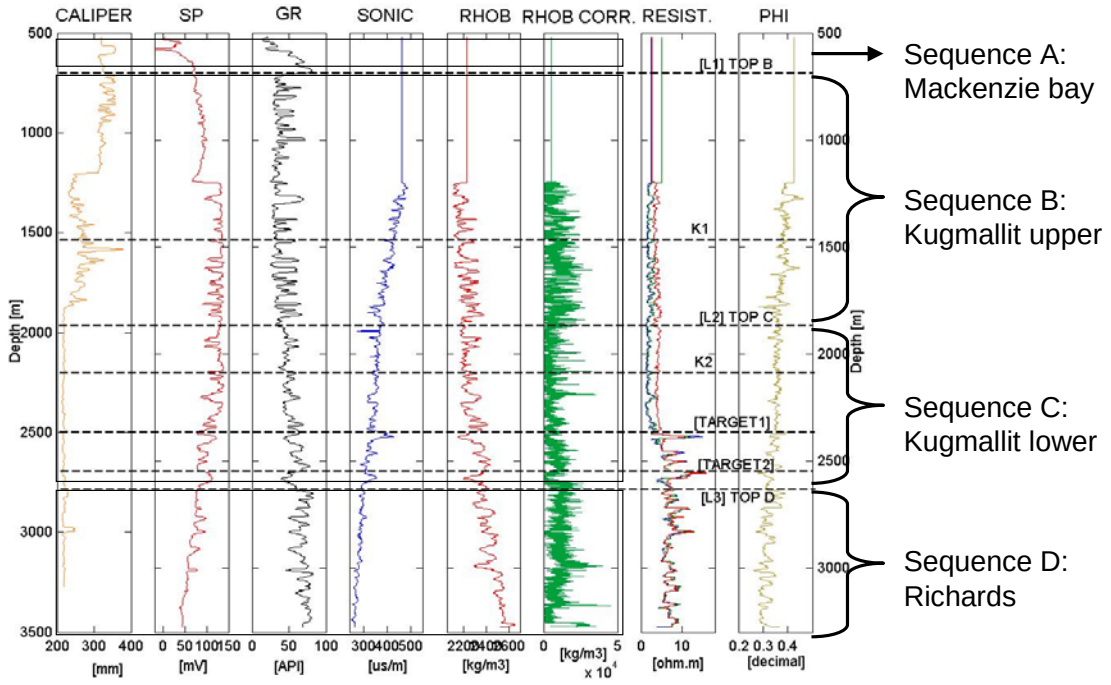

Figure 4.4 Hansen Harbour G-07 well logs. Observe that the SP, gamma ray and caliper logs were acquired from 521.8 m to 3275 m, and the rest went up to 1196 m only. Based on the GR log the lithology of this well was separated into 4 sequences: A, B, C, and D, A being the shallowest and D the deepest sequence. Notice the two target zones defined in the sequence C.

Boundary	Depth [m]
[L1] Top B	691.4
[L2] Top C	1871.5
[L3] Top D	2636.9
Top target 1	2372.9
Base target 1	2403.9
Top target 2	2548.8
Base target 2	2592.5

Sequence	Thickness [m]
B	1180.1
C	765.4
D	Undetermined
Target 1	31.0
Target 2	43.7

Table 4.1 Depth and thicknesses for defined sequences in the Hansen G-07 well.

Sequence A: consists of a thick shale body with a sand interval over it (Figure 4.4). The top of this sequence could not be defined since it is out of the logged interval. The caliper response for the shale body indicates a competent rock.

L1 boundary is defined as a lithological contrast at 691.4 m deep that separates the shale body (*sequence A*) from the underlying *sequence B* that consists of a succession of shale and unconsolidated to consolidated sands.

Sequence B: ranges from L1 (691.4 m deep) to L2 (1871.5 m depth). Thickness of this sequence is 1180.1 m. The lithology of this sequence is a succession of shale (from 10 to 40 m) and sand (10 to 90 m) bodies. The predominance of sand in this sequence is easily observed on the gamma-ray log. At 1196 m the remaining logs (sonic, resistivity, density and porosity) started to be recorded.

L2 boundary is defined at 1871.5 m deep. It separates two different lithological successions (B and C). The contrast in the gamma-ray log distribution gives evidence of the contact. This is seen, as well, in a difference in the shape of the density and sonic log.

Sequence C consists of a succession of thicker more competent sand (40 m to 100 m) and shale (10 to 50 m) layers with a total thickness of 765.4 m. This sequence has more shale content than *sequence B* (observe how the gamma ray values are higher on average (Figure 4.4). Two seismically recognizable layers are present in this sequence, *TARGET 1* and *TARGET 2*, (Figure 4.5 and Table 4.2). These bodies are attractive because of their high deep, medium, and shallow resistivity values (Figure 4.5).

L3 boundary is defined at 2650-m deep. This contact divides *sequence C and D*. A thick low velocity layer, approximately 60 m thick, lies over a sequence of dominantly shale layers.

Sequence D is more shally than the overlying sequence. The lithology of this sequence is mostly shale intercalated with a few thin sand layers (from 10 to 30 m thick).

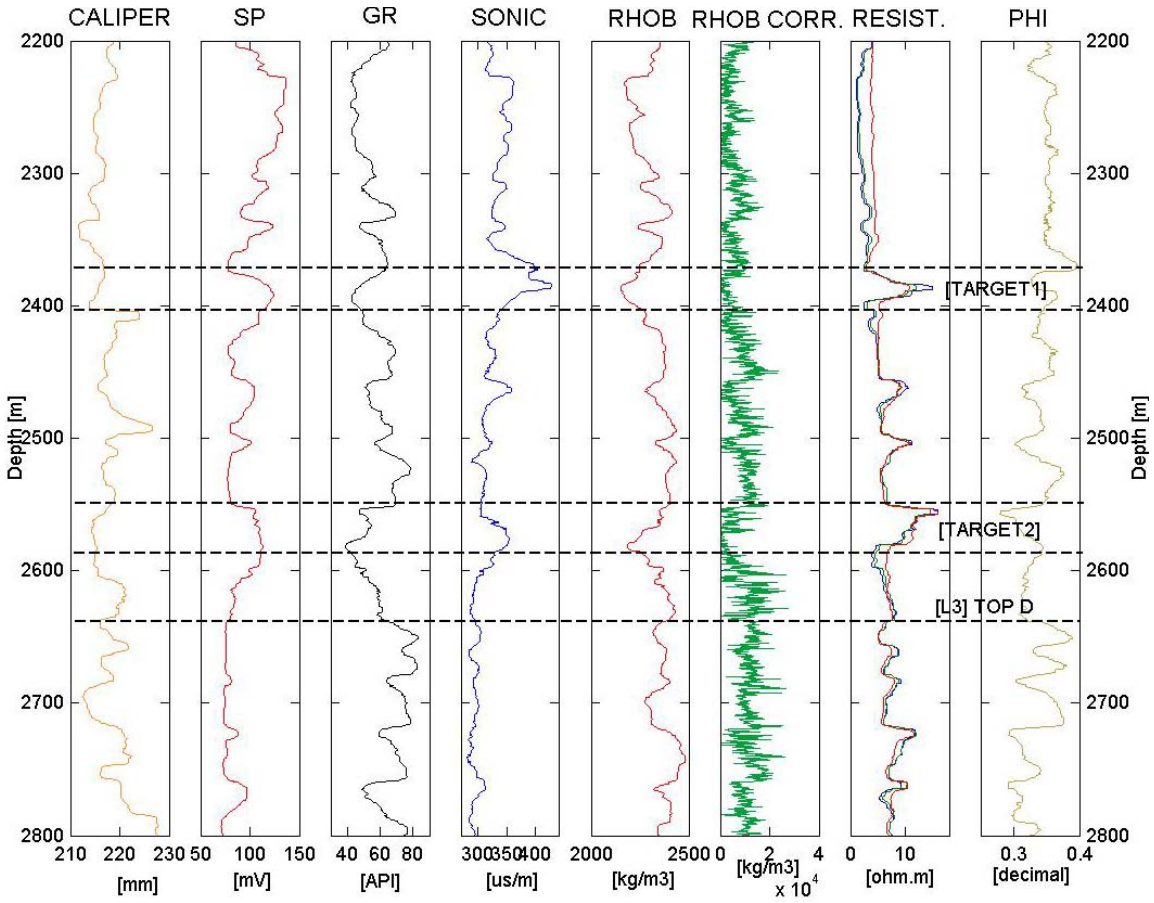

Figure 4.5 Target zones in the Hansen G-07 well. Notice the two bodies defined in the sequence C as TARGET1 and TARGET2. These were marked because of their sonic and resistivity contrast which should be seismically recognizable.

Sequence	Vp [m/s]				Density [kg/m^3]			
	Mean	Median	Min.	Max	Mean	Median	Min.	Max
TARGET 1	2628	2595	2972	2340	2200	2199	2150	2276
TARGET 2	3030	3040	3307	2822	2294	2286	2187	2401

Table 4.2 Statistics for targets in *sequence C* [Hansen G-07 well]

4.3- *3C-2D seismic survey Hansen Harbour*

A series of seismic lines were acquired in a transition zone, from shore to sea, in the Mackenzie Delta, N.W.T. (Figure 4.6). A 2 m thick layer of ice is floating on the ocean,

and a similar layer of packed snow, ground – fast ice, covers the beach. These lines were part of a survey test carried by Devon Energy in the Mackenzie Delta with the objective of testing different types of receivers, as well as sources. The total length of the seismic lines was six kilometres. Station 101 was on the floating ice at the north end, and station 501 was on the ground-fast ice at the south end.

Different types of receivers (conventional and 3-C sensors), and two different source types (Vibroseis and dynamite) were used in this project. A detailed description and discussion of the acquisition is given by Hall *et al.* (2001 and 2002). From these works it is relevant to mention that the program consisted of five active seismic lines:

Single hydrophones (line 1): consisted of 64 hydrophones at 45 m station spacing, inserted into the seafloor under the floating ice (north half of the line only).

Single deep marshphones (line 2): consisted of 132 single marshphones deployed every 45 m from stations 103 to 499 (Figure 4.7). They were inserted into the mud on the sea floor on the north part of the line, and into the frozen ground beneath the ground-fast ice to the south.

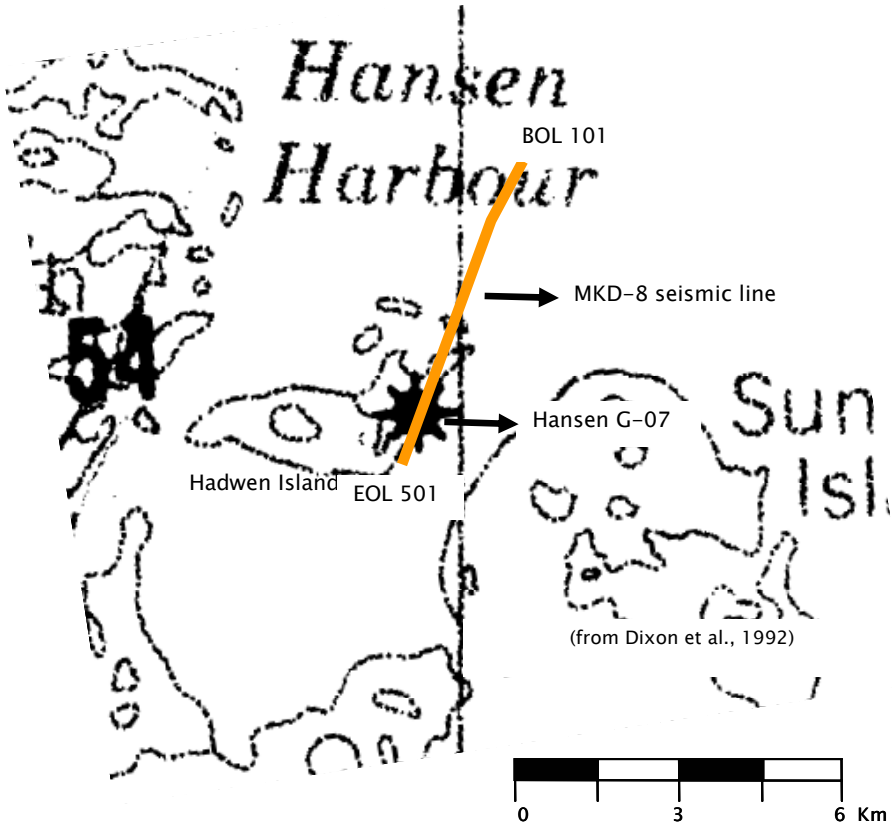

Figure 4.6 Hansen Harbour-Mackenzie Delta area, N.W.T. The six-kilometer MKD-8 seismic line is located along a transitional path from floating ice (BOL101) to ground-fast ice (EOL101). Hansen G-07 is an Imperial Esso well. It is classified as an oil & gas producing well, but no other information is available.

Single shallow marshphones (line 3): consisted of 133 single marshphones deployed between stations 102 and 501 at a 45 m receiver interval (Figure 4.7). These phones were planted just below the surface of the floating ice and the ground-fast ice in augured holes approximately 0.3 m deep.

Six geophone arrays of vertical elements (line 4): consisted of 133 six geophone strings of marshphones 2 m apart. They were deployed between stations 101 and 500 at a 45 m group interval (Figure 4.7). These phones were planted on the surface of the ice using a cordless drill.

Single 3C – geophones (line 5): fifty 3-C geophones (Figures 4.7 and 4.8) were deployed between stations 272 and station 321 every 15 m, centred on the transition zone. The spikes were removed from these geophones, and they were frozen into the bottom of ~0.4 m deep augured holes with fresh water (Figure 4.8).

Three different seismic sources were used as well: Vibroseis, dynamite and sledge hammer. Vibroseis and dynamite covered the entire length of the line while the hammer survey consisted of vertical and 45 degree hits on ice every meter for thirty meters and the floating ice only.

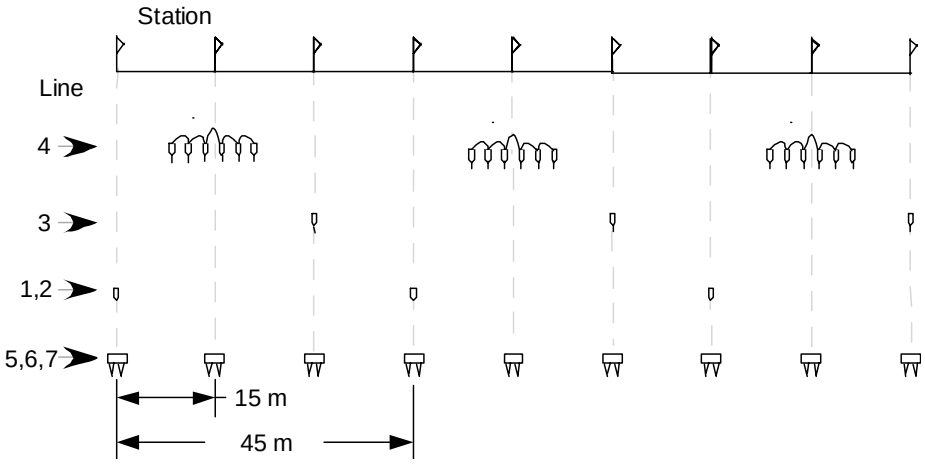

Figure 4.7 Diagram of receiver layout: line 1: single hydrophones; line 2: single deep marshphones; line 3: single shallow marshphones; line 4: six geophone arrays of vertical geophones; line 5: H1 component of 3-C geophones; line 6: Vertical component; Line 7: H2 component.

Vibroseis (source line 1): vibrator points were on every half station with the vibrators centred in-line, from stations 101.5 to 501.5. The linear sweep used for this test line was 6-96 Hz over 32 seconds, and the correlated records are eight seconds long.

Dynamite: Line shot with dynamite at 90 m station spacing. On the floating ice, an in-line five hole pattern (north/south) with 2 kg per hole was used. If the charge could not be placed at least 7 m below the seafloor the shot point was not used. On the ground-fast ice, single 20 kg charges at a depth of 20 m were used.

Figure 4.8 Typical 3-C geophone plant in an augured hole in the sea ice. Geophones were frozen in with fresh water.

Sledge hammer: A twelve pound sledge hammer was pounded on the ice surface from station 285 to station 287, for a total source line length of thirty meters. Three shots were recorded every meter, 1) a vertical hit, 2) a 45° hit into a V shaped notch in the ice towards the east, and 3) a 45° hit on the opposite side of the notch, towards the west. An audible tone was transmitted from the recorder for timing, so time-zero depended on human reflexes, and is different for every shot record.

4.4- *PP and PS seismic correlation*

The migrated seismic lines resulted from the dynamite source was used to make a correlation with well log data from Hansen G-07. The results from the correlation have been published (Nieto *et al.*, 2003). Geological data from a compilation, plus two well locations were merged to build a proper velocity model for the area.

Geological model for the study area

A model for the surrounding area of the Hansen Island was defined using the isopach maps (modified from Dixon *et al.*, 1992) of all the geological sequences. This model consists of the following sequences:

Iperk: because the logging starting depth was 500 m, this sequence is not expected to be present at this location. Even though, it should be appear in the shallow part of the seismic section.

Akpak: Is not present at this location as it wedges to zero thickness.

Mackenzie: This sequence should be present depending on the real thickness of this sequence at G-07 and should be represented by the first 200 m of the well logs (Figure 4.4).

Kugmallit: A complete section of Kugmallit should have been logged at G-07 and should be 1800 m approximately (Figure 4.4).

Richards: The presence of this sequence depends on the real thickness of the Kugmallit Sequence. If it is present, it should appear at the very bottom of G-07 with a total thickness of 1400 m approximately.

The interpretation of the G-07 logs and the geological interpretation were merged to make a depth model. The depth model from isopach maps was used to guide this interpretation:

[L1] TOP B: Mackenzie Bay Sequence and Kugmallit Sequence contact.

[L2] TOP C: interface where the Kugmallit Sequence become shale-dominant.

[L3] TOP D: Kugmallit Sequence and Richards Sequence contact.

Sequence A [Mackenzie Bay Sequence]: the thickness cannot be calculated.

Sequence B and C [Kugmallit Sequence]: the thickness was 1945.5 m.

Sequence D [Richards Sequence]: the thickness cannot be calculated.

PP and PS real to synthetic seismic sections correlation

Using the "synth" application from the CREWES MATLAB Seismic Toolbox several synthetic sections were created (Figures 4.9 and 4.10). The objective was to interpret the PP and PS seismic sections obtained with the 3C geophones in the Hansen Harbour area. The parameters used to define the synthetic sections are:

Type of section: NMO removed;

Maximum offset = 1500 m;

Offset increment = 100 m;

Offset/depth ratio = 1;

Vp/Vs ratio = variable from 1.6 to 2.8;

Ricker wavelet, 30 Hz dominant frequency; and

No attenuation or geometrical spreading effects included.

Since no shear-wave sonic log was acquired at Hansen G-07, several panels with different constant V_P/V_S ratios were created to define an appropriate V_P/V_S depth function.

A reasonable correlation was found between the PP synthetic stacked seismic section from Hansen G-07 and the PP migrated seismic section from Hanson (Figures 4.9 and 4.10). Although the indicators used to correlate the well data are not easily recognized, both the Kugmallit – Richards sequence contact and the target zones at the bottom of the Kugmallit Sequence were successfully identified in the PP seismic section.

Once the PP section has been interpreted, the next thing to do is analyze the PS section. An estimation of V_P/V_S ratio for different sequences from a relatively close well was done. The closest well that had both P-wave and S-wave sonic logs, as well as other logs, and that has been extensively studied is the Mallik 2L-38 (Figure 4.3). The sequences found at this location are: Iperk, Mackenzie Bay, and Kugmallit. The base of the permafrost occurs at 640 m (Mi *et al.*, 1999). The V_P/V_S curve was calculated from the sonic logs (Figure 4.3). An average ratio for each sequence was taken from this log (Table 4.3).

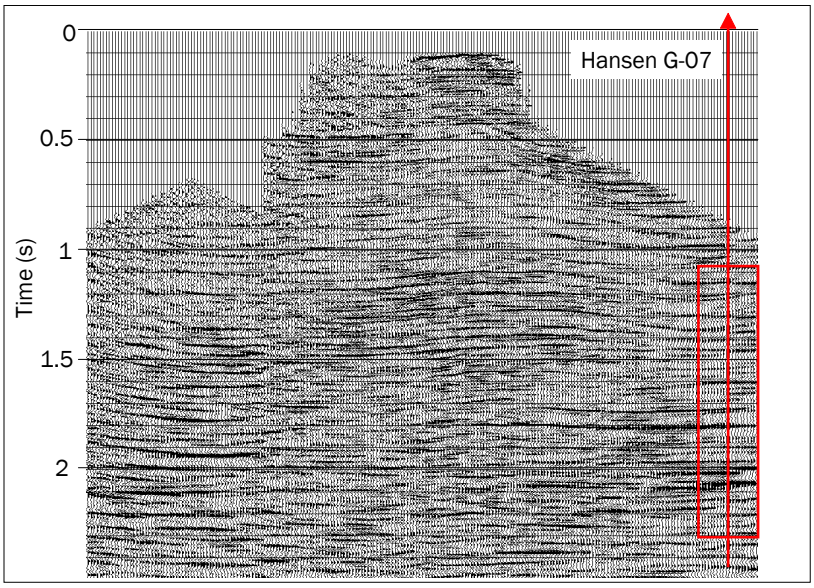

Figure 4.9 PP migrated seismic section. The rectangle highlights the area close to the G-07 well.

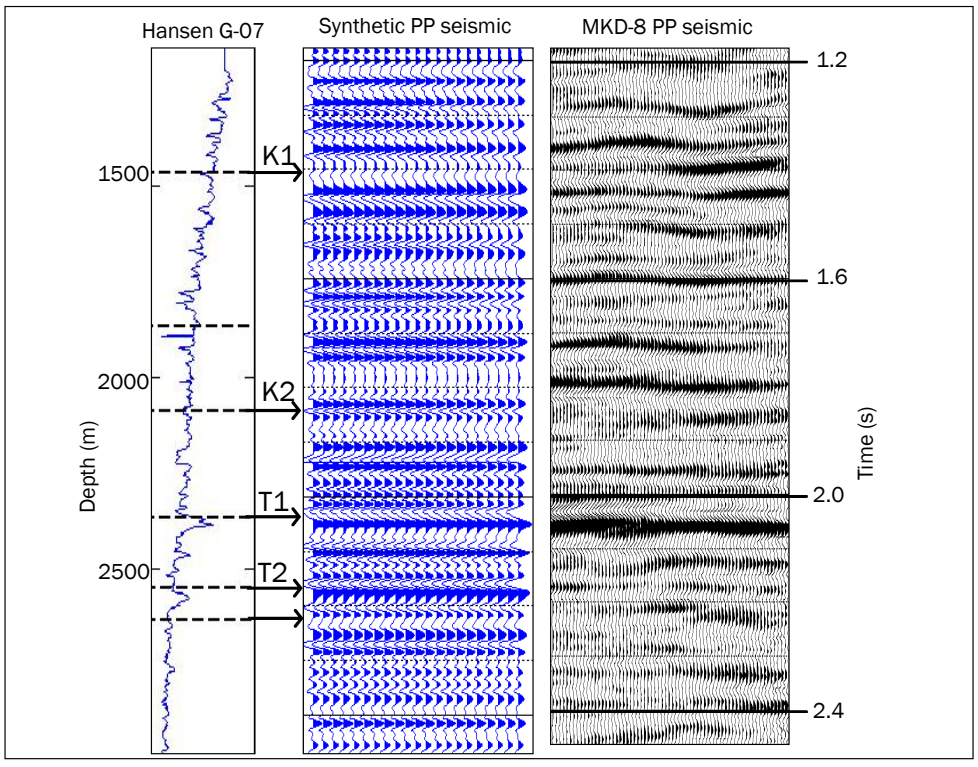

Figure 4.10 PP seismic data correlation. The traces displayed in the left panel correspond to the synthetic NMO removed seismic section. Observe that the targets are not easily recognized in the section. The absence of shallow data doesn't allow the interpretation of the Kugmallit / Mackenzie Bay boundary.

Sequence	Vp/Vs values			
	Mean	Median	Minimum	Maximum
Iperk	**2.19**	**2.17**	1.44	2.90
Upper Mackenzie Bay	**2.04**	**2.08**	1.31	2.62
Lower Mackenzie Bay	**2.41**	**2.46**	1.42	2.81
Kugmallit	**2.30**	**2.30**	1.98	2.69

Table 4.3 Vp/Vs values for Mallik 2L-38 well

Notice that the Mackenzie Bay may be separated into two different zones, based on the V_P/V_S values (Table 4.3). The reason that the V_P/V_S changes across the sequence is the transition from permafrost to non-frozen rock which occurs at about 640 m deep (Figure 4.3). The upper part has a value of 2.04 (frozen) and the lower 2.41 (unfrozen). The value Vp/Vs for the Iperk Sequence is 2.19, which is larger than the Mackenzie Bay, indicating a change in lithology.

The average V_P/V_S in the upper part of the section (Iperk and Upper Mackenzie Bay sequences) is 2.1, which corresponds to the permafrost section. An average V_P/V_S for the lower part of the section (Lower Mackenzie Bay and Kugmallit) is 2.4.

Using several V_P/V_S values, the PP and PS real sections were compared. Two reflectors "K1" and "K2" were originally defined to help interpret the PS section, (Figure 4.4). Both are part of the Kugmallit Sequence.

The PS section was stretched to match the PP time scale by a factor $t_{PS}/t_{PP} = 1.55$, which corresponds to the average V_P/V_S of 2.1 obtained from the well Mallik 2L-38. Several other values were used as well, and the highest correlation between the PP and PS sections was obtained by using a $t_{PS}/t_{PP} = 1.45$, which corresponds to a V_P/V_S of 1.9 (Figure 4.11). The correlation was done based mainly on the seismic character

(amplitude, continuity) of the reflectors K1 and K2 and omitting any structure around the edges. A low pass frequency filter, 45 Hz, was used to correlate the events K1 and K2. Reliability of the interpretation in the deep area (K2 indicator) is not so high since *there is no control of the shallow velocity and density values*. This represents a preliminary approach, since the PS section looses seismic character under K1.

The PS synthetic section was included in the analysis to make a final interpretation. PP and PS synthetic seismic sections were modeled using constant V_P/V_S value of 1.9. These sections were correlated with the PP and PS migrated seismic sections, reaffirming the interpretation of the data (Figure 4.12).

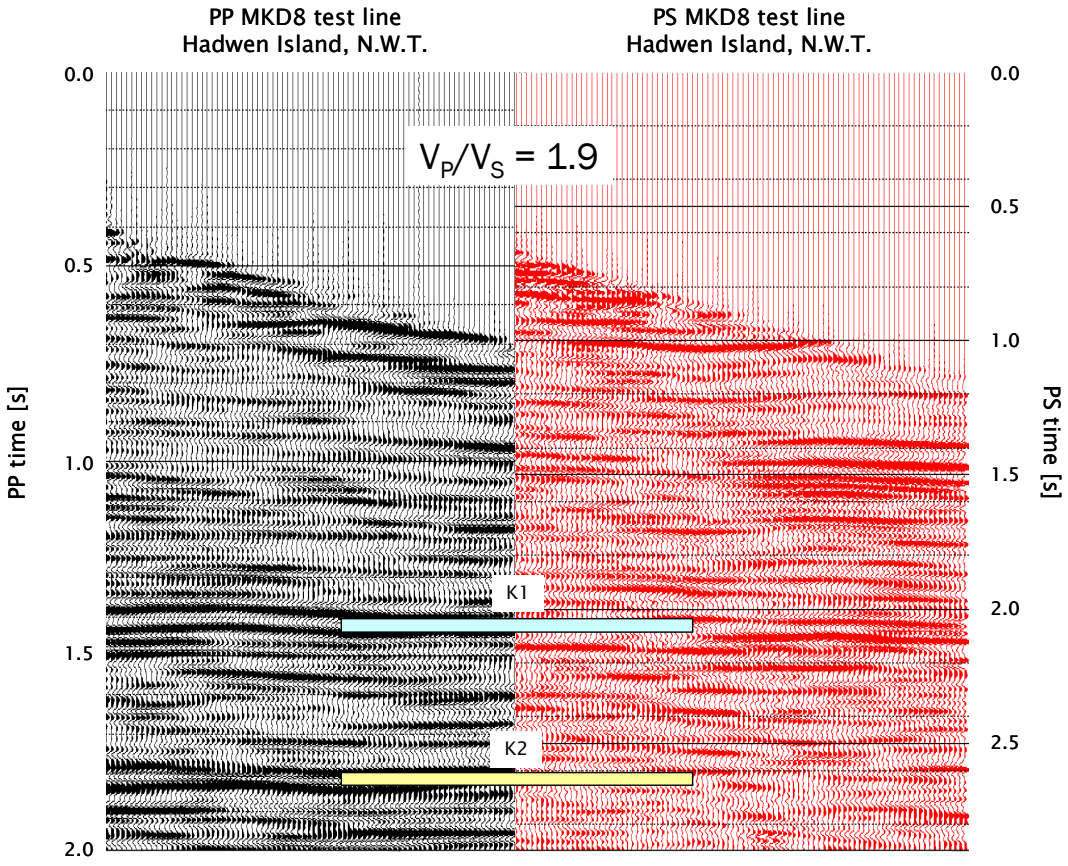

Figure 4.11 PS NMO removed seismic data correlation. The targets are not easily recognized in this section either, but the reflectors K1 and K2 serve as a reference in the Kugmallit Sequence.

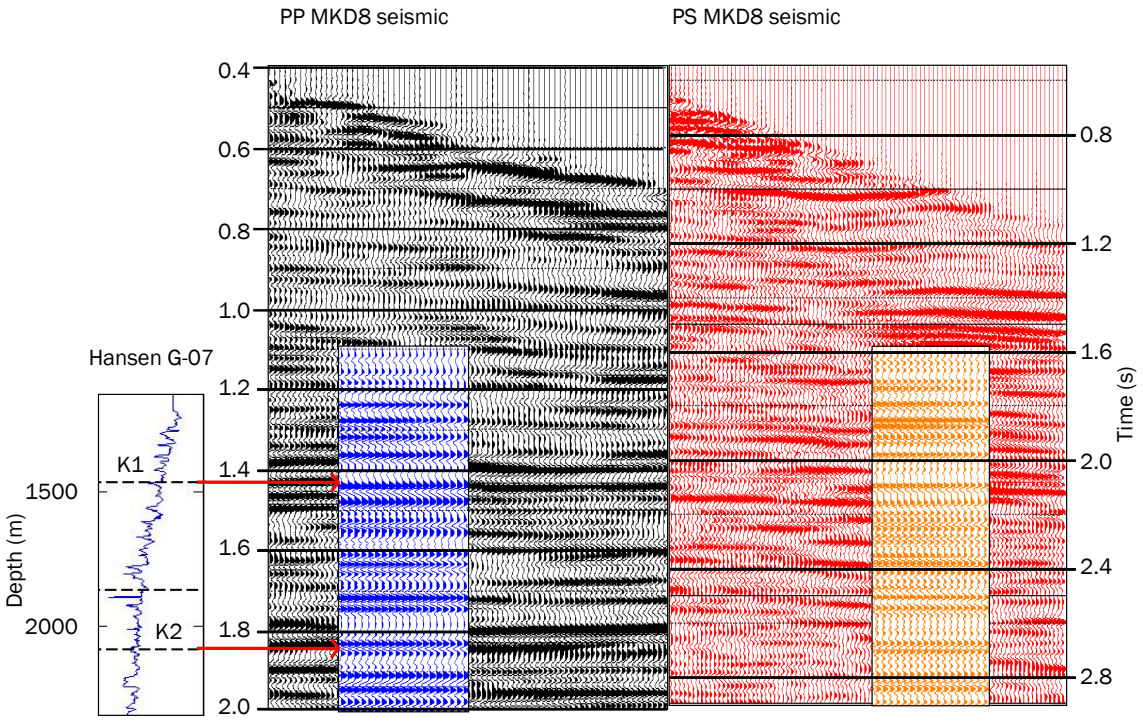

Figure 4.12 Final correlation of the PP and PS synthetic section with the MKD-8 seismic line. From left to right: MKD-8 PP seismic section (black); Hansen G-07 PP seismic section (blue), Hansen G-07 PS seismic section (orange); MKD-8 PS seismic section (red). The synthetic seismograms start at 1 sec PP time, equivalent to 1.5 sec PS time, approximately, due to the absence of the shallow part of the well logs.

CHAPTER FIVE: *CONCLUSIONS AND FUTURE WORK*

Two different objectives were met with the completion of this research: (1) to determine some of the capabilities and limitations of seismic and GPR exploration techniques for near-surface imaging in periglacial environments, and (2) to process and interpret PP and PS seismic sections from the Mackenzie Delta. These experiments took place in two different locations in the Canadian Arctic: Devon Island, Nunavut, and Mackenzie Delta, Northwest Territories. The Devon Island study focuses on the evaluation of geophysical exploration techniques for the study of aqueous and frozen ground systems for future application to Mars exploration. Both seismic and ground-penetrating radar surveys were acquired and evaluated in the base camp of the Haughton-Mars Project. The second part of this thesis focuses on the interpretation of a 3C-2D seismic survey acquired in a transition zone of the Mackenzie Delta, Northwest Territories, and recorded by the CREWES Project at the University of Calgary.

The following sections summarize results presented in this thesis:

5.1- *Near-surface seismic surveying*

(1) I find that velocity of compressional wave increases considerably due to freezing in the near-surface. As a consequence of this, a large P-wave reflection coefficient is obtained.

(2) Modeling indicates the seismic reflection methods to be limited due to:

- *A small critical angle of incidence*: which causes poor transmission of homogeneous waves to the sub-permafrost layers, reducing the possibility of imaging sub-permafrost unfrozen bodies (taliks), if present; and causing reverberations and multiples that contaminate the reflections.

- *A P-wave transmission coefficient considerably smaller than the reflection coefficient*: coupled with attenuation and amplitude further reduces more the possibility of imaging an intra-permafrost talik.

(3) Direct and refracted PP and PS waves were interpreted from the seismic gathers. A reflection event from the thawed – frozen layer interface was not identified in any of the records due to the small time difference between the direct and reflected wave for the near-offset traces. No obvious reflections from deeper interfaces were identified.

(4) The head-wave energy was used to image the interface between thawed and frozen layer interface. A processing flow was designed to obtain a seismic image. It consists of four main steps: balance and equalization, signal separation, linear moveout correction and stack.

(5) In the final pseudo zero-offset stacked section or volume, the parameter that is related to the structure of the permafrost top is the pseudo zero-offset time since it is a direct function of the depth to the refracting surface below the source location.

(6) A number of values were obtained from these experiments:

- An average thickness of 0.6 m for the active layer around the study area.
- From the 2D experiment, the vertical component of the data yields a velocity value of 263 m/s and the inline component a value of 256 m/s. In a previous study, values for compressional and shear wave velocities of *260 and 168 m/s*, with V_P/V_S *of 1.55* in the very near surface were reported (Nieto *et al.*, 2002).
- A velocity of 2244 m/s was estimated from the *PPP* head wave arrivals observed in the vertical component geophones. From a previous investigation (Nieto *et al.*, 2002)

velocity for compressional head waves in permafrost of 3100 m/s and a shear wave velocity of *2030 m/s,* with a V_P/V_S *ratio of 1.53* were obtained.

(7) From recording the 3C-3D seismic survey it was found that:

- The procedure to record this survey was similar to that of a standard rectangular 3D seismic exploration survey but on a smaller scale.
- Rotation of horizontal component data from the H1 – H2 field directions to the *radial-transverse* is required to obtain a seismic image. The geometrical rotation method was used for this survey due to its practicality.
- In the processing flow: a binning of offset values is required to avoid aliasing problems when transforming to the radial domain.
- A single LMO correction velocity of 2500 m/s for P wave and 1500 m/s for S wave, yielding a V_P/V_S ratio across the area of 1.67.
- LMO velocity variation is observed across the study area, and is attributed to dips in the top of the frozen layer.

In general, the refraction seismic method was found to be more applicable to this case of study than the reflection seismic method. It is possible to improve 3D seismic refraction image of the shallow subsurface by modifying the acquisition geometry.

5.2- *Near-surface ground-penetrating radar surveying*

The motivation for using ground-penetrating radar in this project is based in the dielectric properties contrast which is found between frozen and unfrozen sediments. The use of constant-offset ground-penetrating radar lines allows a fast study of the area due to the simple processing steps required to obtain an image: trace DC removal, automatic gain control and high cut frequency filter. Disadvantages are the impossibility of using

variable-offset tools such as: analysis of signal variation with offset (AVO), measurement of propagation velocities of direct, refracted or reflected modes, stacking to obtain a greater S/N ratio. A number of ground-penetrating radar experiments were acquired to image the frozen-unfrozen sediment interface. From these, it was found that GPR velocity curves for the active layer: these are important for time to depth conversion, and interpretation of GPR data.

A change in the slope of the time-depth crossplot of signal arrival values is interpreted as radar velocity change. This change responds to the contrast between saturated silt and saturated sand observed in the test pit. A third velocity model was obtained by fitting *hyperbolas* to the rebar diffractions at different depth values. It grossly correlates with the RMS velocity curve but with some differences. Difference between these models is due in part to approximating constant-offset velocity estimation with a variable-offset.

From the 3D GPR survey, it was found that an additional interpolation step is required to fill in the gaps due to the acquisition geometry. This step consisted of two passes of linear interpolation, first in the crossline and second in the inline directions, and averaging both results to obtain the final image. An acquisition footprint marked by the recorded lines is observed in the time slices. They are interpreted to be caused by out-of-plane reflections.

5.3- ***3C-2D seismic interpretation in the Mackenzie Delta***

A theoretical geological model of the Hansen Harbour area was defined from the compilation of isopach maps, structural maps, seismic sections and well logs. Three lithological boundaries separating four different lithological formations were identified using the GR and SONIC logs of the G-07 well. These units were correlated with the

migrated seismic lines resulted from the dynamite source. The results from the correlation have been published (Nieto *et al.*, 2003).

A velocity model, V_P and V_S, was built using geological data from a compilation, plus sonic logs from two different wells: G07 and Mallik 2L-38. The interpretation of PP and PS seismic sections is based on synthetic seismic sections calculated from the velocity model. A good correlation was found between the PP synthetic stacked seismic section from Hansen G-07 and the PP migrated seismic section from Hanson.

To interpret the PS seismic section and correlate it to the PP, a series of V_P/V_S ratios were analyzed. Two reflectors “K1” and “K2” were originally defined to help interpret the PS section, which are both part of the Kugmallit Sequence. The stretch factor used to match the PS section to the PP time scale was t_{PS}/t_{PP} = 1.45, which corresponds to the average V_P/V_S of 1.9. In the correlation of the PP and PS sections, the seismic character (amplitude, continuity) of the reflectors K1 and K2 was used. A low pass frequency filter, 45 Hz, was used to correlate the events K1 and K2.

5.4- ***Future work***

The Devon Island study offers several routes for the continuation of research in near-surface seismic surveying of periglacial environments. I recommend the next step to be taken in this area is in the laboratory measurement of (1) compressional and shear-wave velocity variation with temperature and (2) attenuation coefficients, for P and S-wave, plus their variation with temperature. Samples of soil from different depths are available for these experiments. The estimation of these parameters would serve as input for elastic-wave seismic modeling. The usefulness would be to use correct velocities to model different scenarios and design appropriate survey geometries. Results from this

analysis would indicate the requirements to be able to record a standard reflection seismic line. It will also help in investigating the possibility of recording reflected signals from below the top of the frozen soil.

The seismic images shown throughout this project are obtained from processing the refracted wave instead of the reflected wave, as is normally done. For this case of study, a *flat* reflecting/refracting *interface* (frozen/unfrozen sediments interface) allows this method to be equivalent to a pseudo zero-offset seismic section. Modeling a depth-varying single interface would indicate the usefulness of this methodology.

From the ground-penetrating radar section, an area where many improvements can be made is the definition of volumes from a series of orthogonal lines. Different interpolation techniques can be analyzed using the dataset acquired in this project. A new dataset of multi-offset ground-penetrating radar is available for further analysis such as the amplitude variation with offset and its relation with water saturation of the sediments, or the use of seismic processing techniques.

REFERENCES

Bachrach, R., J. Dvorkin, and A. Nur, 1998, High-resolution shallow-seismic experiments in sand, Part II: Velocities in shallow unconsolidated sand: Geophysics, **63**, 1234-1240.

Bancroft, J., 2001, Seismic imaging: Course notes, The University of Calgary, Department of Geology and Geophysics.

Bland, H., and E. Gallant, 2001, A simplified tap test method for multicomponent seismic surveys: CREWES Research Report **13**, 17-28.

Davis, J.L. and A.P. Annan, 1989, Ground-penetrating radar for high resolution mapping of soil and rock stratigraphy. Geophysical Prospecting, **37**, 531-551.

DiSiena, J.P, J.E. Gaiser, and D. Corrigan, 1984, Horizontal components and shear waves analysis of three-component VSP data, in N. Toksoz and R.R. Stewart, eds., Vertical seismic profiling: advanced concepts: Geophysical Press, Vol. 15B.

Dixon, J., J.R. Dietrich and D.H. MacNeil, 1992, Upper Cretaceous to Pleistocene sequence stratigraphy of the Beaufort-Mackenzie Delta and Banks areas, northwest Canada: Geological Survey of Canada, Bulletin 407.

Dixon, J., J.R. Dietrich, D.H. McNeil, and L.S. Lane, 2001, Geological framework of the Beaufort-Mackenzie Basin: Annual National Convention Abstracts, Canadian Society of Petroleum Geologists, 103-104.

Dufour, J., D.C. Lawton and S. Gorek, 1996, Determination of S-wave static corrections from S-wave refractions on P-S data: 66th Annual International Meeting, SEG, Expanded Abstracts, 1551-1554.

French, H.M., 1996, The periglacial environment, Longman.

Guevara, S., 2001, Analysis and filtering of near-surface effects in land multicomponent seismic data: M.Sc. thesis, University of Calgary.

Hall, K., C. Nieto, E. Gallant and R. Stewart, 2001, Multicomponent seismic survey over ground-fast and floating ice, Mackenzie Delta, N.W.T.: CREWES Research Report, **13**, 29-38.

Hall, K.W., C.E. Nieto, E.V. Gallant, R.R. Stewart and P. Cary , 2002, Multicomponent seismic acquisition in the Mackenzie Delta, N.W.T.: Annual National Convention, CSEG, Canadian Society of Exploration Geophysicists, MCC-1.

Henley, D.C., 2003, Coherent noise attenuation in the radial trace domain: Geophysics, **68**, 1408-1416.

Jolly, R. N. and J.F. Mifsud, 1971, Experimental studies of source-generated seismic noise: Geophysics, **36**, 1138-1149.

King, M.S., 1984, The influence of clay-sized particles on seismic velocity for Canadian Arctic permafrost: Canadian Journal of Earth Sciences, **21**, 19-24.

Kurfurst, P.L., 1976, Ultrasonic wave measurements on frozen soils at permafrost temperatures: Canadian Journal of Earth Sciences, **13**, 1571-1576.

Lee, P., 2002, Mars on Earth: The NASA Haughton-Mars Project: Ad Astra, National Space Society, **14**, 12-17.

Lee, P., 2002, From Earth to Mars, Part One: A crater, ice, and life: The Planetary Report, **1**, at http://www.planetary.org/html/Devon_Island/Devon_TPR1.htm

Lee, P., 2002, From Earth to Mars, Part Two: Robots and humans working together: The Planetary Report, **1**, at http://www.planetary.org/html/Devon_Island/Devon_TPR2.htm

Leslie, J. M. and L.C. Lawyer, 1999, A refraction-seismic field study to determine the anisotropic parameters of shales: Geophysics, **64,** 1247-1252.

Long, M.E., 1999, Mars on Earth: National Geographic, **196**, 34-51.

Mayr, U., T. de Freitas, B. Beauchamp and G. Eisbacher, 1998, The Geology of Devon Island North of 76º, Canadian Arctic Archipelago: Geological Survey of Canada, Bulletin 526.

Mi, Y., A. Sakai, R. Walia, R.D. Hyndman and S.R. Dallimore, 1999, Vertical seismic profiling and seismic properties of gas hydrate in an Arctic well: CREWES Research Report, **11**, 705-726.

Moorman, B.J., and F.A. Michel, 2000, Glacial hydrological system characterization using ground-penetrating radar. Hydrological Processes, **14**, 2645-2667.

Nieto, C.E. and R.R. Stewart, 2002, Ultra high-resolution seismic imaging of permafrost, Devon Island, Nunavut: CREWES Research Report, **14**.

Nieto, C., and R. Stewart, 2003, Analyzing Multicomponent Seismic Data from the Mackenzie Delta, N.W.T.: Recorder, **28**, 36-39.

Nieto, C. and R. Stewart, 2003, Geophysical investigations at a Mars analog site; Devon Island, Nunavut: Third International Conference on Mars Polar Science and Exploration, 8115.

Nieto, C.E., and R.R. Stewart, 2003, Interpretation of PP and PS seismic data from the Mackenzie Delta, N.W.T.: CSPG/CSEG Joint Convention, Canadian Society of Petroleum Geologists and Canadian Society of Exploration Geophysicists.

Nieto, C.E. and R.R. Stewart, 2003, Ultra high-resolution seismic and GPR imaging of permafrost, Devon Island, Nunavut: CSPG/CSEG Joint Convention, Canadian Society of Petroleum Geologists and Canadian Society of Exploration Geophysicists.

Norminton, E. J., 1990, Seismic model studies of the overburden bedrock reflection: P-wave and s-wave: 60th Annual International Meeting and Exposition, SEG, Expanded Abstracts, 376-379.

Polczer, S., 2001, Game back on; exploration returns to the Mackenzie Delta after two-decade hiatus: Nickle's Petroleum Explorer, **8**, 4-5.

Pullan, S. E., J.A. Hunter and K.G. Neave, 1990, Shallow shear wave reflection tests: 60th Annual International Meeting and Exposition, SEG, Expanded Abstracts, 380-382.

Reynolds, C. B., I.B. Reynolds and W.C. Haneberg, 1990, Refraction velocity sections; an aid in shallow reflection interpretation: 60th Annual International Meeting and Exposition, SEG, Expanded Abstracts, 383-384.

Ross, E., 2003, New Mackenzie Delta play types identified: Petroleum Explorer, **10**, 6-13.

Szelwis, R. and A. Behle, 1987, Shallow shear-wave velocity estimation from multimodal Rayleigh waves: in S.H. Danbom and S.N. Domenico, eds., Shear-wave exploration: Society of Exploration Geophysicists, 214-226.

Telford, W.M., L.P. Geldart, R.E. Sheriff and D.A. Keys, 1976, Applied Geophysics. Cambridge University Press.

Timur, A., 1968, Velocity of compressional waves in porous media at permafrost temperatures: Geophysics, **33**, 584-595.

Vermeer, G., 2001, Understanding the fundamentals of 3D seismic survey design: First Break, **19,** 130-134.

Wilkin, D., 1998, NTI, Ottawa meet to set rules for High Arctic drilling**:** Nunatsiaq News. At http://www.nunatsiaq.com/archives/nunavut981130/nvt81120_06.html (published Nov 2004)

Williams, P.J. and M.W. Smith, 1989, The frozen earth: fundamentals of geocryology: Cambridge University Press.

Xia, J., R. Miller, C. Park, R. Nigbor, and E. Wightman, 1999, A pitfall in shallow shear-wave refraction surveying: 69th Annual International Meeting, SEG, Expanded Abstracts, 508-511.

Yilmaz, O., 2001, Seismic data analysis: processing, inversion and interpretation of seismic data: Society of Exploration Geophysicists.

Zimmerman, R.W. and M.S. King, 1986, The effect of the extent of freezing on seismic velocities in unconsolidated permafrost: Geophysics, **51**, 1285-1290.

APPENDIX A: *3C-2D AND 3C-3D SEISMIC SURVEYS GEOMETRY*

Channel number	Geophone number	Type	Channel number	Geophone number	Type
01	01	H1	31	11	H1
02	01	V	32	11	V
03	01	H2	33	11	H2
04	02	H1	34	12	H1
05	02	V	35	12	V
06	02	H2	36	12	H2
07	03	H1	37	13	H1
08	03	V	38	13	V
09	03	H2	39	13	H2
10	04	H1	40	14	H1
11	04	V	41	14	V
12	04	H2	42	14	H2
13	05	H1	43	15	H1
14	05	V	44	15	V
15	05	H2	45	15	H2
16	06	H1	46	16	H1
17	06	V	47	16	V
18	06	H2	48	16	H2
19	07	H1	49	17	H1
20	07	V	50	17	V
21	07	H2	51	17	H2
22	08	H1	52	18	H1
23	08	V	53	18	V
24	08	H2	54	18	H2
25	09	H1	55	19	H1
26	09	V	56	19	V
27	09	H2	57	19	H2
28	10	H1	58	20	H1
29	10	V	59	20	V
30	10	H2	60	20	H2

Table A.1 Convention used to connect the H1, V and H2 component of the geophones to the seismic recorder. 3C-2D seismic survey

Source location	FFID	1st receiver location	Last receiver location	First geophone	Last geophone	Notes
100	1000	101	139	1	20	
102	1001	101	139	1	20	
104	1002	101	139	1	20	
106	1003	101	139	1	20	
108	1004	101	139	1	20	
110	1005	101	139	1	20	
112	1006	101	139	1	20	
114	1007	101	139	1	20	
116	1008	101	139	1	20	
118	1009	101	139	1	20	
120	1010	101	139	1	20	
122	1011	101	139	1	20	
124	1012	101	139	1	20	
126	1013	101	139	1	20	
128	1014	101	139	1	20	
130	1015	101	139	1	20	
132	1016	101	139	1	20	
134	1017	101	139	1	20	
136	1018	101	139	1	20	
138	1019	101	139	1	20	
140	1020	101	139	1	20	
140	1021	101	139	1	20	VOID
140	1022	101	139	1	20	Used normal pellets
140	1023	101	139	1	20	No pellets

Table A.2 Observer report for 3C-2D high resolution seismic line.

Channel number	Geophone #	Sensor position		Channel number	Geophone #	Sensor position
1	1	H2		31	11	H1
2	2	H2		32	12	H1
3	3	H2		33	13	H1
4	4	H2		34	14	H1
5	5	H2		35	15	H1
6	6	H2		36	16	H1
7	7	H2		37	17	H1
8	8	H2		38	18	H1
9	9	H2		39	19	H1
10	10	H2		40	20	H1
11	10	V		41	20	V
12	9	V		42	19	V
13	8	V		43	18	V
14	7	V		44	17	V
15	6	V		45	16	V
16	5	V		46	15	V
17	4	V		47	14	V
18	3	V		48	13	V
19	2	V		49	12	V
20	1	V		50	11	V
21	1	H1		51	11	H2
22	2	H1		52	12	H2
23	3	H1		53	13	H2
24	4	H1		54	14	H2
25	5	H1		55	15	H2
26	6	H1		56	16	H2
27	7	H1		57	17	H2
28	8	H1		58	18	H2
29	9	H1		59	19	H2
30	10	H1		60	20	H2

Table A.3 Channel number correspondence with geophone number and sensor position.

Each trace has a header that contains a file number and a geophone number which are used to match source station and receiver station respectively. The correspondence between file numbers and source stations is based on the grid designed for the study area and is summarized in Table A.4:

File #	Source
3000	101
3001	102
3002	103
3003	104
3004	105
3005	106
3006	107
3007	108
3008	109
3009	301
3010	302
3011	303
3012	304
3013	305

File #	Source
4000	105
4001	106
4002	107
4003	108
4004	109
4005	110
4006	111
4007	112
4008	113
4009	305
4010	306
4011	307
4012	308
4013	309

File #	Source
5000	109
5001	110
5002	111
5003	112
5004	113
5005	114
5006	115
5007	116
5008	117
5009	309
5010	310
5011	311
5012	312
5013	313

File #	Source
6127	113
6000	114
6001	115
6002	116
6003	117
6004	118
6005	119
6006	120
6007	121
6126	313
6009	314
6010	315
6011	316
6012	317

File #	Source
7000	117
7001	118
7002	119
7003	120
7004	121
7005	122
7006	123
7007	124
7008	125
7009	317
7010	318
7011	319
7012	320
7013	321

3014	306
3015	307
3016	308
3017	309
3018	501
3019	502
3020	503
3021	504
3022	505
3023	506
3024	507
3025	508
3026	509
3027	701
3028	702
3029	703
3030	704
3031	705
3032	706
3033	707
3034	708
3035	709
3036	901
3037	902
3038	903
3039	904
3040	905
3041	906
3042	907
3043	908
3044	909
3045	1101
3046	1102
3047	1103
3048	1104
3049	1105
3050	1106
3051	1107
3052	1108
3053	1109
3054	1301
3055	1302
3056	1303
3057	1304
3058	1305
3059	1306
3060	1307
3061	1308
3062	1309
3063	1501
3064	1502
3065	1503
3066	1504
3067	1505
3068	1506
3069	1507
3070	1508
3071	1509
3072	1701

4014	310
4015	311
4016	312
4017	313
4018	505
4019	506
4020	507
4021	508
4022	509
4023	510
4024	511
4025	512
4026	513
4027	705
4028	706
4029	707
4030	708
4031	709
4032	710
4033	711
4034	712
4035	713
4036	905
4037	906
4038	907
4039	908
4040	909
4041	910
4042	911
4043	912
4044	913
4045	1105
4046	1106
4047	1107
4048	1108
4049	1109
4050	1110
4051	1111
4052	1112
4053	1113
4054	1305
4055	1306
4056	1307
4057	1308
4058	1309
4059	1310
4060	1311
4061	1312
4062	1313
4063	1505
4064	1506
4065	1507
4066	1508
4067	1509
4068	1510
4069	1511
4070	1512
4071	1513
4072	1705

5014	314
5015	315
5016	316
5017	317
5018	509
5019	510
5020	511
5021	512
5022	513
5023	514
5024	515
5025	516
5026	517
5027	709
5028	710
5029	711
5030	712
5031	713
5032	714
5033	715
5034	716
5035	717
5036	909
5037	910
5038	911
5039	912
5040	913
5041	914
5042	915
5043	916
5044	917
5045	1109
5046	1110
5047	1111
5048	1112
5049	1113
5050	1114
5051	1115
5052	1116
5053	1117
5054	1309
5055	1310
5056	1311
5057	1312
5058	1313
5059	1314
5060	1315
5061	1316
5062	1317
5063	1509
5064	1510
5065	1511
5066	1512
5067	1513
5068	1514
5069	1515
5070	1516
5071	1517
5072	1709

6013	318
6014	319
6015	320
6016	321
6125	513
6018	514
6019	515
6020	516
6021	517
6022	518
6023	519
6024	520
6025	521
6124	713
6027	714
6028	715
6029	716
6030	717
6031	718
6032	719
6033	720
6034	721
6123	913
6036	914
6037	915
6038	916
6039	917
6040	918
6041	919
6042	920
6043	921
6122	1113
6045	1114
6046	1115
6047	1116
6048	1117
6049	1118
6050	1119
6051	1120
6052	1121
6121	1313
6054	1314
6055	1315
6056	1316
6057	1317
6058	1318
6059	1319
6060	1320
6061	1321
6120	1513
6063	1514
6064	1515
6065	1516
6066	1517
6067	1518
6068	1519
6069	1520
6070	1521
6119	1713

7014	322
7015	323
7016	324
7017	325
7018	517
7019	518
7020	519
7021	520
7022	521
7023	522
7024	523
7025	524
7026	525
7027	717
7028	718
7029	719
7030	720
7031	721
7032	722
7033	723
7034	724
7035	725
7036	917
7037	918
7038	919
7039	920
7040	921
7041	922
7042	923
7043	924
7044	925
7045	1117
7046	1118
7047	1119
7048	1120
7049	1121
7050	1122
7051	1123
7052	1124
7053	1125
7054	1317
7055	1318
7056	1319
7057	1320
7058	1321
7059	1322
7060	1323
7061	1324
7062	1325
7063	1517
7064	1518
7065	1519
7066	1520
7067	1521
7068	1522
7069	1523
7070	1524
7071	1525
7072	1717

3073	1702	4073	1706	5073	1710	6072	1714	7073	1718
3074	1703	4074	1707	5074	1711	6073	1715	7074	1719
3075	1704	4075	1708	5075	1712	6074	1716	7075	1720
3076	1705	4076	1709	5076	1713	6075	1717	7076	1721
3077	1706	4077	1710	5077	1714	6076	1718	7077	1722
3078	1707	4078	1711	5078	1715	6077	1719	7078	1723
3079	1708	4079	1712	5079	1716	6078	1720	7079	1724
3080	1709	4080	1713	5080	1717	6079	1721	7080	1725
3081	1901	4081	1905	5081	1909	6118	1913	7081	1917
3082	1902	4082	1906	5082	1910	6081	1914	7082	1918
3083	1903	4083	1907	5083	1911	6082	1915	7083	1919
3084	1904	4084	1908	5084	1912	6083	1916	7084	1920
3085	1905	4085	1909	5085	1913	6084	1917	7085	1921
3086	1906	4086	1910	5086	1914	6085	1918	7086	1922
3087	1907	4087	1911	5087	1915	6086	1919	7087	1923
3088	1908	4088	1912	5088	1916	6087	1920	7088	1924
3089	1909	4089	1913	5089	1917	6088	1921	7089	1925
3090	2101	4090	2105	5090	2109	6117	2113	7090	2117
3091	2102	4091	2106	5091	2110	6090	2114	7091	2118
3092	2103	4092	2107	5092	2111	6091	2115	7092	2119
3093	2104	4093	2108	5093	2112	6092	2116	7093	2120
3094	2105	4094	2109	5094	2113	6093	2117	7094	2121
3095	2106	4095	2110	5095	2114	6094	2118	7095	2122
3096	2107	4096	2111	5096	2115	6095	2119	7096	2123
3097	2108	4097	2112	5097	2116	6096	2120	7097	2124
3098	2109	4098	2113	5098	2117	6097	2121	7098	2125
3099	2301	4099	2305	5099	2309	6099	2313	7099	2317
3100	2302	4100	2306	5100	2310	6100	2314	7100	2318
3101	2303	4101	2307	5101	2311	6101	2315	7101	2319
3102	2304	4102	2308	5102	2312	6102	2316	7102	2320
3103	2305	4103	2309	5103	2313	6103	2317	7103	2321
3104	2306	4104	2310	5104	2314	6104	2318	7104	2322
3105	2307	4105	2311	5105	2315	6105	2319	7105	2323
3106	2308	4106	2312	5106	2316	6106	2320	7106	2324
3107	2309	4107	2313	5107	2317	6107	2321	7107	2325
3108	2501	4108	2505	5108	2509	6108	2513	7108	2517
3109	2502	4109	2506	5109	2510	6109	2514	7109	2518
3110	2503	4110	2507	5110	2511	6110	2515	7110	2519
3111	2504	4111	2508	5111	2512	6111	2516	7111	2520
3112	2505	4112	2509	5112	2513	6112	2517	7112	2521
3113	2506	4113	2510	5113	2514	6113	2518	7113	2522
3114	2507	4114	2511	5114	2515	6114	2519	7114	2523
3115	2508	4115	2512	5115	2516	6115	2520	7115	2524
3116	2509	4116	2513	5116	2517	6116	2521	7116	2525

Table A.4 File number correspondence to source point for rectangular grid.

The receiver stations were assigned to geophone numbers in each of the five swaths (recording units) since the geophone position changed for every different swath. The correspondence of receiver stations to geophone numbers was done following Table A.5:

Swath 1		Swath 2		Swath 3		Swath 4		Swath 5	
Geophone number	Receiver station	Geophone number	Receiver station	Geophone number	Receiver station	Geophone number	Receiver station	Geophone number	Receiver station
1	2204	1	2208	1	2212	1	2216	1	2220
2	2004	2	2008	2	2012	2	2016	2	2020
3	1804	3	1808	3	1812	3	1816	3	1820
4	1604	4	1608	4	1612	4	1616	4	1620
5	1404	5	1408	5	1412	5	1416	5	1420
6	1204	6	1208	6	1212	6	1216	6	1220
7	1004	7	1008	7	1012	7	1016	7	1020
8	804	8	808	8	812	8	816	8	820
9	604	9	608	9	612	9	616	9	620
10	404	10	408	10	412	10	416	10	420
11	406	11	410	11	414	11	418	11	422
12	606	12	610	12	614	12	618	12	622
13	806	13	810	13	814	13	818	13	822
14	1006	14	1010	14	1014	14	1018	14	1022
15	1206	15	1210	15	1214	15	1218	15	1222
16	1406	16	1410	16	1414	16	1418	16	1422
17	1606	17	1610	17	1614	17	1618	17	1622
18	1806	18	1810	18	1814	18	1818	18	1822
19	2006	19	2010	19	2014	19	2018	19	2022
20	2206	20	2210	20	2214	20	2218	20	2222

Table A.5 Correspondence between geophone numbers and receiver stations for the five different swaths in the 3C – 3D seismic survey.

The survey file contains the geographical coordinates for all the stations of the study area (Table A.6). This file is used to add the spatial relations to the seismic traces in the 3C – 3D survey. No elevation information is considered since no variation was observed.

Station number	North (cm)	East (cm)
101	175	175
102	200	175
103	225	175
104	250	175
105	275	175
106	300	175
107	325	175
108	350	175
109	375	175
110	400	175
111	425	175
112	450	175
113	475	175
114	500	175
115	525	175
116	550	175
117	575	175
118	600	175
119	625	175
120	650	175
121	675	175
122	700	175

Station number	North (cm)	East (cm)
1401	175	500
1402	200	500
1403	225	500
1404	250	500
1405	275	500
1406	300	500
1407	325	500
1408	350	500
1409	375	500
1410	400	500
1411	425	500
1412	450	500
1413	475	500
1414	500	500
1415	525	500
1416	550	500
1417	575	500
1418	600	500
1419	625	500
1420	650	500
1421	675	500
1422	700	500

123	725	175
124	750	175
125	775	175
201	175	200
202	200	200
203	225	200
204	250	200
205	275	200
206	300	200
207	325	200
208	350	200
209	375	200
210	400	200
211	425	200
212	450	200
213	475	200
214	500	200
215	525	200
216	550	200
217	575	200
218	600	200
219	625	200
220	650	200
221	675	200
222	700	200
223	725	200
224	750	200
225	775	200
301	175	225
302	200	225
303	225	225
304	250	225
305	275	225
306	300	225
307	325	225
308	350	225
309	375	225
310	400	225
311	425	225
312	450	225
313	475	225
314	500	225
315	525	225
316	550	225
317	575	225
318	600	225
319	625	225
320	650	225
321	675	225
322	700	225
323	725	225
324	750	225
325	775	225
401	175	250
402	200	250
403	225	250
404	250	250
405	275	250
406	300	250
407	325	250
408	350	250
409	375	250
410	400	250
411	425	250
412	450	250
413	475	250
414	500	250
415	525	250
416	550	250
417	575	250
418	600	250
419	625	250
420	650	250
421	675	250

1423	725	500
1424	750	500
1425	775	500
1501	175	525
1502	200	525
1503	225	525
1504	250	525
1505	275	525
1506	300	525
1507	325	525
1508	350	525
1509	375	525
1510	400	525
1511	425	525
1512	450	525
1513	475	525
1514	500	525
1515	525	525
1516	550	525
1517	575	525
1518	600	525
1519	625	525
1520	650	525
1521	675	525
1522	700	525
1523	725	525
1524	750	525
1525	775	525
1601	175	550
1602	200	550
1603	225	550
1604	250	550
1605	275	550
1606	300	550
1607	325	550
1608	350	550
1609	375	550
1610	400	550
1611	425	550
1612	450	550
1613	475	550
1614	500	550
1615	525	550
1616	550	550
1617	575	550
1618	600	550
1619	625	550
1620	650	550
1621	675	550
1622	700	550
1623	725	550
1624	750	550
1625	775	550
1701	175	575
1702	200	575
1703	225	575
1704	250	575
1705	275	575
1706	300	575
1707	325	575
1708	350	575
1709	375	575
1710	400	575
1711	425	575
1712	450	575
1713	475	575
1714	500	575
1715	525	575
1716	550	575
1717	575	575
1718	600	575
1719	625	575
1720	650	575
1721	675	575

422	700	250
423	725	250
424	750	250
425	775	250
501	175	275
502	200	275
503	225	275
504	250	275
505	275	275
506	300	275
507	325	275
508	350	275
509	375	275
510	400	275
511	425	275
512	450	275
513	475	275
514	500	275
515	525	275
516	550	275
517	575	275
518	600	275
519	625	275
520	650	275
521	675	275
522	700	275
523	725	275
524	750	275
525	775	275
601	175	300
602	200	300
603	225	300
604	250	300
605	275	300
606	300	300
607	325	300
608	350	300
609	375	300
610	400	300
611	425	300
612	450	300
613	475	300
614	500	300
615	525	300
616	550	300
617	575	300
618	600	300
619	625	300
620	650	300
621	675	300
622	700	300
623	725	300
624	750	300
625	775	300
701	175	325
702	200	325
703	225	325
704	250	325
705	275	325
706	300	325
707	325	325
708	350	325
709	375	325
710	400	325
711	425	325
712	450	325
713	475	325
714	500	325
715	525	325
716	550	325
717	575	325
718	600	325
719	625	325
720	650	325

1722	700	575
1723	725	575
1724	750	575
1725	775	575
1801	175	600
1802	200	600
1803	225	600
1804	250	600
1805	275	600
1806	300	600
1807	325	600
1808	350	600
1809	375	600
1810	400	600
1811	425	600
1812	450	600
1813	475	600
1814	500	600
1815	525	600
1816	550	600
1817	575	600
1818	600	600
1819	625	600
1820	650	600
1821	675	600
1822	700	600
1823	725	600
1824	750	600
1825	775	600
1901	175	625
1902	200	625
1903	225	625
1904	250	625
1905	275	625
1906	300	625
1907	325	625
1908	350	625
1909	375	625
1910	400	625
1911	425	625
1912	450	625
1913	475	625
1914	500	625
1915	525	625
1916	550	625
1917	575	625
1918	600	625
1919	625	625
1920	650	625
1921	675	625
1922	700	625
1923	725	625
1924	750	625
1925	775	625
2001	175	650
2002	200	650
2003	225	650
2004	250	650
2005	275	650
2006	300	650
2007	325	650
2008	350	650
2009	375	650
2010	400	650
2011	425	650
2012	450	650
2013	475	650
2014	500	650
2015	525	650
2016	550	650
2017	575	650
2018	600	650
2019	625	650
2020	650	650

721	675	325
722	700	325
723	725	325
724	750	325
725	775	325
801	175	350
802	200	350
803	225	350
804	250	350
805	275	350
806	300	350
807	325	350
808	350	350
809	375	350
810	400	350
811	425	350
812	450	350
813	475	350
814	500	350
815	525	350
816	550	350
817	575	350
818	600	350
819	625	350
820	650	350
821	675	350
822	700	350
823	725	350
824	750	350
825	775	350
901	175	375
902	200	375
903	225	375
904	250	375
905	275	375
906	300	375
907	325	375
908	350	375
909	375	375
910	400	375
911	425	375
912	450	375
913	475	375
914	500	375
915	525	375
916	550	375
917	575	375
918	600	375
919	625	375
920	650	375
921	675	375
922	700	375
923	725	375
924	750	375
925	775	375
1001	175	400
1002	200	400
1003	225	400
1004	250	400
1005	275	400
1006	300	400
1007	325	400
1008	350	400
1009	375	400
1010	400	400
1011	425	400
1012	450	400
1013	475	400
1014	500	400
1015	525	400
1016	550	400
1017	575	400
1018	600	400
1019	625	400

2021	675	650
2022	700	650
2023	725	650
2024	750	650
2025	775	650
2101	175	675
2102	200	675
2103	225	675
2104	250	675
2105	275	675
2106	300	675
2107	325	675
2108	350	675
2109	375	675
2110	400	675
2111	425	675
2112	450	675
2113	475	675
2114	500	675
2115	525	675
2116	550	675
2117	575	675
2118	600	675
2119	625	675
2120	650	675
2121	675	675
2122	700	675
2123	725	675
2124	750	675
2125	775	675
2201	175	700
2202	200	700
2203	225	700
2204	250	700
2205	275	700
2206	300	700
2207	325	700
2208	350	700
2209	375	700
2210	400	700
2211	425	700
2212	450	700
2213	475	700
2214	500	700
2215	525	700
2216	550	700
2217	575	700
2218	600	700
2219	625	700
2220	650	700
2221	675	700
2222	700	700
2223	725	700
2224	750	700
2225	775	700
2301	175	725
2302	200	725
2303	225	725
2304	250	725
2305	275	725
2306	300	725
2307	325	725
2308	350	725
2309	375	725
2310	400	725
2311	425	725
2312	450	725
2313	475	725
2314	500	725
2315	525	725
2316	550	725
2317	575	725
2318	600	725
2319	625	725

1020	650	400
1021	675	400
1022	700	400
1023	725	400
1024	750	400
1025	775	400
1101	175	425
1102	200	425
1103	225	425
1104	250	425
1105	275	425
1106	300	425
1107	325	425
1108	350	425
1109	375	425
1110	400	425
1111	425	425
1112	450	425
1113	475	425
1114	500	425
1115	525	425
1116	550	425
1117	575	425
1118	600	425
1119	625	425
1120	650	425
1121	675	425
1122	700	425
1123	725	425
1124	750	425
1125	775	425
1201	175	450
1202	200	450
1203	225	450
1204	250	450
1205	275	450
1206	300	450
1207	325	450
1208	350	450
1209	375	450
1210	400	450
1211	425	450
1212	450	450
1213	475	450
1214	500	450
1215	525	450
1216	550	450
1217	575	450
1218	600	450
1219	625	450
1220	650	450
1221	675	450
1222	700	450
1223	725	450
1224	750	450
1225	775	450
1301	175	475
1302	200	475
1303	225	475
1304	250	475
1305	275	475
1306	300	475
1307	325	475
1308	350	475
1309	375	475
1310	400	475
1311	425	475
1312	450	475
1313	475	475
1314	500	475
1315	525	475
1316	550	475
1317	575	475
1318	600	475

2320	650	725
2321	675	725
2322	700	725
2323	725	725
2324	750	725
2325	775	725
2401	175	750
2402	200	750
2403	225	750
2404	250	750
2405	275	750
2406	300	750
2407	325	750
2408	350	750
2409	375	750
2410	400	750
2411	425	750
2412	450	750
2413	475	750
2414	500	750
2415	525	750
2416	550	750
2417	575	750
2418	600	750
2419	625	750
2420	650	750
2421	675	750
2422	700	750
2423	725	750
2424	750	750
2425	775	750
2501	175	775
2502	200	775
2503	225	775
2504	250	775
2505	275	775
2506	300	775
2507	325	775
2508	350	775
2509	375	775
2510	400	775
2511	425	775
2512	450	775
2513	475	775
2514	500	775
2515	525	775
2516	550	775
2517	575	775
2518	600	775
2519	625	775
2520	650	775
2521	675	775
2522	700	775
2523	725	775
2524	750	775
2525	775	775

1319	625	475
1320	650	475
1321	675	475
1322	700	475
1323	725	475
1324	750	475
1325	775	475

Table A.6 Geographical coordinates for 3C – 3D seismic survey.